



**CALIFORNIA
ENERGY COMMISSION**



**CALIFORNIA
natural
resources
AGENCY**

Energy Research and Development Division

FINAL PROJECT REPORT

Performance-Based Earthquake Engineering Assessment Tool for Natural Gas Storage and Pipeline Systems

Task 4F – System Wide Natural Gas Infrastructure Response
and Fragility Model Report

Gavin Newsom, Governor
November 2022 | CEC-500-XXXX-XXX

PREPARED BY:

Primary Author:

Jennie Watson-Lamprey, Micaela Largent, Barry Zheng

Slate Geotechnical Consultants
2927 Newbury St. Berkeley, California
510-277-3325
<https://slategeotech.com/>

Contract Number: PIR-18-003

PREPARED FOR:

California Energy Commission

Yahui Yang

Project Manager

Laurie ten Hope

Deputy Director

ENERGY RESEARCH AND DEVELOPMENT DIVISION

Drew Bohan

Executive Director

DISCLAIMER

This report was prepared as the result of work sponsored by the California Energy Commission. It does not necessarily represent the views of the Energy Commission, its employees or the State of California. The Energy Commission, the State of California, its employees, contractors and subcontractors make no warranty, express or implied, and assume no legal liability for the information in this report; nor does any party represent that the uses of this information will not infringe upon privately owned rights. This report has not been approved or disapproved by the California Energy Commission nor has the California Energy Commission passed upon the accuracy or adequacy of the information in this report.

ACKNOWLEDGEMENTS

The Performance-Based Earthquake Engineering Assessment Tool for Natural Gas Storage and Pipeline Systems project is led by Professor Jonathan Bray at the University of California Berkeley, with partners at the University of California Berkeley, University of Nevada Reno (UNR), Lawrence Berkeley National Laboratories (LBNL), University of California (UC) San Diego, NHERI SimCenter at UC Berkeley, and Slate Geotechnical Consultants and its subcontractors Lettis Consultants International (LCI) and Thomas O'Rourke. The authors are grateful for the technical input and advice from all members of the project team, and especially Professor Thomas O'Rourke of Cornell University. The authors are also grateful for the support of the staff at the UC San Diego and UNR Laboratories; donations of materials by University Mechanical and Engineering Contractors (UMEC) of El Cajon, California and SoCalGas; and fabrication and delivery of the component specimens tested at UC San Diego by UMEC.

This research study was funded by the California Energy Commission, under Contract No. PIR 18-003. The opinions, findings, conclusions, and recommendations expressed in this publication are those of the authors and do not necessarily reflect the view of California Energy Commission and its employees, the State of California, the Pacific Earthquake Engineering Research (PEER) Center, and the Regents of the University of California.

PREFACE

The California Energy Commission's (CEC) Energy Research and Development Division manages the Natural Gas Research and Development Program, which supports energy-related research, development, and demonstration not adequately provided by competitive and regulated markets. These natural gas research investments spur innovation in energy efficiency, renewable energy and advanced clean generation, energy-related environmental protection, energy transmission and distribution and transportation.

The Energy Research and Development Division conducts this public interest natural gas-related energy research by partnering with RD&D entities, including individuals, businesses, utilities and public and private research institutions. This program promotes greater natural gas reliability, lower costs and increases safety for Californians and is focused in these areas:

- Buildings End-Use Energy Efficiency.
- Industrial, Agriculture and Water Efficiency
- Renewable Energy and Advanced Generation
- Natural Gas Infrastructure Safety and Integrity.
- Energy-Related Environmental Research
- Natural Gas-Related Transportation.

The *Task4F - System Wide Natural Gas Infrastructure Response and Fragility Model Report* is an interim report for the Performance-Based Earthquake Engineering Assessment Tool for Natural Gas Storage and Pipeline Systems project (PIR 18-003) conducted by Pacific Earthquake Engineering Research Center. The information from this project contributes to the Energy Research and Development Division's Natural Gas Research and Development Program.

For more information about the Energy Research and Development Division, please visit the [CEC's research website](http://www.energy.ca.gov/research/) (www.energy.ca.gov/research/) or contact the CEC at 916-327-1551.

ABSTRACT

This report is one of a series of reports documenting the methods and findings of a multi-year, multi-disciplinary project conducted by the Pacific Earthquake Engineering Research Center (PEER) with the Lawrence Berkeley National Laboratory (LBNL) and funded by the California Energy Commission (CEC). The overall project is titled *Performance-based Earthquake Engineering Assessment Tool for Natural Gas Storage and Pipeline Systems* henceforth referred to as the *OpenSRA* Project.

The overall goal of the *OpenSRA* Project is to create an open-source research-based seismic risk assessment tool for natural gas infrastructure that can be used by utility stakeholders to better understand state-wide risks, prioritize mitigation, plan new gas infrastructure, and help focus post-earthquake repair work.

The project team includes researchers from UC Berkeley, LBNL, UC San Diego, University of Nevada Reno, the NHERI SimCenter at UC Berkeley, and Slate Geotechnical Consultants and its subcontractors Lettis Consultants International (LCI) and Thomas O'Rourke of Cornell University. Focused research to advance the seismic risk assessment tool was conducted by Tasks, each addressing a particular area of study and expertise, and collaborating with the other Tasks.

This subsection of the project focuses on the fragility of natural gas infrastructure. Three systems are considered (buried pipeline, underground storage facilities, and surficial storage and distribution systems). Each has undergone finite element modeling to estimate the response of the system and the probability of failure. The results of the finite element modeling are used to develop fragility curves that are implemented into *OpenSRA* to aid end users in estimating failures in their systems as well as planning mitigation efforts.

Keywords: Fragility, natural gas, demand, resistance, risk

Please use the following citation for this report:

Watson-Lamprey, Jennie; Micaela Largent; Barry Zheng. 2022. *Performance-based Earthquake Engineering Assessment Tool for Natural Gas Storage and Pipeline Systems, Task 4F - System Wide Natural Gas Infrastructure Response and Fragility Model Report*. California Energy Commission. Publication Number: CEC-500-202X-XXX.

TABLE OF CONTENTS

	Page
ACKNOWLEDGEMENTS	i
PREFACE.....	ii
ABSTRACT.....	iii
TABLE OF CONTENTS	iv
LIST OF FIGURES	v
LIST OF TABLES.....	viii
EXECUTIVE SUMMARY	1
Introduction	1
Project Purpose	1
Project Approach	2
Project Results	2
CHAPTER 1: Introduction.....	3
CHAPTER 2: Project Approach.....	5
2.1 Introduction.....	5
2.2 <i>OpenSRA</i>	5
2.2.1 PEER Risk Framework.....	5
2.2.2 Efficient Evaluation of the PBEE Risk Framework	6
2.2.3 Simplification of the Triple Integral to One-Dimensional Integrals.....	7
2.2.4 <i>OpenSRA</i> Overview	8
2.3 Fragility Curve Development	12
2.3.1 System Modeling.....	12
2.3.2 Sensitivity Studies	12
2.3.3 Final Fragility Curves	13
CHAPTER 3: Project Results.....	15
3.1 Introduction.....	15
3.2 Below Ground Pipelines	15
3.2.1 Sensitivity Analysis	15
3.2.2 Tensile and Compressive Strain Damage Models	17
3.2.3 Tensile and Compressive Strain Failure Models.....	18
3.3 Wells and Caprocks	23
3.3.1 Fragility of Wells	24

3.3.2	Fragility of Caprocks	35
3.4	Above Ground Infrastructure.....	37
3.4.2	Damage Model for Wellheads to Ground Shaking	40
3.4.3	Fragility Model for Wellheads to Ground Shaking	41
3.4.4	Damage Models for Storage Containers and Pressure Vessels to Ground Shaking.....	41
3.4.5	Fragility Models for Storage Containers and Pressure Vessels to Ground Shaking.....	43
CHAPTER 4:	Conclusions/Recommendations	44
4.1	Implementation in <i>OpenSRA</i>	44
4.2	Recommendations for Further Research.....	44
GLOSSARY AND LIST OF ACRONYMS.....		45
REFERENCES.....		49
APPENDIX A:	Failure Mechanism Logic for Buried Pipelines	A-1
APPENDIX B:	Damage Models of Below Ground Pipelines.....	B-1
APPENDIX C:	Damage Models of Wells	C-1
APPENDIX D:	Damage Models of Above Ground Infrastructure	D-1

LIST OF FIGURES

	Page
Figure 1: PEER Risk Methodology Applied to Below Ground Pipelines	9
Figure 2: PEER Risk Methodology Applied to Wells and Caprocks.....	10
Figure 3: PEER Risk Methodology Applied to Above Ground Components	11
Figure 4: <i>OpenSRA</i> User Experience Flow Chart.....	11
Figure 5: Well tree dimension distributions for Latin Hypercube Sampling	13
Figure 6: Mean Joint Rotation in Wellheads due to Ground Shaking	13
Figure 7: Probability of Failure for Wellheads due to Ground Shaking.....	14
Figure 8: Probability of Failure for Wellheads due to Ground Shaking.....	14
Figure 9: Tornado Diagrams from Sensitivity Study.....	17
Figure 10: Assessed Ground Deformation Modes	18
Figure 11: Tensile Damage State Fragility Model	20
Figure 12: Critical Compressive Pipe Strain Data.....	21
Figure 13: Probability of Compressive Rupture for Select D/t Ratios.....	23

Figure 14: Fragility Curve Development for UGS Integrity	24
Figure 15: Typical Gas Storage Well Cross Section (Above Reservoir)	25
Figure 16: Depiction of fault shear through a well, at Aliso Canyon.....	26
Figure 17: The Numerical Model for the Well Shear Simulation	26
Figure 18: Outputs of the Well Shear Analysis	28
Figure 19: Probability of Failure for Well Casing and Tubing due to Fault Offset	30
Figure 20: Finite-Element Conceptual Model Used in OpenSees	30
Figure 21: Probability of Failure for Conductor Casing due to Ground Shaking	33
Figure 22: Probability of Failure for Surface Casing due to Ground Shaking	34
Figure 23: Probability of Failure for Production Casing due to Ground Shaking	34
Figure 24: Probability of Failure for Tubing due to Ground Shaking.....	35
Figure 25: Conceptual Model of Flow Area of an Activated Fault Crossing a Caprock.....	36
Figure 26: Component models for the tee rotating in-plane.....	37
Figure 27: Summary of configuration of laterals	40
Figure 28: Probability of Failure for Wellheads due to Ground Shaking.....	41
Figure 29: Vertical pressure vessels modeled in OpenSees and Abaqus.....	42
Figure 30: Probability of Failure for Pressure Vessels due to Ground Shaking	43
Figure 31: Left Lateral Strike-Slip Fault Displacement Geometry	A-3
Figure 32: Oblique Normal with Left Lateral Strike-Slip Geometry	A-5
Figure 33: Normal-Slip Geometry.....	A-6
Figure 34: Oblique Normal with Right Lateral Strike-Slip Geometry	A-7
Figure 35: Right Lateral Strike-Slip Geometry	A-8
Figure 36: Oblique Reverse with Left Lateral Strike-Slip Geometry	A-9
Figure 37: Reverse-Slip Geometry.....	A-10
Figure 38: Oblique Reverse with Right Lateral Strike-Slip Geometry	A-11
Figure 39: Landslide Crossing – Level 2 and 3 – Location Logic	A-15
Figure 40: Landslide Crossing – Level 2 and 3 – Angle Logic	A-15
Figure 41: Lateral Spreading – Level 2 – Angle of Crossing Logic.....	A-17
Figure 42: Lateral Spreading – Level 3 – Angle of Crossing Logic.....	A-18
Figure 43: Liquefaction-Induced Settlement – Level 3 – Analysis Logic	B-20
Figure 44: Modeled Pipeline Response to Tensile and Compressive Pipe Strain	B-2

Figure 45: SRSS values of the model parameters for the casing in the first well mode (cemented annulus case): (a) first to 14th parameters; (b) 15th to 27th parameters.....	C-2
Figure 46: SRSS values of the model parameters for the tubing in the first well mode (cemented annulus case): (a) first to 14th parameters; (b) 15th to 27th parameters.....	C-3
Figure 47: SRSS values of the model parameters for the casing in the second well mode (cemented annulus case): (a) first to 14th parameters; (b) 15th to 27th parameters.....	C-4
Figure 48: SRSS values of the model parameters for the tubing in the second well mode (cemented annulus case): (a) first to 14th parameters; (b) 15th to 27th parameters.....	C-6
Figure 49: SRSS values of the model parameters for the casing in the fourth well mode (cemented annulus case): (a) first to 14th parameters; (b) 15th to 27th parameters.....	C-7
Figure 50: SRSS values of the model parameters for the tubing in the fourth well mode (cemented annulus case): (a) first to 14th parameters; (b) 15th to 27th parameters.....	C-8
Figure 51: SRSS values of the model parameters for the casing in the first well mode (uncemented annulus case): (a) first to 11th parameters; (b) 12th to 22nd parameters.....	C-10
Figure 52: SRSS values of the model parameters for the tubing in the first well mode (uncemented annulus case): (a) first to 11th parameters; (b) 12th to 22nd parameters.....	C-11
Figure 53: SRSS values of the model parameters for the casing in the second well mode (uncemented annulus case): (a) first to 11th parameters; (b) 12th to 22nd parameters.....	C-12
Figure 54: SRSS values of the model parameters for the tubing in the second well mode (uncemented annulus case): (a) first to 11th parameters; (b) 12th to 22nd parameters.....	C-13
Figure 55: SRSS values of the model parameters for the casing in the fourth well mode (uncemented annulus case): (a) first to 11th parameters; (b) 12th to 22nd parameters.....	C-14
Figure 56: SRSS values of the model parameters for the tubing in the fourth well mode (uncemented annulus case): (a) first to 11th parameters; (b) 12th to 22nd parameters.....	C-15
Figure 57: Sensitivity Analysis Result for Conductor Casing (RSN548_CHALFANT.A_A-BEN)	C-21
Figure 58: Sensitivity Analysis Result for Surface Casing (RSN548_CHALFANT.A_A-BEN)....	C-22
Figure 59: Sensitivity Analysis Result for Production Casing (RSN548_CHALFANT.A_A-BEN) ...	C-22
Figure 60: Sensitivity Analysis Result for Tubing (RSN548_CHALFANT.A_A-BEN)	C-23
Figure 61: Sensitivity Analysis Result for Conductor Casing (RSN77_SFERN_PUL)	C-23
Figure 62: Sensitivity Analysis Result for Surface Casing (RSN77_SFERN_PUL)	C-24
Figure 63: Sensitivity Analysis Result for Production Casing (RSN77_SFERN_PUL)	C-24
Figure 64: Sensitivity Analysis Result for Tubing (RSN77_SFERN_PUL).....	C-25
Figure 65: Sensitivity Analysis Result for Conductor Casing (RSN548_CHALFANT.A_A-BEN)	C-26
Figure 66: Sensitivity Analysis Result for Surface Casing (RSN548_CHALFANT.A_A-BEN)....	C-26

Figure 67: Sensitivity Analysis Result for Production Casing (RSN548_CHALFANT.A_A-BEN)...	C-27
Figure 68: Sensitivity Analysis Result for Tubing (RSN548_CHALFANT.A_A-BEN)	C-27
Figure 69: Sensitivity Analysis Result for Conductor Casing (RSN77_SFERN_PUL).....	C-28
Figure 70: Sensitivity Analysis Result for Surface Casing (RSN77_SFERN_PUL)	C-28
Figure 71: Sensitivity Analysis Result for Production Casing (RSN77_SFERN_PUL)	C-29
Figure 72: Sensitivity Analysis Result for Tubing (RSN77_SFERN_PUL).....	C-29
Figure 73: Sensitivity Analysis Result for Conductor Casing (RSN548_CHALFANT.A_A-BEN)	C-30
Figure 74: Sensitivity Analysis Result for Surface Casing (RSN548_CHALFANT.A_A-BEN)....	C-31
Figure 75: Sensitivity Analysis Result for Production Casing (RSN548_CHALFANT.A_A-BEN)...	C-31
Figure 76: Sensitivity Analysis Result for Tubing (RSN548_CHALFANT.A_A-BEN)	C-32
Figure 77: Sensitivity Analysis Result for Conductor Casing (RSN77_SFERN_PUL).....	C-32
Figure 78: Sensitivity Analysis Result for Surface Casing (RSN77_SFERN_PUL)	C-33
Figure 79: Sensitivity Analysis Result for Production Casing (RSN77_SFERN_PUL)	C-33
Figure 80: Sensitivity Analysis Result for Tubing (RSN77_SFERN_PUL).....	C-34
Figure 81: Schematic of subsystem P2-E (elbow) with well tree dimensions	D-2
Figure 82: Schematic of subsystem P2-T (tee-joints) with well tree dimensions	D-3
Figure 83: Schematic of subsystem P3-E (elbow) with well tree dimensions	D-4
Figure 84: Schematic of subsystem P3-T (tee-joints) with well tree dimensions	D-5
Figure 85: Schematic of subsystem P4-E (elbows) with well tree dimensions.....	D-7
Figure 86: Schematic of subsystem P4-T (tee-joints) with well tree dimensions	D-8

LIST OF TABLES

	Page
Table 1: List of Parameters Used in Sensitivity Analysis.....	16
Table 2: Top Four Well Configuration Modes	24
Table 3: Sensitivity Inputs for Fragility of Wells to Fault Displacement	27
Table 4: Cases used for Latin Hypercube Sampling	29
Table 5: Metrics for failure model for fault offset induced well failure.....	29
Table 6: Nominal and Increment Values for Parameters Related to Soil.....	31

Table 7: List of damage models created for shaking of a well	32
Table 8: Metrics for failure model for shaking induced well failure	33
Table 9: Parameters for caprock fragilities and their range.....	36
Table 10: Configurations of WTP subsystem, variables considered and EDP	38
Table 11: Range of Rake Angles for Analysis Method	A-2
Table 12: Range of Parameters Used in Numerical Simulations.....	B-1
Table 13: Model Regression Coefficients to Estimate Δ_o	B-3
Table 14: Recommended Default ϵ_{ult} (%) Values Based on Steel Grade.....	B-3
Table 15: Model Regression Coefficients to Estimate ϵ_{long}	B-4
Table 16: Regression Coefficient to estimate Δu	B-6
Table 17: Regression Coefficient to estimate ϵ_{long}	B-7
Table 18: Model Regression Coefficients to Estimate $\sigma_{In\epsilon}$	B-9
Table 19: Coefficients for first and second well mode, with cement for well casing	C-16
Table 20: Coefficients for first well mode, with cement for well tubing	C-16
Table 21: Coefficients for second well mode, with cement for well tubing	C-17
Table 22: Coefficients for fourth well mode, with cement for well tubing.....	C-18
Table 23: Coefficients for fourth well mode, with cement for well casing.....	C-18
Table 24: Coefficients for well modes, with no cement for the well casing.....	C-19
Table 25: Coefficients for first, second, and fourth without cement - tubing	C-19
Table 26: Coefficients for fourth well mode without cement - casing.....	C-20
Table 27: Model Coefficients for Conductor Casings	C-35
Table 28: Model Coefficients for Surface Casings.....	C-35
Table 29: Model Coefficients for Production Casings	C-36
Table 30: Model Coefficients for Tubings.....	C-36
Table 31: Coefficients for subsystem P2-E (elbows)	D-2
Table 32: Coefficients for subsystem P2-T (tee-joints)	D-3
Table 33: Coefficients for subsystem P3-E (elbows)	D-4
Table 34: Coefficients for subsystem P3-T (tee-joints)	D-5
Table 35: Coefficients for subsystem P4-E (elbows)	D-6
Table 36: Coefficients for subsystem P4-T (tee-joints)	D-8
Table 37: Coefficients for strain models	D-9
Table 38: Coefficients for the moment ratio model with and without stretch length	D-10

EXECUTIVE SUMMARY

Introduction

This report is one of a series of reports documenting the methods and findings of a multi-year, multi-disciplinary project conducted by the Pacific Earthquake Engineering Research Center (PEER) with the Lawrence Berkeley National Laboratory (LBNL) and funded by the California Energy Commission (CEC). The overall project is titled *Performance-based Earthquake Engineering Assessment Tool for Natural Gas Storage and Pipeline Systems*, henceforth referred to as the *OpenSRA* Project.

The overall goal of the *OpenSRA* Project is to create an open-source research-based seismic risk assessment tool for natural gas infrastructure that can be used by utility stakeholders to better understand state-wide risks, prioritize mitigation, plan new gas infrastructure, and help focus post-earthquake repair work.

The project team includes researchers from University of California (UC) Berkeley, LBNL, UC San Diego, University of Nevada Reno, the Natural Hazards Engineering Research Infrastructure (NHERI) SimCenter at UC Berkeley, and Slate Geotechnical Consultants (Slate) and its subcontractors Lettis Consultants International (LCI) and Professor Thomas O'Rourke of Cornell University. Focused research to advance the seismic risk assessment tool was conducted by Tasks, each addressing a particular area of study and expertise, and collaborating with the other Tasks.

This report is the sixth report submitted in a series of reports to satisfy the requirements of the *OpenSRA* Project. The first four reports focused on calculating system demands including fault displacement (Thompson et al., 2021), liquefaction and ground-motion deformation (Bain et al., 2022), the seismic response of wells and caprocks associated with underground gas storage (Rutqvist et al., 2022), and the seismic response of surface pipeline and gas storage infrastructure (Pantoli et al., 2022). The fifth report focused on educating natural gas infrastructure owners on modern monitoring technologies for evaluating the parameters that *OpenSRA* will use to make assessments of natural gas infrastructure risk in California (Wang et al., 2022). This report integrates the demand calculations that were evaluated in the first four reports with information about the ability of the infrastructure to withstand those demands explored through Finite Element Analysis in Bain et al. (2022), Pantoli et al. (2022), and Rutqvist et al. (2022). The result is a set of damage models and fragility models implemented in *OpenSRA* that enables the end users to estimate the annual number of leaks and/or breaks caused by seismicity in California.

Project Purpose

The goal of the task described in this report is to develop fragility models that incorporate both the system demands evaluated in Tasks A and B and the infrastructure capacity explored in Tasks B through D.

$$\lambda_{dv} = \int_{DM} \int_{EDP} \int_{IM} P\{DV > dv|dm\} p\{dm|edp\} p\{edp|im\} \lambda_{im} d(im) d(edp) d(dm) \quad (1)$$

OpenSRA uses the PEER risk methodology presented by Moehle and Deierlein (2004) that combines multiple conditional probabilities to calculate the annual rate of exceedance of a specified loss metric (see Equation (1), above). Equation (1) is described in detail later in this report. Our focus here is on how the main components relate to the various research tasks. Previously submitted reports (Thompson et al. 2021, Bain et al. 2022, Rutqvist et al. 2022, and Pantoli et al. 2022) focused on developing the last probability in Equation 1 (developing intensity measures and engineering demand parameters). This report utilizes this information to estimate the first and second probability, going from engineering demand parameter to damage measure and damage measure to decision variable. The overall goal of this task is to synthesize the work performed by other researchers into fragility curves (both damage and fragility models) for buried pipeline, wells, caprocks, and above-ground infrastructure.

Project Approach

Tasks B, C, and D each performed finite element analyses to parameterize their system and to develop a model using programs such as Abaqus, OpenSees, and FLAC to test their infrastructure. In some cases, these programs were also used to validate lab testing. In addition to finite element analyses, Task D performed laboratory tests to generate data for validating their finite element models. Once the models were developed and validated, the teams performed in-depth sensitivity analyses, and the results are presented within this report in the form of tornado plots. From the sensitivity analyses, the teams determined the list of parameters that controlled the response of their model. The teams then performed additional finite element analyses focusing on the significant parameters to develop a robust dataset from which damage models were developed. This is further described in Chapter 2.

Project Results

Damage models for natural gas infrastructure were developed using data from Tasks B through D and are presented in this report. These new models capture:

1. Longitudinal (compressive and tensile) strains along underground pipeline segments due to permanent ground deformation from liquefaction, landslide, and fault rupture;
2. Shear strains on wells due to fault offset (i.e., displacement);
3. Bending moments on wells due to strong ground shaking;
4. Onset of gas leakage from caprocks from fault shear;
5. Rotations and tensile strains concentrated at joints on wellheads due to ground shaking; and
6. Bending moments on pressure vessels due to ground shaking.

Each damage model listed above is accompanied by a fragility model that predicts the distributions of the probability of failure (i.e., rupture or leakage) given the uncertainty in the system damages and regression parameters. Each model has been incorporated into *OpenSRA*.

CHAPTER 1:

Introduction

This report is one of a series of reports documenting the methods and findings of a multi-year, multi-disciplinary project conducted by the Pacific Earthquake Engineering Research Center (PEER) with the Lawrence Berkeley National Laboratory (LBNL) and funded by the California Energy Commission (CEC). The overall project is titled *Performance-based Earthquake Engineering Assessment Tool for Natural Gas Storage and Pipeline Systems*, henceforth referred to as the *OpenSRA* Project.

The overall goal of the *OpenSRA* Project is to create an open-source research-based seismic risk assessment tool for natural gas infrastructure that can be used by utility stakeholders to better understand state-wide risks, prioritize mitigation, plan new gas infrastructure, and help focus post-earthquake repair work.

The probabilistic seismic risk tool developed in this project follows the widely accepted risk methodology of Cornell (1968). A seismic source characterization is used to develop a suite of earthquake scenarios with associated rates of occurrence to represent the seismic hazard. Fault ruptures and the resulting ground shaking are generated for each earthquake scenario to represent the seismic loading, which includes a map of ground motion parameters. This scenario-based seismic parameter map is overlaid on the infrastructure system, and the seismic loading is related to the capacities of the infrastructure to calculate the seismic performance of the natural gas system for the scenario. By repeating the process for all the scenarios in the suite, the tool can evaluate the seismic risk to the system.

A user-driven research approach was used to develop *OpenSRA* to be applied easily by regulators and utilities, and to include updated models and methods for the seismic demands and capacities that control the seismic risk for natural gas systems. The project includes several innovative approaches that improve the basic methodology and distinguish this project's approach from standard approaches currently used. Current risk studies developed by the utilities use risk scoring approaches that are highly subjective and qualitative. They do not incorporate properly the uncertainties in the seismic demand and in the fragility of the system and its components. Targeted research was conducted in this project to improve the characterization of uncertainty of key inputs to the seismic risk assessment tool. The seismic risk methodology employed in this project provides quantitative estimates of the probabilistic seismic risk. For risk-informed decision-making processes, the reliability of the risk estimates needs to be considered because this can be significant, particularly for large, rare earthquakes.

The project team includes researchers from UC Berkeley, LBNL, UC San Diego, University of Nevada Reno, the PEER Center, the NHERI SimCenter, and Slate Geotechnical Consultants and its subcontractors Lettis Consultants International (LCI) and Thomas O'Rourke of Cornell University. Focused research to advance the seismic risk assessment tool was conducted by Tasks, each addressing a particular area of study and expertise, and collaborating with the other Tasks. The Tasks are as follows:

Task A: Fault displacement

Task B: Liquefaction-induced deformation and seismically induced slope displacement

Task C: Performance of natural gas storage well casings and caprock

Task D: Performance of gas storage and pipeline system surface infrastructure

Task E: Smart gas infrastructure sensing of wells and pipeline connections performance

Task F: Synthesis of component fragilities into a system performance model

This report addresses Task F: Synthesis of component fragilities into a system performance model. The following outlines the development of damage models and fragility models, collectively referred to as fragility curves, for each component of natural gas infrastructure (underground pipelines, above ground pipelines, storage facilities, wells, and caprocks).

CHAPTER 2:

Project Approach

2.1 Introduction

The following outlines the approach to synthesize the research on natural gas infrastructure presented in reports earlier this year (Thompson et al. 2021, Bain et al. 2022, Rutqvist et al. 2022, and Pantoli et al. 2022) into damage models and fragility models. Each type of infrastructure and demand is analyzed in a similar manner. First a damage model is developed to predict the response of the infrastructure in question by performing a sensitivity analysis on input parameters to determine the key parameters in the model, performing additional analyses to provide a robust dataset on which to base a model, and finally a regression analysis to develop damage models that address each of the probabilities within the PEER risk framework. Next, a fragility model is developed based on the damage models to predict the probability of failure. Collectively each task creates a series of damage models and fragility curves, herein referred to as fragility curves.

2.2 *OpenSRA*

OpenSRA follows the Performance-Based Earthquake Engineering (PBEE) risk methodology developed by PEER (Moehle and Deierlein, 2004) to assess the seismic risk of natural gas infrastructure. Details of the risk framework and modifications to the framework for more efficient computation are presented in the following sections. Overall, each stage in the PEER risk framework typically involves the evaluation of one analytical or regression model. The resulting metrics and their distributions from this evaluation are then propagated into the next stage until the probability of failure is assessed. Prior to this project, models existed in literature that fall into the earlier stages of the PEER risk framework (e.g., models that predicts system response given seismic intensity), but the knowledge for the latter stages of the framework was lacking (e.g., damage models for damage given system response and fragility models for probability of failure given damage). One of the primary goals of this research study is to perform analyses to develop new models that can be used to fill in this knowledge gap. The new models are then incorporated into *OpenSRA* and combined with the existing models described in the previously submitted CEC reports (Thompson et al. 2021, Bain et al. 2022) to perform a more complete seismic risk assessment.

2.2.1 PEER Risk Framework

In the PEER risk framework the annual rate of exceedance of a decision variable is calculated by:

$$\lambda_{dv} = \int_{DM} \int_{EDP} \int_{IM} P\{DV > dv|dm\} p\{dm|edp\} p\{edp|im\} \lambda_{im} d(im) d(edp) d(dm) \quad (2.1)$$

In the above equation, IM is the intensity measure (e.g., peak ground acceleration), EDP is the engineering demand parameter (e.g., ground deformation), DM is the damage measure (e.g., pipe strain), DV is the decision variable (e.g., rate of rupture), λ is the annual rate, the operations of $p\{y|x\}$ and $P\{Y > y|x\}$ are the conditional probability density function (PDF) and

cumulative distribution function (CDF), respectively, of y given x . Given these definitions, λ_{IM} is the annual rate of occurrence of the seismic event, $p\{edp|im\}$ is the probability of a system response computed using geohazard models given the seismic demand, $p\{dm|edp\}$ is the fragility assessment given the system response, and $p\{dv|dm\}$ is the loss estimate given the damage level. The mathematical formulations for $p\{y|x\}$ and $p\{Y > y|x\}$ are given by the following equations, assuming that the random variables X and Y are both lognormally distributed:

$$p\{y|x\} = \frac{1}{\sqrt{2\pi}\sigma_Y y} e^{-\frac{(\ln(y) - (\mu_Y(x) + \sigma_{\mu_Y}\xi))^2}{2\sigma_Y^2}} \quad (2.2)$$

$$P\{Y > y|x\} = 1 - \Phi\left(\frac{\ln(y) - (\mu_Y(x) + \sigma_{\mu_Y}\xi)}{\sigma_Y}\right) \quad (2.3)$$

where $\mu_Y(x)$ is the mean of Y given $X=x$, σ_Y is the aleatory variability, σ_{μ_Y} is the epistemic uncertainty on $\mu_Y(x)$, ξ is a standard normal random variable, and the operator Φ is the error function. Note that $\mu_Y(x)$ represents the engineering models, such as those presented in this report.

In current practice, damage to natural gas pipelines is parameterized as a function of intensity measures (Watson-Lamprey et al., 2020). These simplified fragility curves are easy to develop as they only require estimates of damage and ground shaking intensity, but they are associated with large epistemic uncertainties. By following the PBEE risk methodology, *OpenSRA* is able to incorporate recent scientific advances in our understanding of geohazards, ground response, and the influence of infrastructure characteristics. As additional research is performed, and our understanding continues to improve, this can be incorporated into *OpenSRA* and will lead to reductions in epistemic uncertainty and improved accuracy.

2.2.2 Efficient Evaluation of the PBEE Risk Framework

Risk calculations are typically performed using Monte-Carlo sampling, which may take hours to day to perform a large risk calculation of the type implemented in *OpenSRA*. To develop a user friendly version of *OpenSRA* that runs in significantly less time, a numerical approximation called Polynomial Chaos is implemented. As discussed in Lacour and Abrahamson (2021), the triple integral for the PBEE risk framework presented in Equation (2.1) can be approximated numerically using various traditional quadrature rules (e.g., the rectangle rule or the trapezoidal rule). These numerical methods for integration can be computationally very efficient for evaluating one-dimensional integrals; however, they become exponentially more expensive in computation for evaluating multidimensional integrals.

To reduce the complexity of Equation (2.1), *OpenSRA* implements the three efficient computation methods presented in Lacour and Abrahamson (2021):

1. Simplify Equation (2.1) from a triple integral to three one-dimensional integrals.
2. Approximate the engineering models for $\mu_Y(x)$ using linear functions to compute the integration analytically and avoid numerical integration.
3. Analytically propagate the epistemic uncertainty through the integrals using polynomial chaos approximation, over the traditional Monte-Carlo sampling approach.

2.2.3 Simplification of the Triple Integral to One-Dimensional Integrals

According to Lacour and Abrahamson (2021), one practical property of the PBEE risk equation is that the conditional models of IM, EDP, DM and DV are typically one-dimensional functions of these parameters (e.g., IM is used for the conditioning of the median EDP only, and not additionally for the conditioning of DM and DV). If we enforce these one-dimensional relationships between parameters IM, EDP, DM and DV, we can rewrite the triple integral in Equation (2.1) with one-dimensional integrals:

$$\lambda_{dv} = \int_{DM} P\{DV > dv|dm\} d(dm) * \int_{EDP} p\{dm|edp\} d(edp) * \int_{IM} p\{edp|im\} \lambda_{im} d(im) \quad (2.4)$$

where the first integral is performed over the domain of IM only, then a second integral is performed over the domain of EDP only, and finally a third integral is performed over the domain of DM only. This reduces the computational complexity in the integration from exponential to linear.

2.2.3.1 Analytical Integration using Linear Approximation of Models

As mentioned previously, the conditional probabilities $p\{y|x\}$ and $P\{Y > y|x\}$ in Equations (2.2) and (2.3) are functions of $\mu_Y(x)$ calculated using the damage and fragility models. When the equations for $p\{y|x\}$ and $P\{Y > y|x\}$ are substituted into the simplified PEER risk equation in Equation (2.4), this equation can be solved analytically if the models for $\mu_Y(x)$ are linear. By taking advantage of the analytical solution to calculate risk, the computation time is significantly faster compared to approximation using numerical integration. To do this, we approximate the models for $\mu_Y(x)$ that are used in the risk equation using linear functions given by the following form:

$$\mu_Y(x) \approx a_Y * \ln(x) + b_Y \quad (2.5)$$

where a_Y and b_Y are the slope and intercept for the linear model. For the full derivation and verification of the linear approximation approach, see Lacour and Abrahamson (2021).

2.2.3.2 Polynomial Chaos Approximation for Propagation of Epistemic Uncertainty

Epistemic uncertainty is used to capture the uncertainty in the mean prediction of a parameter. According to Lacour and Abrahamson (2021), epistemic uncertainty in civil engineer problems is traditionally propagated using a brute-force Monte-Carlo sampling approach. For the simplified risk equation in Equation (2.4), this brute force method can be applied to propagate uncertainty by considering separate logic trees for the parameters IM, EDP, DM, and DV (i.e., ξ_{IM} , ξ_{EDP} , ξ_{DM} , and ξ_{DV}) and then sampling each ξ independently. However, this approach requires a large number of samples (i.e., simulations) before the results converge, which is computationally inefficient.

Lacour and Abrahamson (2021) presents polynomial chaos (PC) approximation as an efficient approach to propagate epistemic uncertainty. The method approximates PDFs and CDFs as linear combinations of a set basis functions (analogous to Taylor expansion of analytical functions), which are then incorporated into the analytical solution mentioned in the previous section. The basic forms of the PC expansion for PDFs and CDFs are presented below.

$$p\{x\} \approx \sum_{i=0}^P c_i(x) \Psi_i[\{\xi\}] \quad (2.6)$$

$$P\{X > x\} \approx \sum_{i=0}^P C_i(x) \Psi_i[\{\xi\}] \quad (2.7)$$

where c_i and C_i are the coefficients for the PC expansion, Ψ_i are the known polynomial functions (specifically the Hermite family of polynomial for approximating normal distributions), and P is the number of PC terms to use to approximate the distribution. By substituting these functions into Equation (2.4) for risk, λ_{dv} is now a direct a function of the PC coefficients, the polynomial functions, and just one set of samples for the overall epistemic uncertainty of the entire problem. The primary computation required for PC is the intermediate calculation of the PC terms, which are functions of the various σ_Y and σ_{μ_Y} for IM, EDP, DM, DV, and the linear approximation coefficients for EDP, DM, DV. This set of intermediate calculations is very fast and efficient to perform, as the PC terms are evaluated analytically. Furthermore, the polynomial functions are known mathematical functions, and the sampling of the uncertainty is performed only once during post-processing after the PC terms have been fully computed for all events. Overall, as discussed in Lacour and Abrahamson (2021), the use of PC over traditional Monte-Carlo sampling can easily improve the computation time by two to three orders of magnitude. For additional details to the application of PC to the risk framework and validation examples, please refer to the Lacour and Abrahamson PEER report.

2.2.4 *OpenSRA* Overview

Figure 1 to Figure 3 show the workflow of *OpenSRA* and how the PEER risk methodology shown in Equation (2.4) is conceptually incorporated into the seismic risk assessment of each of the three infrastructure types: below ground pipelines, wells and caprocks, and above ground subsystem components. The PEER risk methodology serves as the backbone to the *OpenSRA* risk assessment workflow. The user defines the infrastructure type that will be analyzed by *OpenSRA* and inputs their component characteristics. *OpenSRA* then steps through the PEER risk methodology as shown in the flow charts in these figures to perform the risk assessment. Figure 4 shows a flow chart of the overall user process for *OpenSRA* and how the PEER risk framework is wrapped into the user experience.

As shown in Figure 1, the workflow for below ground pipelines utilize the full form of the triple integral given in Equation (2.4) in order to capture the influence of seismic intensity on ground deformation, the influence of ground deformation on pipe strain, and finally the influence of pipe strain on the probability of failure in the form of failure and leakage. The models to relate seismic intensity to ground deformation are based on state-of-the-art models that have been published in literature (see Bain et al., 2022). The models to relate deformation to pipe strain and pipe strain to failure are developed as part of the focus of Task B and Task F. These models are described in detail in Section 3.2 and Appendix B.

Figure 2 shows the workflow for wells and caprocks. For this category, Task Groups C and F developed damage models for well casings and tubings that are dependent on fault rupture deformation and ground shaking. These models are considered as two independent modes of failure for wells. Because both branches of the workflow for wells consist of only two integrals, Equation (2.4) is adjusted accordingly to reflect the workflow. For caprocks, results of the numerical study suggest that probability of leakage is not significantly dependent on the tested model parameters, hence its distribution is independent on seismic and geohazard demands, and the overall risk is a constant distribution. Please refer to Section 3.3 and Appendix C for details to the development of these models.

Figure 3 shows the workflow for above ground subsystem components, specifically failure associated with wellheads and pressure vessels. Research by Task D and F resulted in models for joint rotations and strains for wellheads and moment ratios for pressure vessels, both of which are dependent on the seismic intensity (i.e., peak ground acceleration). The intensity of the strains and moment ratios are then used to inform the levels of failure associated with wellheads and pressure vessels respectively. Please refer to Section 3.4 and Appendix D for details to the development of these models.

Figure 1: PEER Risk Methodology Applied to Below Ground Pipelines

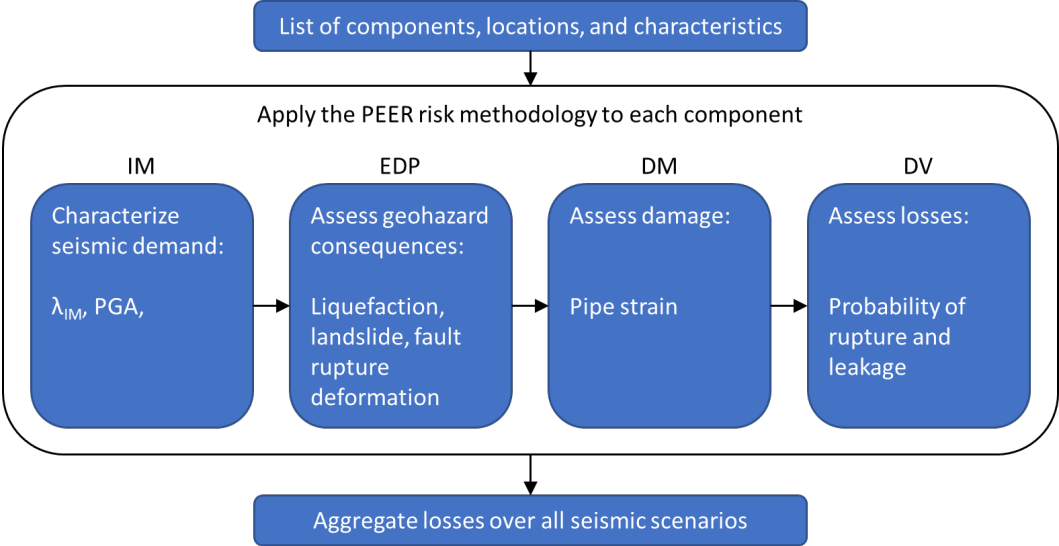


Figure 2: PEER Risk Methodology Applied to Wells and Caprocks

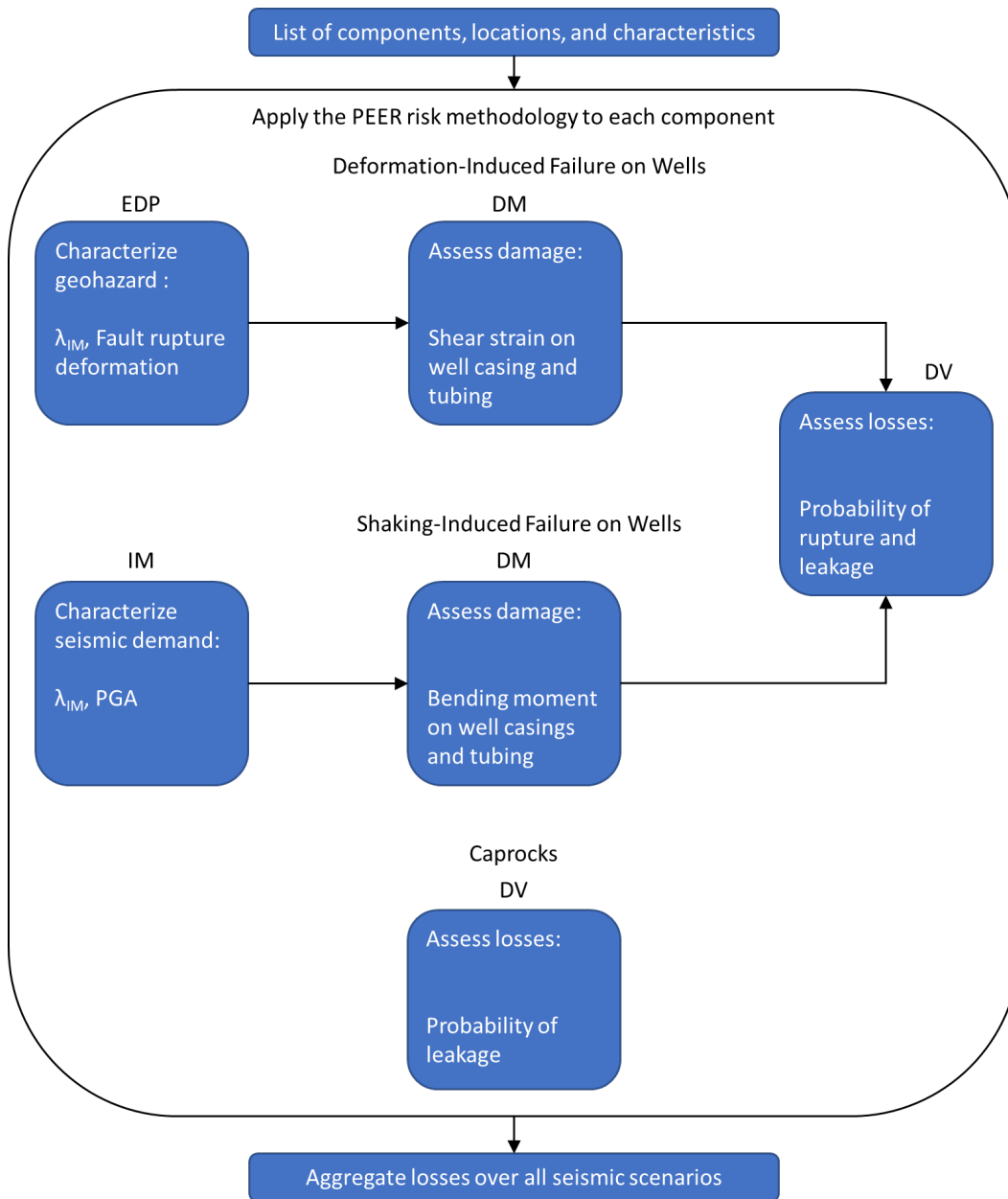


Figure 3: PEER Risk Methodology Applied to Above Ground Components

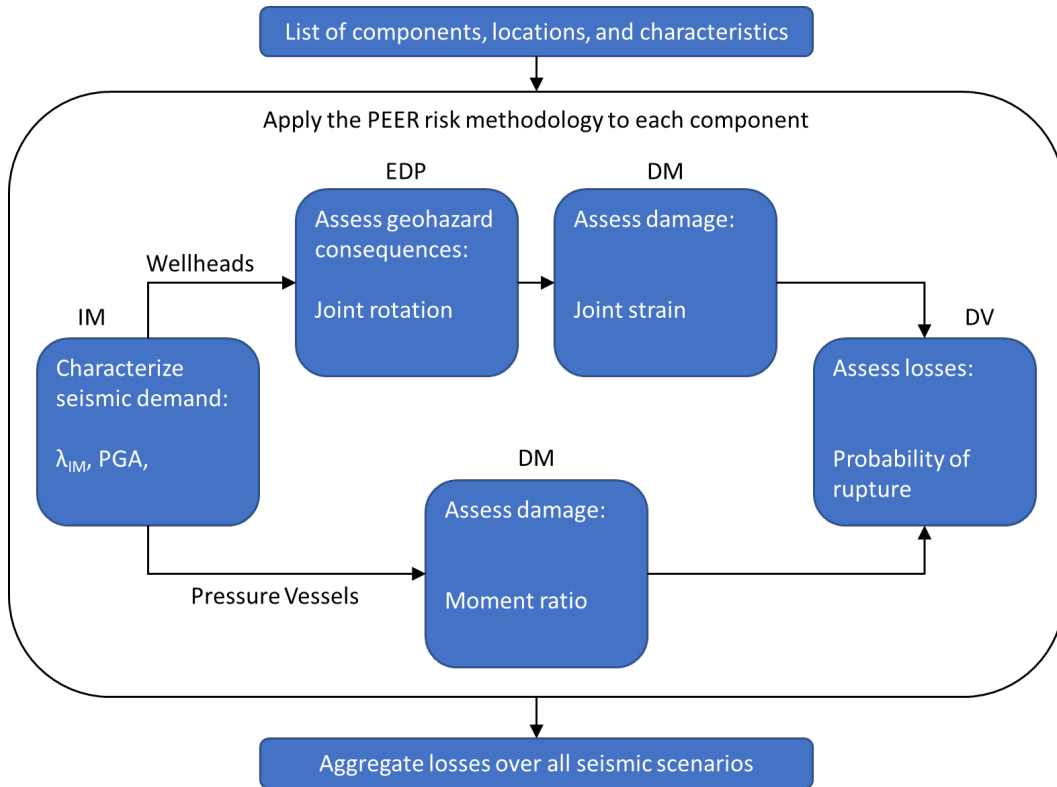
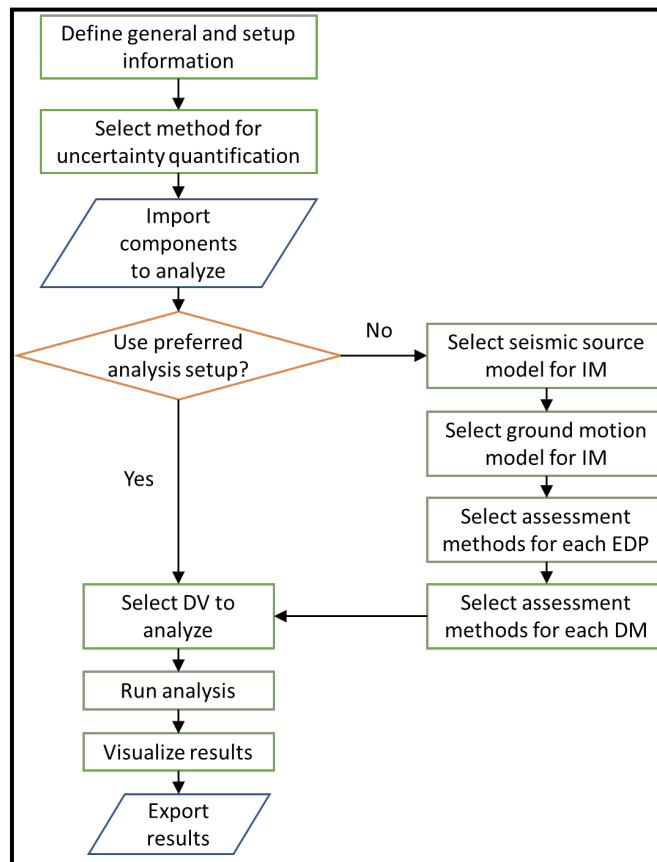


Figure 4: *OpenSRA* User Experience Flow Chart



2.3 Fragility Curve Development

Each research task team followed a similar process to develop the dataset for calculation of the individual damage models and fragility models, collectively referred to as fragility curves. The first step involved developing a base system model using various finite-element (FE) software. The teams then performed sensitivity studies using the base model to identify the parameters that are most significant for predicting system response. Additional finite element analyses were performed to develop a robust database from which fragility curves were estimated.

2.3.1 System Modeling

Each research task team first developed FE models for their specified infrastructure. The groups used publicly available data and previously published reports to develop the FE models. Each of the input parameters was defined as a distribution that was developed through literature reviews. Further information on each individual model can be found in the previously submitted reports (Bain et al., 2022, Rutqvist et al., 2022, and Pantoli et al., 2022).

2.3.2 Sensitivity Studies

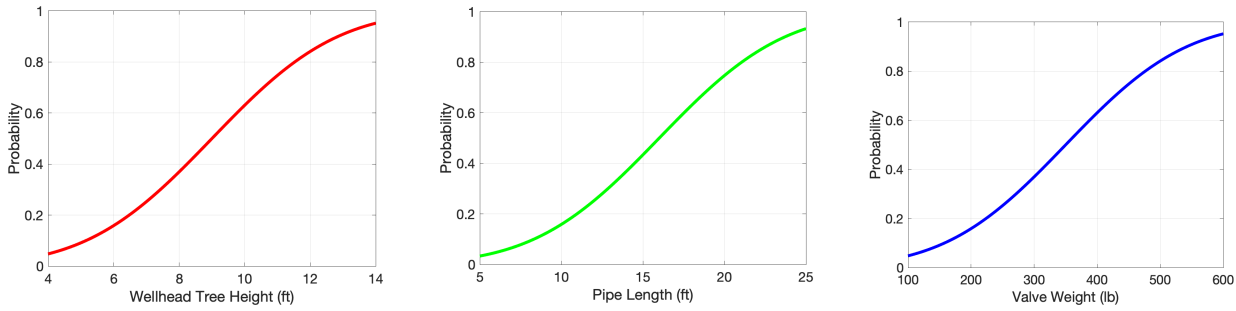
The FE models developed in the first step were used by the teams to conduct sensitivity studies on the system. Each team varied one model parameter at a time to evaluate the change in the system response. The results are presented in tornado plots where each parameter is identified along the y-axis with the amount each parameter changed the final answer (whether that bending moment or strain) plotted along the x-axis (these figures can be found in the appendices). Given the time constraints of this project, the number of analyses performed had to be reduced. To do this the input parameters were ranked by order of impact to the system response. The input parameters that contributed to 95% of the variability in the system response, or the largest number of input parameters that could be modeled in the time available, were used to perform additional analyses.

2.3.2.1 System Modeling Results

Additional FE modeling was then performed using a Latin hypercube sampling (LHS) approach of the key input parameters identified during the sensitivity study. The LHS approach is an efficient, pseudo-random way to select samples in a distribution (Vamvatsikos, 2014). Unlike Monte-Carlo sampling where parameters are sampled completely in random, LHS discretizes the CDFs of the parameters into a number of bins (a hypercube with dimensions equal to the number of parameters) and samples a combination of the bins across all parameters to make sure each bin of the CDFs is captured. This allows the simulations to be more representative of the distribution of each parameter and allows for more efficient run times (order of one magnitude more efficient compared to Monte-Carlo sampling).

For instance, for above ground well trees, the group assigned distributions to three key parameters based on information from the Technical Advisory Committee (TAC) as shown in Figure 5. These distributions were then sampled using LHS, and then earthquakes run through the sampled systems to calculate the rotation of the well tree.

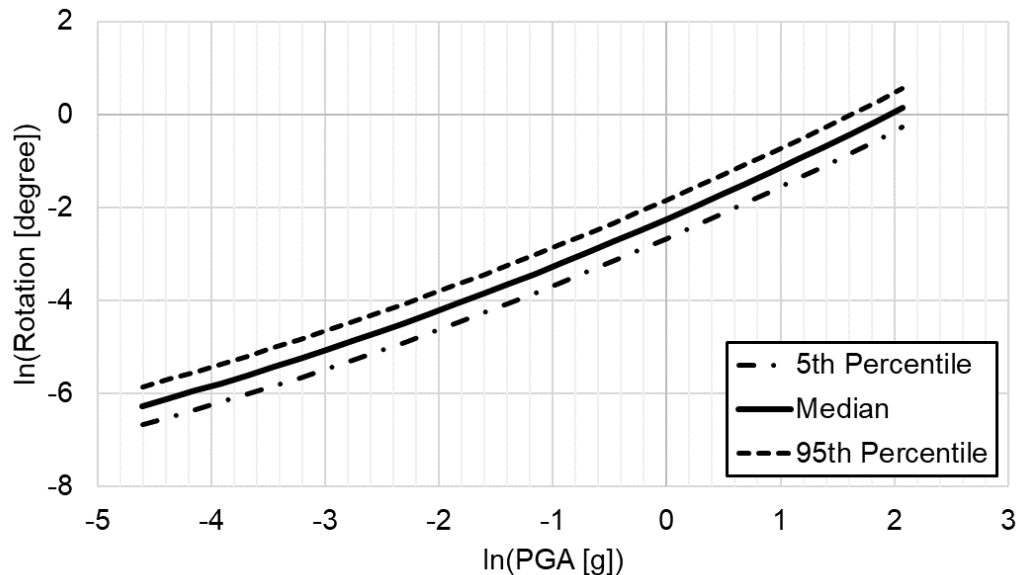
Figure 5: Well tree dimension distributions for Latin Hypercube Sampling



2.3.3 Final Fragility Curves

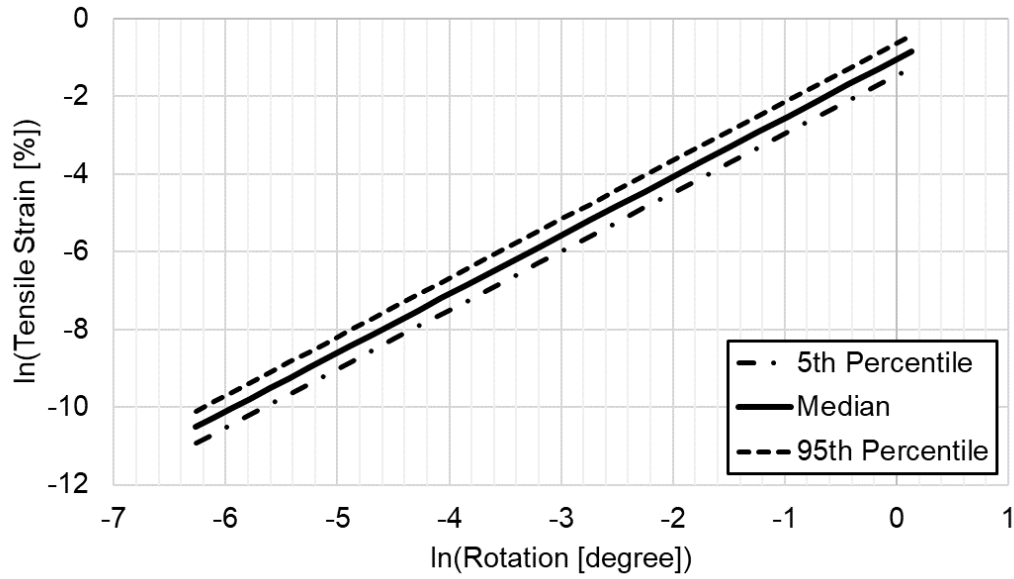
Each team developed fragility curves that are made up of damage models and fragility models. From the above example (Figure 5), a damage model for rotation of elbows and tee-joints for wellheads are developed as a function of the ground shaking intensity (i.e., peak ground acceleration or PGA). A very specific case of the well tree rotation on elbows is shown in Figure 6 for a range of PGAs. This is the “EDP” stage in the upper branch for wellheads in Figure 3. The distribution of rotations is then used to inform the distribution of the tensile strain in the wellheads. A specific case of the strains on elbows is shown in Figure 7. This is the “DM” stage in the upper branch for wellheads in Figure 3. Finally, the tensile strain (or damage) is compared to the mean tensile strain where 50% probability of failure is expected to get a distribution of the probability of failure given the observed (or expected) tensile strain on elbows. An example of the distribution of probability of failure is shown in Figure 8. This is the final step (DV) in Figure 3.

Figure 6: Mean Joint Rotation in Wellheads due to Ground Shaking



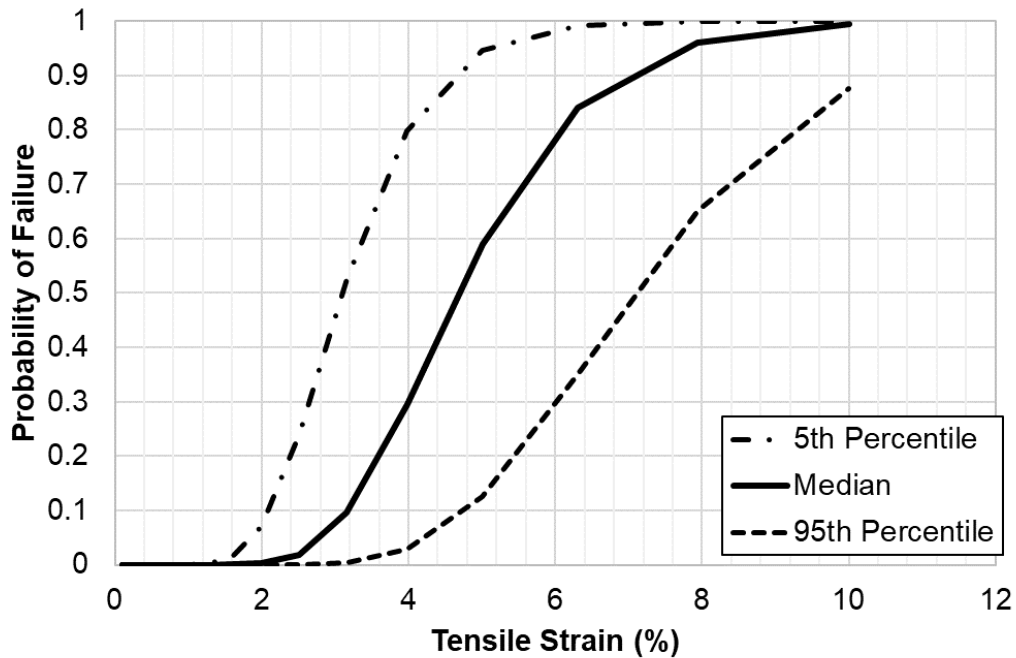
The results shown above assumes 9 feet for wellhead tree height, 16 feet for length pipe segment L6, and valve weight of 350 lbs. The model used is subsystem P4-E (elbows) – y-direction – joint A – closed. An epistemic uncertainty of 0.25 is considered for the 5th and 95th percentiles. See Appendix D for details to this model.

Figure 7: Probability of Failure for Wellheads due to Ground Shaking



The results shown above uses the median rotation values from Figure, along with the damage model for 4E-90 (elbows) with no pressure and closed (negative) configuration. See Appendix D for details to this model.

Figure 8: Probability of Failure for Wellheads due to Ground Shaking



The results shown above uses the failure model in tension as described in Section Error! Reference source not found..

CHAPTER 3:

Project Results

3.1 Introduction

This section outlines the results of the different sensitivity analyses and the subsequent regression analyses resulting in the final damage models and fragility models for each infrastructure component. Further information regarding specific finite element analyses can be found in the previously submitted reports (Thompson et al., 2021, Bain et al., 2022, Rutqvist et al., 2022, and Pantoli et al., 2022).

3.2 Below Ground Pipelines

This section expands on the work of Task B: Enhanced Liquefaction and Ground Deformation (see Bain et al., 2022a). This section presents the finite element modeling that was performed by Task B and the damage models and fragility models that were developed. The finite element computer program Abaqus was used to assess underground pipeline response to four modes of permanent ground deformation: 1) strike-slip tension, 2) strike-slip compression, 3) normal-slip, and 4) reverse-slip. The Abaqus results are the basis for deriving fragility functions to estimate tensile and compressive pipe strain to buried pipelines subjected to permanent ground deformations from fault rupture, landslide displacement, or liquefaction-induced lateral spreading or vertical settlement. A fifth mode of ground deformation where the ground deforms in a direction parallel to the longitudinal pipeline axis resulting in tension at the scarp and compression at the toe was evaluated using an analytical model. Ultimately, the fifth case is confined to be used for only lateral spread where the direction of movement is parallel to the pipeline axis.

3.2.1 Sensitivity Analysis

Details to the derivation and validation of the Abaqus models can be found in Bain et al. (2022a). A sensitivity study was performed to identify the system parameters that most greatly effect the estimated longitudinal pipe strain for each ground deformation mode. A baseline scenario was selected which consists of a 61 cm outside diameter X-52 pipe, buried 1.3 m deep, subjected to 1.0 m of strike-slip tension permanent ground deformation with the assumption that the pipeline-ground deformation zone interaction angle was 50 degrees. Each system parameter was varied by plus- and minus-one standard deviation (σ) from their respective mean (μ) value to assess the sensitivity of the results to reasonable variations of that parameter, as shown in Table 1. The coefficient of variation ($CoV = \sigma/\mu$) of a parameter is used to characterize its uncertainty.

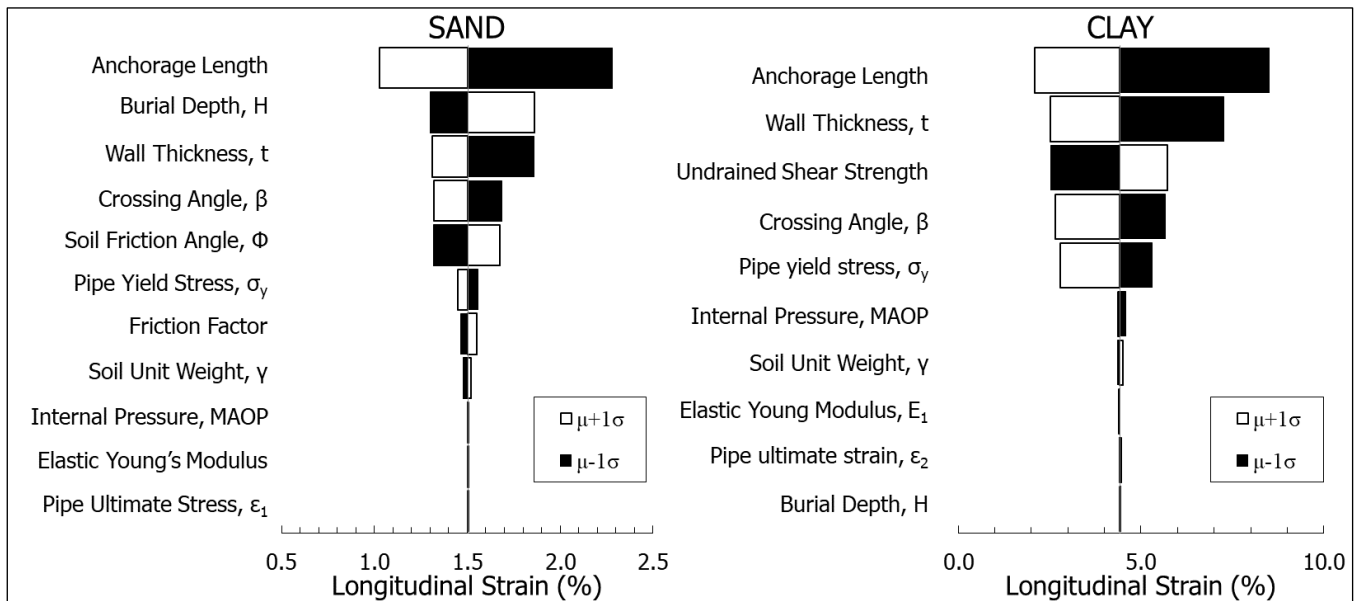
Table 1: List of Parameters Used in Sensitivity Analysis

Parameters	Sand			Clay		
	Base (μ)	CoV	$\mu \pm \sigma$	Base (μ)	CoV	$\mu \pm \sigma$
Pipeline Properties						
Outside Diameter, D (cm)	61.0	-	-	61.0	-	-
Wall Thickness, t (mm)	9.2	30%	6.4 to 12.7	9.2	30%	6.4 to 12.7
Steel Specified Minimum Yield Stress, SMYS (MPa)	358	10%	322 to 394	358	10%	322 to 294
Site & Soil Properties						
Soil Cover, H_c (m)	1.2	30%	0.9 to 1.5	1.2	30%	0.9 to 1.5
Effective Unit Weight, γ (kN/m ³)	18.5	10%	18 to 19	18.5	10%	18 to 19
Soil Friction Angle, Φ (°)	40	8%	37 to 43	N/A	N/A	N/A
Soil-Pipeline Interface Friction Factor, k	0.9	25%	0.8 to 1.0	N/A	N/A	N/A
Backfill Relative Density	Dense	-	Medium Dense to Very Dense	Firm	-	Soft to Stiff
Undrained Shear Strength, s_u (kPa)	N/A	N/A	N/A	50	50%	25 to 75
Fault Properties						
Permanent Ground Deformation, Δ_f (m)	1.0	40%	0.6 to 1.4	1.0	40%	0.6 to 1.4
Pipeline-Ground Deformation Zone Intersection Angle	50	20%	40 to 60	45	22%	35 to 55

Figure 9 shows tornado diagrams for the described pipeline buried in sand and clay and subjected to the described strike-slip tension mode of ground deformation. Tornado diagrams show the sensitivity of the analysis to each variable. The larger the box on the diagram, the greater the sensitivity to that variable.

Based on the results of this study, soil-pipeline systems subjected to permanent ground deformation are typically most sensitive to the anchorage length, soil type and strength (i.e., burial depth and friction angle for pipelines buried in sand and undrained shear strength for pipelines buried in clay), pipe wall thickness, yield stress, the magnitude of permanent ground deformation, and the pipeline-ground deformation zone intersection or dip angle (which is termed the crossing angle).

Figure 9: Tornado Diagrams from Sensitivity Study



Tornado diagrams for soil-pipeline systems subjected to strike-slip tension ground movement where the results are most sensitive to those input parameters that have the widest boxes on the diagram. Results for pipelines buried in sandy soils are shown on the left and results for pipelines buried in clayey soils are shown on the right.

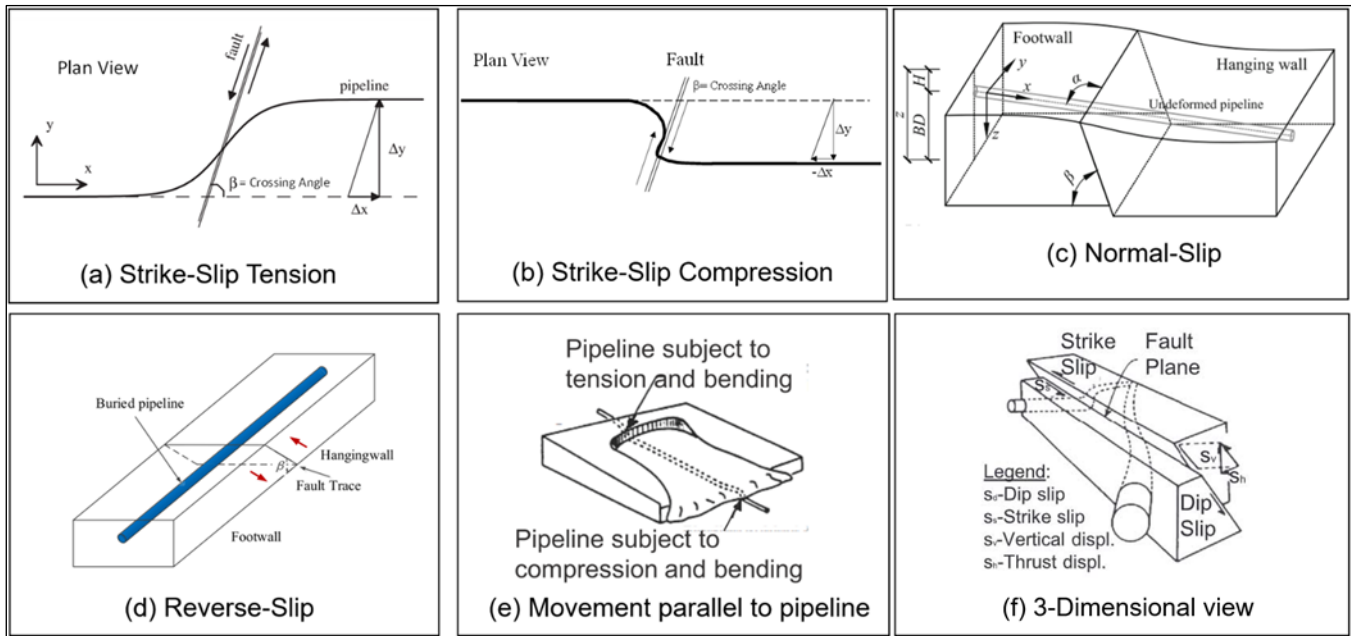
3.2.2 Tensile and Compressive Strain Damage Models

Abrupt permanent ground deformations that pull, compress, or bend pipelines are caused by surface fault rupture or creep, rainfall or seismically induced landslides, liquefaction-induced lateral spreading or vertical settlement, or ground subsidence caused by mining, groundwater extraction, or other reasons. The first step in deriving models for assessing pipe strain for pipelines subjected to permanent ground deformation is to determine the modes of ground deformation to be analyzed. The numerical modeling in this study analyzed only abrupt ground movements. Abrupt (“knife-edge”) ground movements result in locally higher strain concentrations compared to distributed ground movements, which were not studied. The assumption of knife-edge ground movements is appropriate for many practical cases, and it introduces a moderately conservative bias to the pipe strain fragility models for the cases involving distributed ground movements.

Pure strike-slip tension, pure strike-slip compression, pure normal-slip, and pure reverse-slip modes of ground deformation were analyzed using Abaqus for the *OpenSRA* Project. Although each of these modes of ground deformation can have an oblique component of movement, such deformation was not evaluated. Sensitivity analyses indicated that the key aspects of soil-pipeline interaction for a seismic risk assessment are captured with the primary modes of ground deformation employed in this study. A fifth mode of ground deformation where a pipeline crosses a ground deformation zone that displaces parallel to the longitudinal pipeline axis and places the pipeline in pure tension at the landslide or lateral spread scarp and pure compression at the landslide or lateral spread toe without induced bending strains was analyzed using an analytical model presented by O’Rourke & Liu (2012).

Figure 10 summarizes the ground deformation modes assessed for the *OpenSRA* Project. The strike-slip tension (Figure 10a), strike-slip compression, (Figure 10b), normal-slip (Figure 10c), and reverse-slip (Figure 10d) modes of ground deformation were assessed using Abaqus with input parameters provided by Jung et al. (2016) and O'Rourke et al. (2014, 2016). An intermediate "bending" model for the strike-slip and normal-slip modes of ground deformation was employed to transition from ground deformation that induces tension to deformation that induces compression. Movement parallel to the pipeline axis without induced bending strains (similar to Figure 10e) was assessed using an analytical model presented in O'Rourke & Liu (2012). Two-dimensional views of abrupt soil deformation are shown in Figure 10a and Figure 10b, whereas three-dimensional views of same are shown in Figure 10c through Figure 10f.

Figure 10: Assessed Ground Deformation Modes



Ground deformation modes assessed to derive pipe strain fragility models

A summary of the above logic for model selection is shown in **Error! Reference source not found.** For clarity, each of the five models have been assigned a specific mode ID (A through E). Details to the models, such as sensitivity study, functional form, and regression parameters, can be found in Appendix B under the same heading labels as those shown in the list below.

1. Mode A: Pipe Strain Estimation Model for Strike-Slip Tension Ground Deformation;
2. Mode B: Pipe Strain Estimation Model for Strike-Slip Compression Ground Deformation;
3. Mode C: Pipe Strain Estimation Model for Normal-Slip Ground Deformation;
4. Mode D: Pipe Strain Estimation Model for Reverse-Slip Ground Deformation;
5. Mode E: Pipe Strain Estimation Model for Ground Deformation Parallel to Pipeline Axis

3.2.3 Tensile and Compressive Strain Failure Models

Section 3.2.2 described the methodology recommended by Task Group to calculate ground deformation induced longitudinal strains in buried pipes. The final step to the PEER risk framework is to determine the level of failure given the expected pipe strain. The general form for the failure models is given as:

$$Prob(Failure) = \Phi\left(\frac{x - \mu}{\sigma}\right) \quad (3.1)$$

where:

$Prob(Failure)$ is the probability of failure;

Φ is the error function operator;

μ is the mean at which 50% probability of failure is expected;

σ is the aleatory variability of the model;

x is the observation to be compared to the mean.

The following equation is used to capture the epistemic uncertainty in the mean:

$$\mu = \mu_{mean} + \sigma_{epi}\xi \quad (3.2)$$

where:

μ_{mean} corresponds to the 50th percentile of the distribution of the mean;

σ_{epi} is the epistemic uncertainty associated with the mean;

ξ is the standard normal random variable for epistemic uncertainty.

For buried pipelines, the Task Group recommends to separately calculate the probabilities of failure for tension and compression, as the metrics μ_{mean} , σ_{epi} , and σ , may be quite different between the two modes of failures to be combined into one model for failure. Details to the development and the assumptions used for the models are given in the subsequent sections 3.2.3.1 and 3.2.3.2.

3.2.3.1 Tensile Strain Failure Model

For continuous steel pipelines with high-quality, overmatched girth welds subjected to tensile strain caused by permanent ground deformation (PGD), the 1984 ASCE *Guidelines for the Seismic Design of Oil and Gas Pipeline Systems* permit longitudinal strains in the 3–5% range while the 2001 ALA *Guidelines for the Design of Buried Steel Pipe* recommend a tensile strain limit of 2% to maintain normal operability of the pipeline and 4% to maintain pressure integrity. Similarly, the 2004 PRCI *Guidelines for Gas and Liquid Hydrocarbon Pipelines* (Honegger & Nyman, 2004) suggest tensile strain limits of 1–2% for normal operability and 2–4% to maintain pressure integrity. For a natural gas pipeline risk assessment project in British Columbia, Canada, Wijewickreme et al. (2005) use 7% tensile strain as the median value to maintain pressure integrity, with the 90–10% probability of exceedance tensile strains assumed to be 3% and 10%, respectively. Wijewickreme et al. (2005) developed these values with the goal of not being overly conservative after a review of pipeline rupture criterion available at the time, including the ASCE (1984) guidelines.

To develop realistic (and not overly conservative) tensile damage state fragility functions, this study assumes that the 2% pipe strain criterion suggested by ALA (2001) and Honegger & Nyman (2004) to maintain normal operability corresponds to a 30% probability of minor, nuisance leakage and the 4% pipe strain criterion to maintain pressure integrity corresponds

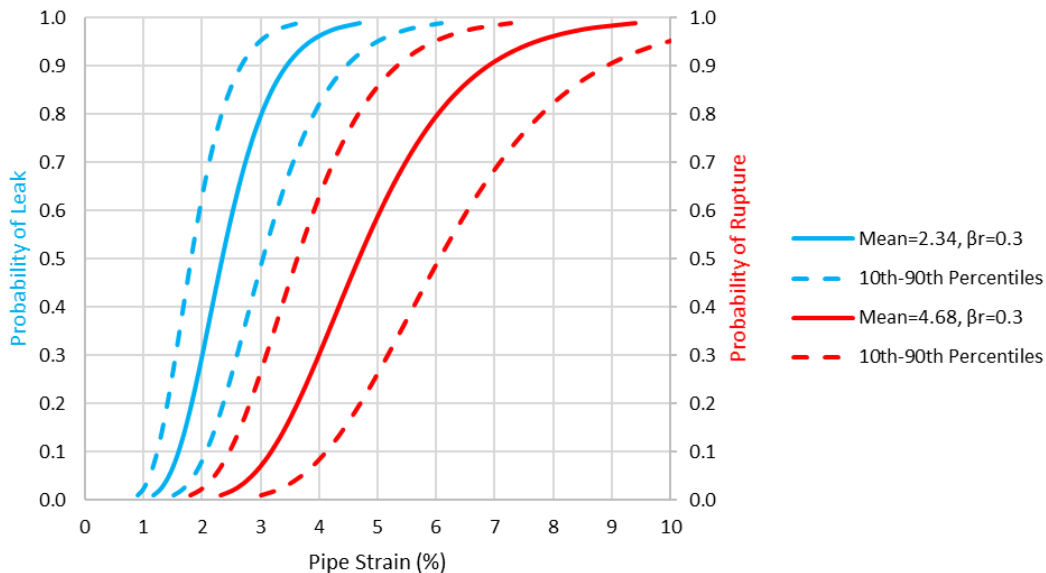
to a 30% probability of pipeline rupture. The typical recommended pipe strain limits of 2 to 4% likely correspond to a small probability of leakage or rupture as would be appropriate for regulatory guidelines. However, because the exact probability of leakage or rupture at 2 or 4% pipe strain is unknown, leakage and rupture were estimated to have 30% probability of occurrence at 2 and 4% pipe strain, respectively, on the basis of expert judgement. The tensile leakage damage state fragility function is presented as Equation (3.3) and the tensile rupture damage state fragility function is presented as Equation (3.4).

$$Prob(Tensile Leakage) = \Phi\left(\frac{\ln(\varepsilon_p) - \mu}{\sigma}\right) \quad (3.3)$$

$$Prob(Tensile Rupture) = \Phi\left(\frac{\ln(\varepsilon_p) - \mu}{\sigma}\right) \quad (3.4)$$

The means (μ) in Equations (3.3) and (3.4) are $-\ln(2.34)$ and $-\ln(4.68)$, respectively, which equates to median strains of 2.34% and 4.68% for 50% probability of failure for onset of leakage and rupture. Figure 11 presents the suggested lognormal cumulative distribution functions (CDFs) for these damage state fragility functions assuming a constant aleatory variability, $\sigma=0.30$, for both leakage and rupture, which was estimated using expert opinion (Abrahamson, 2022). The 10th and 90th percentiles are presented for the fragility functions assuming constant epistemic uncertainty, $\sigma_{epi}=0.20$, for both leakage and rupture, a common assumption for structural systems. σ represents the aleatory variability in the fragility models due to inherent randomness in the loading conditions (e.g., eccentricities in the pipe alignment, nonuniform backfill soil conditions) and pipe properties (e.g., post-yield stress-strain behavior, weld quality, corrosion). σ_{epi} represents the epistemic uncertainty in the mean or median value (i.e., uncertainty resulting from whether the suggested models are the correct models).

Figure 11: Tensile Damage State Fragility Model

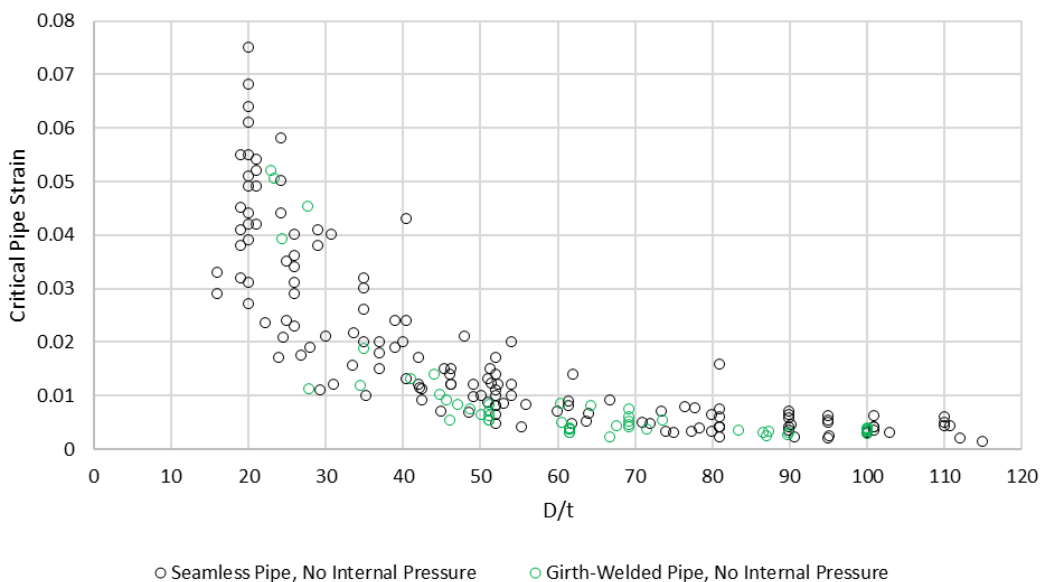


3.2.3.2 Compressive Strain Failure Model

For continuous steel pipelines with high-quality, overmatched girth welds subjected to compressive strain caused by permanent ground deformation, leakage and rupture are often not differentiated. As stated in Wijewickreme et al. (2005), “*The pipe wall response following the onset of compressive wrinkling is complex and it is not well understood in terms of specifying pressure integrity strain limits.*” Buckling itself is therefore taken as the critical damage state because tearing of the pipe wall can occur during buckling and any further straining in the pipe that occurs from permanent ground deformation tends to concentrate at the buckle, dramatically increasing the likelihood of pipe wall tearing or rupture. Mohr (2003) collected the results of published laboratory compressive pipe tests. These are the same data used in pipeline performance studies (e.g., O’Rourke & Liu, 2012). The results of the tests, which are plotted as the critical compressive pipe strain versus the diameter to pipe wall thickness (D/t) ratio, are presented in Figure 12. These data correspond to the longitudinal pipe strain at the maximum compressive stress. According to Harris et al. (1957), buckling occurs at or just before the maximum load the pipe can resist.

The data in Figure 12 were used to derive a compressive pipe strain fragility model that estimates the probability of compressive buckling or pipe wall wrinkling given the D/t ratio and the estimated axial pipe strain. Details regarding the derivation of the compressive pipe strain damage state fragility function are provided in Appendix D in Bain et al. (2022a). See Equation (3.5) for the derived fragility function. Furthermore, the data presented Figure 12 are for pipes without internal pressure. In tension, the effects of internal pressure on the performance of the pipeline are small and it is reasonable to ignore it; however, in compression, the stabilizing effect of internal pressure should be considered. Mohr (2003) recommends a correction factor to convert a pipe strain estimate to a zero-pressure-equivalent pipe strain.

Figure 12: Critical Compressive Pipe Strain Data



Critical compressive pipe strain developed in steel pipe without internal pressure as a function of the pipe diameter (D) to pipe wall thickness (t) ratio (after Mohr, 2003).

The data presented in Figure 12 come from controlled laboratory experiments that should have less uncertainty than that of field conditions. To account for greater uncertainty associated with field conditions, the aleatory variability, σ , is increased from 0.407 to 0.50, as explained in Appendix D in Bain et al. (2022a).

Pipelines can often sustain more axial strain after the initiation of buckling or pipe wall wrinkling before pipe wall tearing or rupturing occurs. The probability of compressive rupture (due to buckling or pipe wall wrinkling) fragility function accounts for this additional capacity by shifting the 50% probability of exceedance values in the original fragility function up to the 20% probability of exceedance level in the final function, as explained in Appendix D in Bain et al. (2022a).

Additional details of the pipeline fragility models are provided in Appendix D in Bain et al. (2022a). Below is the equation for probability of compressive rupture, along with the supplementary equations. Figure 13 plots the 10th, median (50th), and 90th percentiles of the probability of compressive rupture for a number of D/t ratios.

$$Prob(\text{Compressive Rupture}) = \Phi \left(\frac{\ln(\varepsilon_{p-eq}) - \mu}{\sigma} \right) \quad (3.5)$$

Where,

Φ is the error function operator;

$\mu = 1.617 * \ln \left(\frac{D}{t} \right) - 2.130 + \sigma_{epi} \xi$ is the mean;

D/t is the outside pipe diameter to wall thickness ratio;

$\sigma = 0.5$ is the aleatory variability;

$\sigma_{epi} = 0.25$ is the epistemic uncertainty;

ξ is the standard normal random variable;

$\varepsilon_{p-eq} = \frac{\varepsilon_p}{1 + \sigma_h / \sigma_y}$ is zero internal pressure equivalent compressive pipe strain, correction from

Mohr (2003);

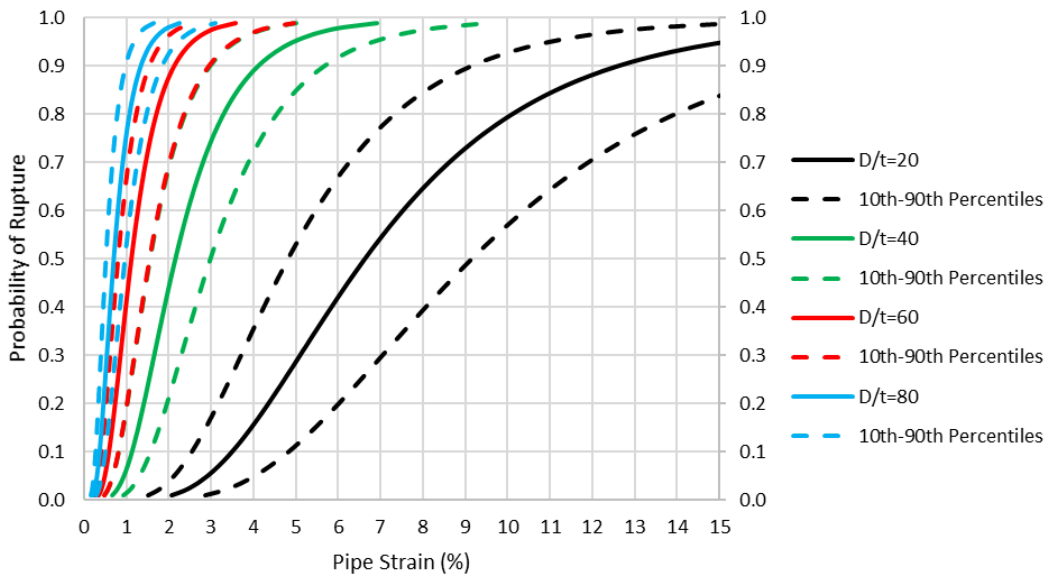
ε_p is estimated compressive pipe strain to computed using the modes in Appendix B;

σ_y is pipe yield stress (kPa);

$\sigma_h = \frac{OP * D}{2 * t}$ pipe hoop stress (kPa);

OP is operating pressure (kPa).

Figure 13: Probability of Compressive Rupture for Select D/t Ratios



3.3 Wells and Caprocks

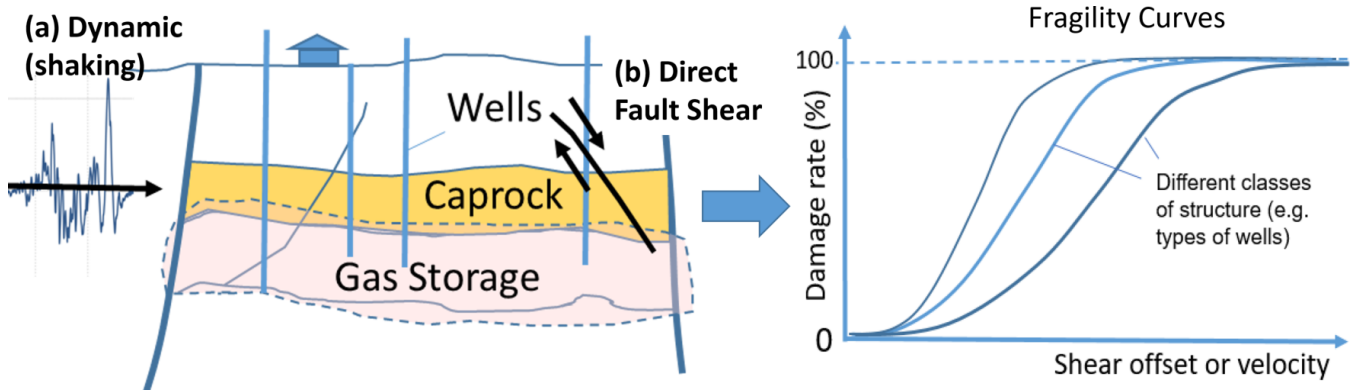
This section expands on the work of Task C: Seismic Response of Wells and Caprocks (see Rutqvist et al., 2022). This section presents the finite element modeling that was performed by Task C and the damage models and fragility models that were developed.

Underground storage facilities are typically much deeper than buried pipelines, as such the failure mechanisms expected are different. This research was split up by component (wells and caprocks) and by failure mechanism. The research was divided into the three modeling subtasks summarized schematically in Figure 14:

1. direct fault shear across wells,
2. ground motion (shaking) impact on wells, and
3. potential caprock gas leakage.

In each of the three subtasks, advanced full-physics modeling was performed for sensitivity and fragility analysis with the goal of providing input that can be used to develop fragility curves, shown Figure 14, for the *OpenSRA* tool.

Figure 14: Fragility Curve Development for UGS Integrity



A schematic of impact of dynamic (shaking) impact and direct fault shear impact on a hypothetical underground gas storage facility (left) that are modeled for input for the development of fragility curve (right).

Source: Lawrence Berkeley National Laboratory (2022)

3.3.1 Fragility of Wells

There are many types of wells and well configurations installed at natural gas reservoirs in California. To reduce the number of wells to be modeled to a reasonable number of analyses to perform in the time allotted for this project, the top four well configuration modes in California were identified by Task D using an assessment of wells in California (Rutqvist et al., 2022). These well configuration modes are outlined in Table 2. The first, second, and fourth modes were selected for analysis of fault shear across wells and seismic shaking. The third mode was not included because it has the same surface casing and tubing as the first mode, but with a one-inch larger diameter production casing. Figure 15 depicts a schematic of an underground well and its components.

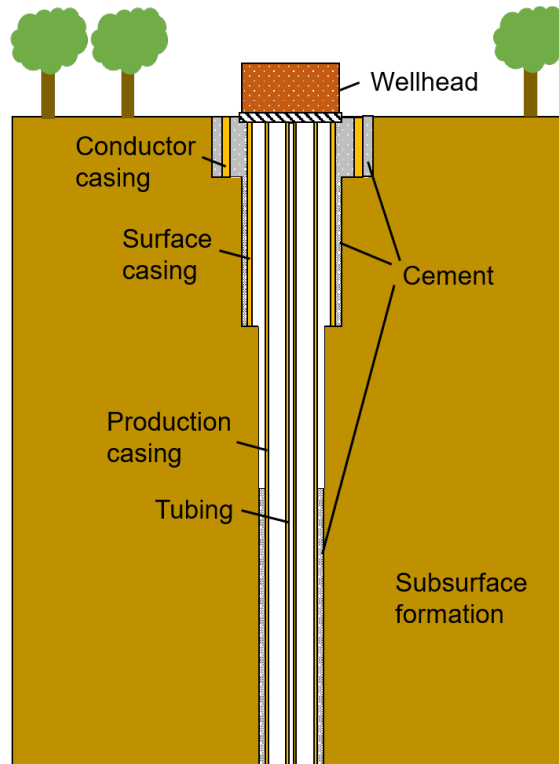
Table 2: Top Four Well Configuration Modes

Mode Well API#	Surface casing				Production casing				Tubing			
	Diam. (in.)	Weight (lb/ft)	Strength (kpsi)	Grade	Diam. (in.)	Weight (lb/ft)	Strength (kpsi)	Grade	Diam. (in.)	Weight (lb/ft)	Strength (kpsi)	Grade
First 03721872	13.375	54.5	55	K	8.625	36	55	K	3.5	9.3	80	L
	13.375	54.5	55	K	8.625	36	55	K	3.5	9.3	80	L
Second 01320115	10.75	40.5	55	K	7	23	55	K	3.5	9.3	55	J
	10.75	40.5	55	K	7	23	55	K	3.5	9.3		
Third 03724130	13.375	54.5	55	K	9.625	47	80	N	3.5	9.3	80	L
	13.375	54.5	55	K	9.625	47	80	N	3.5	9.3	80	L
Fourth 03714070	11.75	54	55	J	6.625	26		C	2.875	6.5	55	J
	11.75	54			6.625	26		C	2.875		55	J

Each well configuration mode is followed by the American Petroleum Institute well number (API#) of a specific gas storage well in California with a configuration equal or close to that mode. API well numbers are unique identifiers for each well in the country. Note the two-digit state code 04 for California (04) starts the full API# but is not shown in the table.

Source: Sasaki et al. (2022)

Figure 15: Typical Gas Storage Well Cross Section (Above Reservoir)



Only the portion of the well above the geologic seal over the gas storage reservoir is shown because damage to this portion of the well could release gas into the surrounding host rock and propagate to the ground surface.

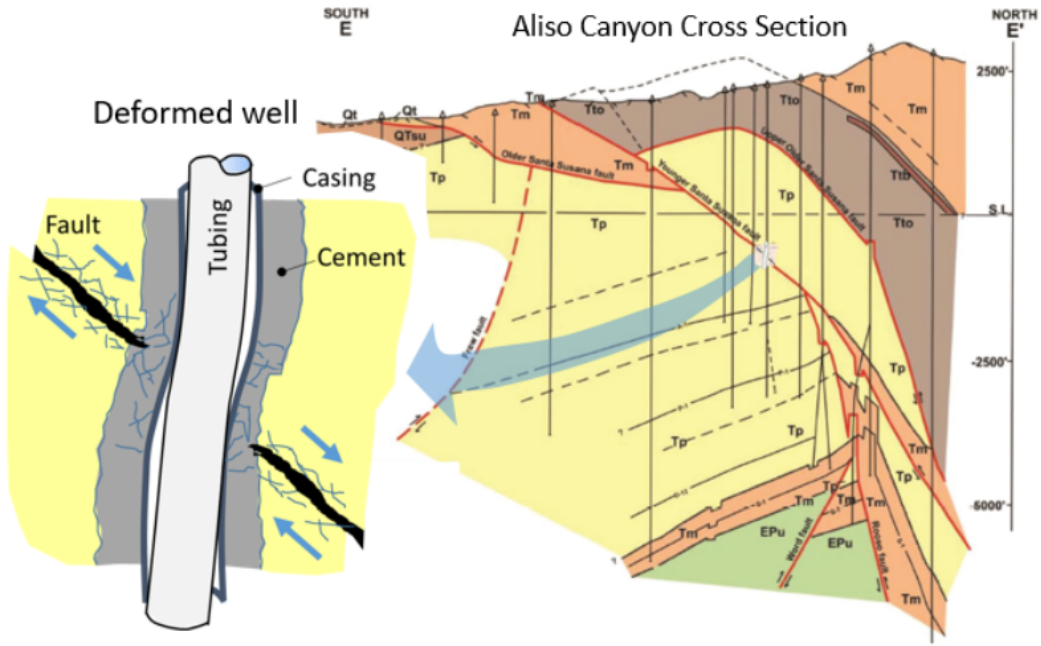
Source: Sasaki et al. (2022)

3.3.1.1 Fault Displacement Damage Models

The first failure mechanism explored, is fault displacement through a well. Figure 16 shows a schematic of this mechanism at Aliso Canyon. When considering this failure, interaction with each component of the well (casing, tubing, and cement) is critical. A finite element model was created to further explore this mechanism and calculate the probability of failure. A commercially available geomechanics software, FLAC3D® (Itasca Consulting Group, 2020), was used for this modeling.

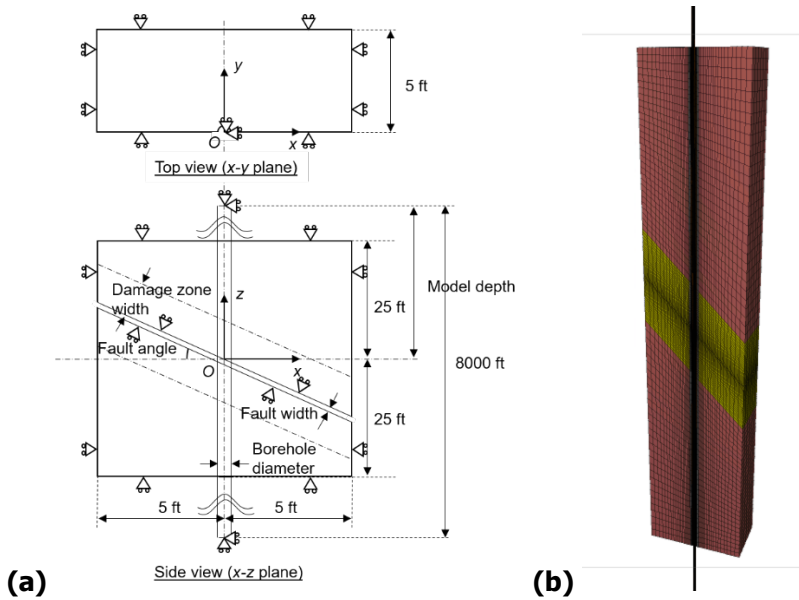
Figure 17 shows the geometry and boundary conditions of the well shear model. The total depth range of the part of the subsurface formation that is modeled mechanically is 50 ft and the width and thickness are both 10 ft. Symmetry permits only half of the model thickness (5 ft) to be modeled. Hence, this is a local well-formation model, assumed to be located at a depth of 4,000 ft. The full model included the well section that extends from the ground surface to the well bottom located at a depth of 8,000 ft.

Figure 16: Depiction of fault shear through a well, at Aliso Canyon



The figure shows a schematic of a well that is damaged by shear along an existing fault but may still be functioning (left). Vertical cross section through Aliso Canyon Gas Storage facility showing vertical wells intersecting faults (right).

Figure 17: The Numerical Model for the Well Shear Simulation



(a) The geometry and boundary conditions of the well shear model; (b) an overview of the model in FLAC3D (brown is intact rock, dark yellow fault zone).

Source: Sasaki et al. (2022)

Sensitivity Analysis

Using the three modes (1,2, and 4) outlined above, a sensitivity analysis was performed to see which parameters impacted the fault shear through a well the most. Table 3 outlines the parameters tested and Figure 45 through Figure 56 in Appendix C show the sensitivity results.

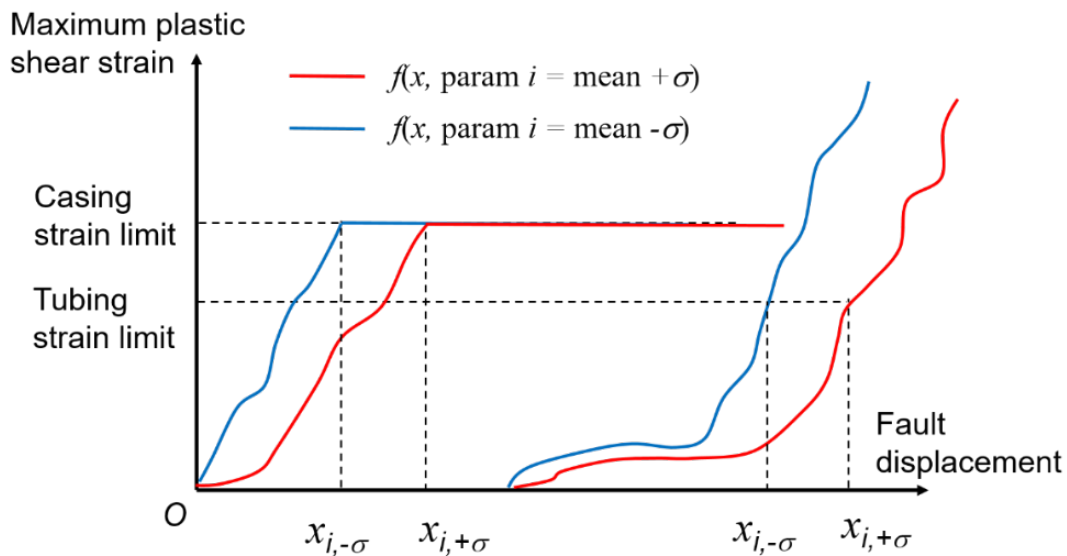
The sensitivity and fragility analyses were carried out to obtain the casing strain and tubing strain as a function of fault displacement as shown schematically in Figure 18. The y-axis shows the maximum plastic shear strains in the casing and tubing and the x-axis is the fault displacement. At a specific casing strain limit, the casing was considered completely failed with a localized fracture simulated by removing numerical elements from casing (Figure 18).

Table 3: Sensitivity Inputs for Fragility of Wells to Fault Displacement

Parameter name	Unit	Mean	Standard deviation (SD)	Coefficient of variation (COV) (%)
Depth (of fault-well intersection)	ft	4000	1500	
Fault core width	m	0.017	1	
Damage zone width	m	1.1	0.5	
Fault angle (dip)	degree	45	10	
Rock Density	kg/m ³	2400	60	
Rock Young's modulus	GPa	11.148	3.9	
Rock Poisson's ratio	-	0.33	0.06	
Rock Internal Friction angle	degree	32.263	1.55	
Rock Tensile Strength	MPa	0.152		30
*Cement Density	kg/m ³	1900		5
*Cement Young's modulus	GPa	16		20
*Cement Poisson's ratio	-	0.25		20
*Cement Internal Friction Angle	degree	25		20
*Cement Cohesion	MPa	60		20
*Cement Tensile strength	MPa	6		30
Casing Density	kg/m ³	7850		1
Casing Young's modulus	GPa	200		6
Casing Poisson's ratio	-	0.3		3
Casing Yield strength	MPa	67.5 (K-55) 95 (N-80)	3 (K-55) 4 (N-80)	
Tubing Density	kg/m ³	7850		1
Tubing Young's modulus	GPa	200		6
Tubing Poisson's ratio	-	0.3		3
Tubing Yield Strength	MPa	67.5 (J-55) 87.5 (L-80)	3 (J-55) 3 (L-80)	
Interface friction angle	degree	33.4	2.3	
Maximum principal stress	MPa	33.489	4.186	
Casing pressure	psi	1005	659	
Tubing pressure	psi	1426	602	
Mud Density	lb/gal	9.25	0.13	

In total, the impact of 27 (for cemented) and 22 (for uncemented) parameters [YY1] on the well damage during well shear was investigated in the sensitivity analysis for the cemented and uncemented annuli scenarios, respectively. (The remaining five parameters for each uncemented case were either held constant or their sensitivity effects were accounted for by other parameters.) It should be noted that 21 of the 28 listed parameters listed in Table 3 were used in both the cemented and uncemented cases. There are 6 additional parameters for the cemented case (denoted with "*" in Table 3), and 1 additional parameter for uncemented (which is, Mud Density). The results of the sensitivity analysis identified the critical parameters effecting well damage (i.e., accumulation of plastic shear strain), and the variability of only those parameters was incorporated into the fragility analysis to estimate how well damage varies with fault displacement. The results of the fragility analysis are provided in a later section of this report.

Figure 18: Outputs of the Well Shear Analysis



The red and blue curves indicate the maximum plastic shear strain profiles when the value of a single parameter (i.e., param i) was changed by $+1\sigma$ and -1σ from its mean, respectively.

Source: Sasaki et al. (2022)

Each of the following sensitivity analyses are split up first by mode and then by component (i.e., casing or tubing) – the results can be found in Appendix C. The sensitivity analysis showed that fault angle ranked highest in all analyses, but that when there is no cement the strain in the well is impacted by fewer parameters.

These key input parameters were then used to develop the damage model for strain of a well due to fault shearing. Using the models outlined in Table 4, Latin Hypercube Sampling was used to run 37 simulations for each mode. These simulations were then used to develop the damage model presented in Appendix C.

Table 4: Cases used for Latin Hypercube Sampling

No.	Case Description
1	First Well Mode – cement – casing
2	First Well Mode – cement - tubing
3	Second Well Mode – cement – casing
4	Second Well Mode – cement - tubing
5	Fourth Well Mode – cement – casing
6	Fourth Well Mode – cement – tubing
7	First Well Mode – no cement – casing
8	First Well Mode – no cement - tubing
9	Second Well Mode – no cement – casing
10	Second Well Mode – no cement - tubing
11	Fourth Well Mode – no cement – casing
12	Fourth Well Mode – no cement - tubing

3.3.1.2 Fault Displacement Failure Model

The probability of fault offset induced failure on wells is given by Equation (3.6) and is plotted in

Figure 19 for both well casings and tubings. The median shear strain at which 50% probability of failure occurs is derived from the strains at failure from the numerical simulations.

$$Prob(\text{fault offset induced failure}) = \Phi\left(\frac{\ln(\gamma) - \mu}{\sigma}\right) \quad (3.6)$$

Where:

γ is the fractional shear strain in the well component computed using the damage models in Appendix C;

$\mu = \bar{\mu} + \sigma_{epi}\xi$ is the mean fractional shear strain corresponding to 50% probability of failure;

$\bar{\mu}$ is the median of the distribution of the mean where 50% probability of failure is expected, given in Table 5;

σ is the aleatory variability for μ , given in Table 5;

σ_{epi} is the epistemic uncertainty for $\bar{\mu}$, given in Table 5;

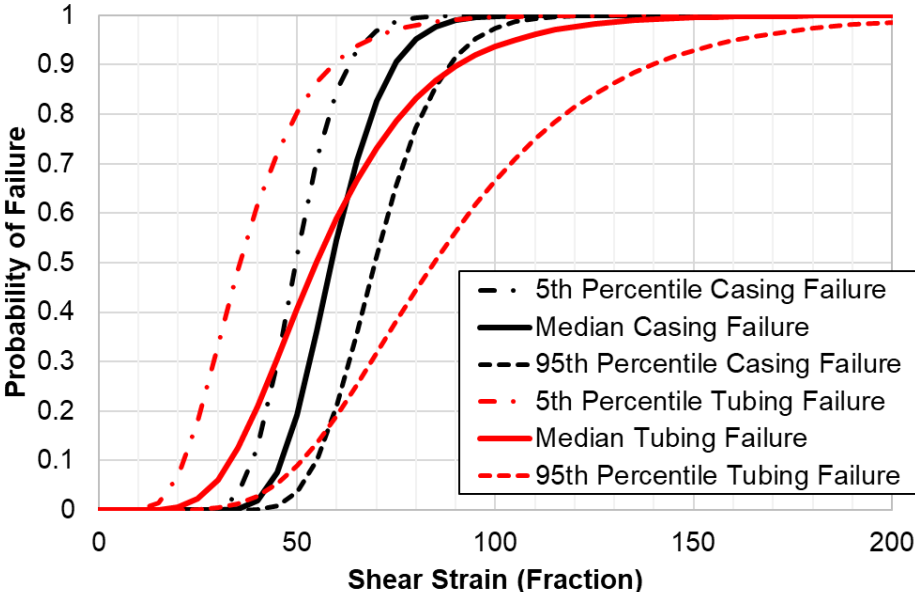
Φ is the error function operator;

ξ is the standard normal random variable for the epistemic uncertainty;

Table 5: Metrics for failure model for fault offset induced well failure

	Casing	Tubing
$\bar{\mu}$	4.073	4.005
σ	0.186	0.392
σ_{epi}	0.103	0.261

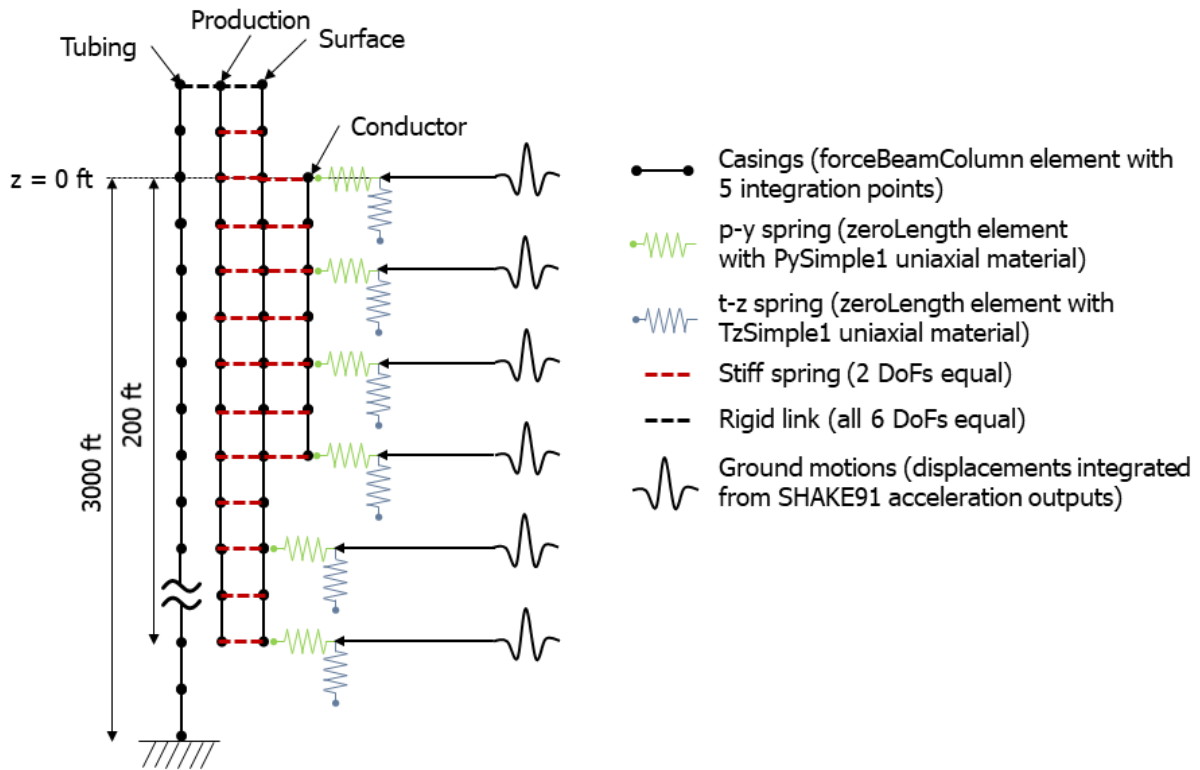
Figure 19: Probability of Failure for Well Casing and Tubing due to Fault Offset



3.3.1.3 Fragility of Wells Subject to Ground Shaking

Similar to fault shearing through a well, Task C developed a finite element model to predict the effects of ground shaking on a well. Similar to fault shearing through a well, Task C developed a finite element model to predict the effects of ground shaking on a well. Figure 20 depicts the model developed in OpenSees.

Figure 20: Finite-Element Conceptual Model Used in OpenSees



Source: Luu et al. (2022)

Sensitivity Analysis

Similar to the other sensitivity analyses performed, this analysis tested the parameters in the model to find the key parameters in ground shaking of wells. Each parameter was assigned a nominal value (mean) and an increment to which it was changed (standard deviation). Table 6 shows the mean and standard deviation of 15 of the 24 [YY2] parameters (the additional 9 are each individual pipe's materials using the mean and standard deviations provided).

In light of the results of the sensitivity analysis, five key parameters were selected to carry out the seismic loading analysis, namely the angle of internal friction of the soil, the height and mass of the wellhead, and the tubing's Young's modulus and yield strength, since these parameters account for most of the variability of the model outputs for both weaker and stronger ground motions. The full sensitivity analysis can be found in Appendix C.

Table 6: Nominal and Increment Values for Parameters Related to Soil

Parameter	Mean	Standard Deviation
Soil Density (kg/m ³)	2000.0	200.0
Soil Angle of internal friction (°)	36.0	3.0
Wellhead mass per length (lb/in)	60.0	5.0
Wellhead height (ft)	10.0	3.0
Density (kg/m ³)	7850.0	78.5
Young's modulus (GPa)	200.0	12.0
Poisson's ratio (-)	0.3	0.01
Conductor Casing Yield strength	67.5 (K55)	3.0
Conductor Casing Young/Tensile	0.8 (K55)	0.02
Surface Casing Yield strength (Ksi)	67.5 (K55) / 67.5 (J55)	3.0
Surface Casing Young/Tensile	0.8 (K55) / 0.8 (J55)	0.02
Production Casing Yield strength	67.5 (K55) / 95.0 (N80)	3.0
Production Casing Young/Tensile	0.8 (K55) / 0.875 (N80)	0.02
Tubing Yield strength (Ksi)	87.5 (L80) / 67.5 (J55)	3.0
Tubing Young/Tensile strength	0.875 (L80) / 0.8 (J55)	0.03

3.3.1.4 Ground Shaking Damage Model

The sensitivity analysis showed that the maximum bending moments recorded along the casing system are primarily affected by a set of three parameters for all the casings and the tubing, namely the angle of internal friction of the soil, and the height and mass of the wellhead. In addition, the bending moment of the tubing is also sensitive to its Young's modulus and yield strength. In order to sample the parameter space for each ground motion, for the three well configuration modes, and within the time constraints of this project 100 Latin Hypercube samples were chosen. Resulting in a total of $100 \times 3 \times 60 = 18,000$ simulations performed.

The results of the Latin hypercube sampling were then used to develop the damage models. Models for the following well modes and components are outlined in Table 7 and can be found in Appendix C.

Table 7: List of damage models created for shaking of a well

Well Mode	Component
First Well Mode	Conductor Casing
	Production Casing
	Surface Casing
	Tubing
Second Well Mode	Conductor Casing
	Production Casing
	Surface Casing
	Tubing
Fourth Well Mode	Conductor Casing
	Production Casing
	Surface Casing

3.3.1.5 Ground Shaking Failure Model

The probability of ground shaking induced failure on wells is given by Equation (3.7) and is plotted in

Figure 21 through Figure 24 for the conductor casing, production casing, surface casing, and well tubings. The median plastic moment at which 50% probability of failure occurs is compiled and estimated by the Task C researchers.

$$Prob(\text{shaking induced failure}) = \Phi\left(\frac{\ln(M) - \mu}{\sigma}\right) \quad (3.7)$$

Where:

M is the maximum moment (N-m) in the well component computed using the damage models in Appendix C;

$\mu = \bar{\mu} + \sigma_{epi}\xi$ is the mean plastic moment (N-m) corresponding to 50% probability of failure;

$\bar{\mu} = \ln(M_p)$ is the median of the distribution of the mean where 50% probability of failure is expected, given in Table 8;

σ is the aleatory variability for μ , given in Table 8;

σ_{epi} is the epistemic uncertainty for $\bar{\mu}$, given in Table 8;

Φ is the error function operator;

ξ is the standard normal random variable for the epistemic uncertainty;

Table 8: Metrics for failure model for shaking induced well failure

	Conductor Casing	Surface Casing	Production Casing	Tubing
First well mode M_p (N-m)	1311917	564045	211194	27913
Mode 2 M_p (N-m)	1311917	300336	109907	21532
Mode 4 M_p (N-m)	1066185	435757	162947	12302
σ	0.2	0.2	0.2	0.2
$\sigma_{\ln(M_p)}$	0.25	0.25	0.25	0.25

Figure 21: Probability of Failure for Conductor Casing due to Ground Shaking

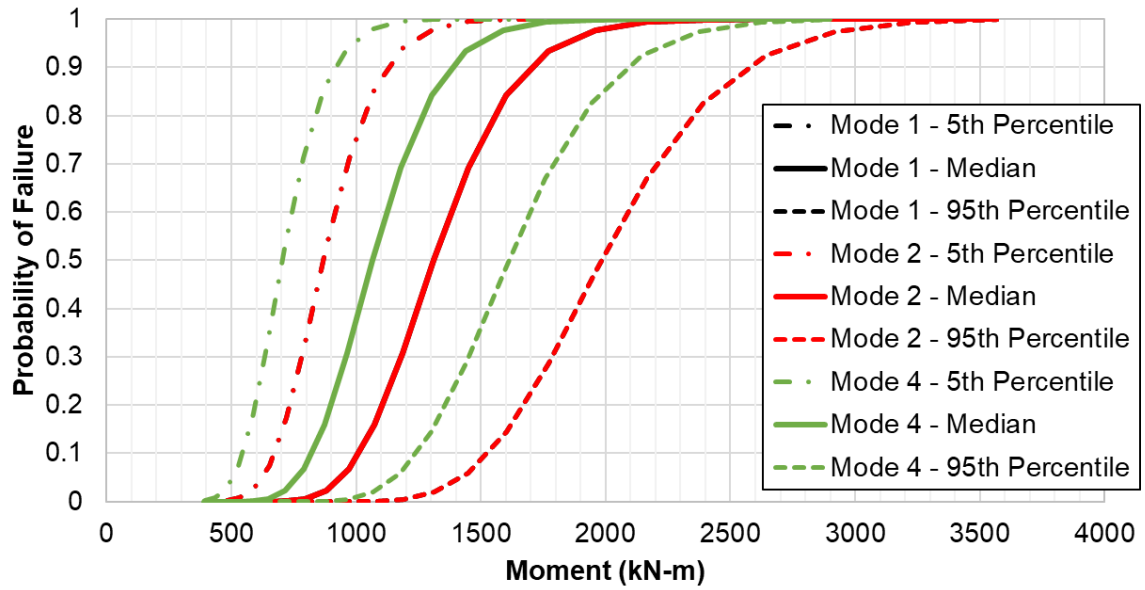


Figure 22: Probability of Failure for Surface Casing due to Ground Shaking

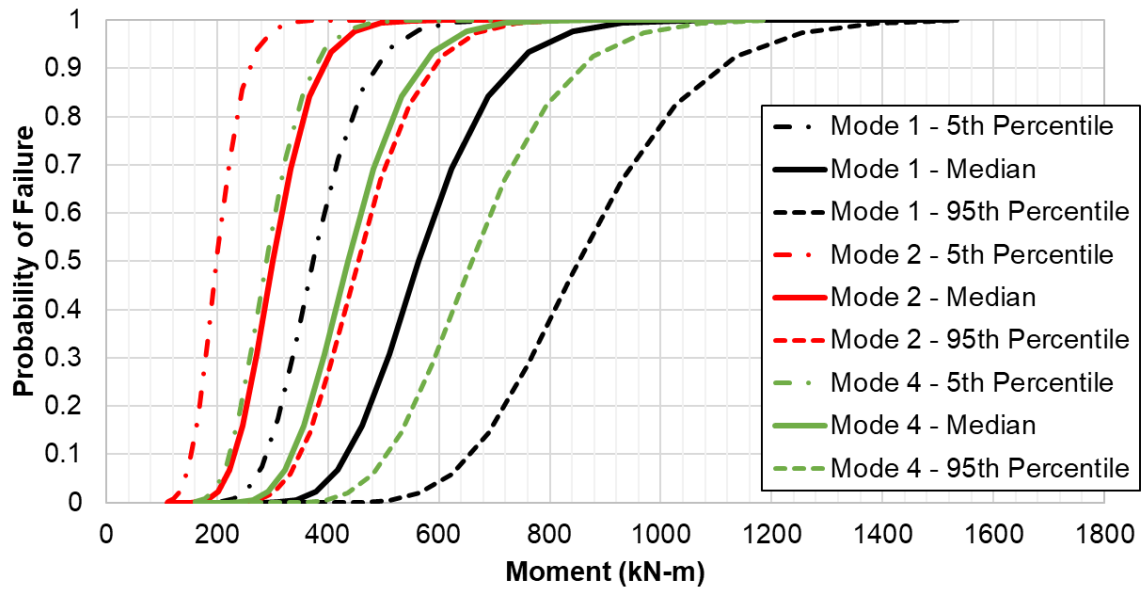


Figure 23: Probability of Failure for Production Casing due to Ground Shaking

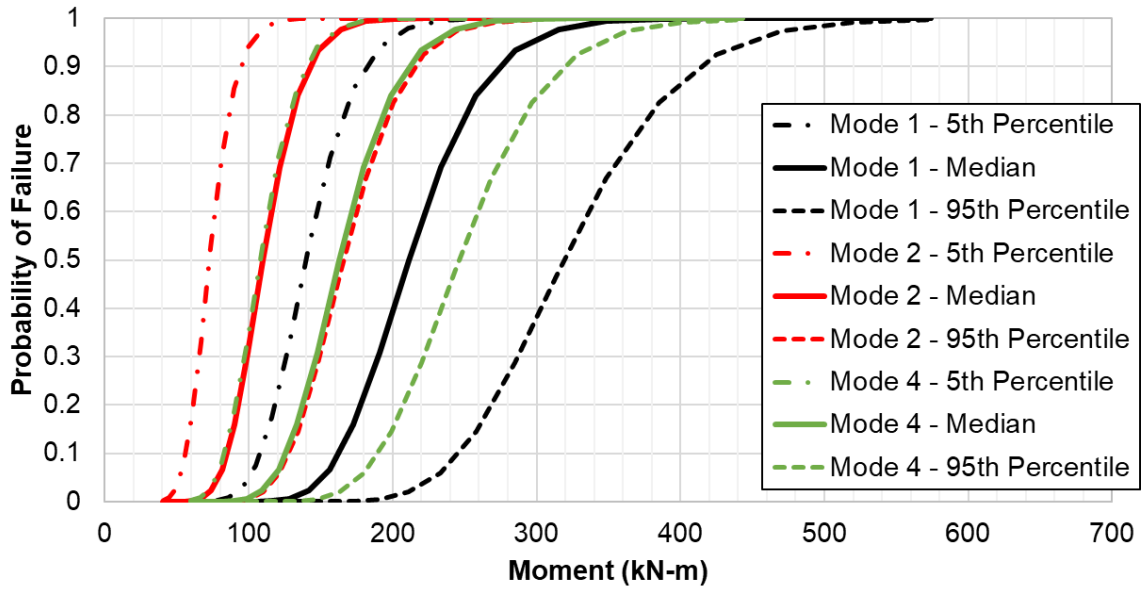
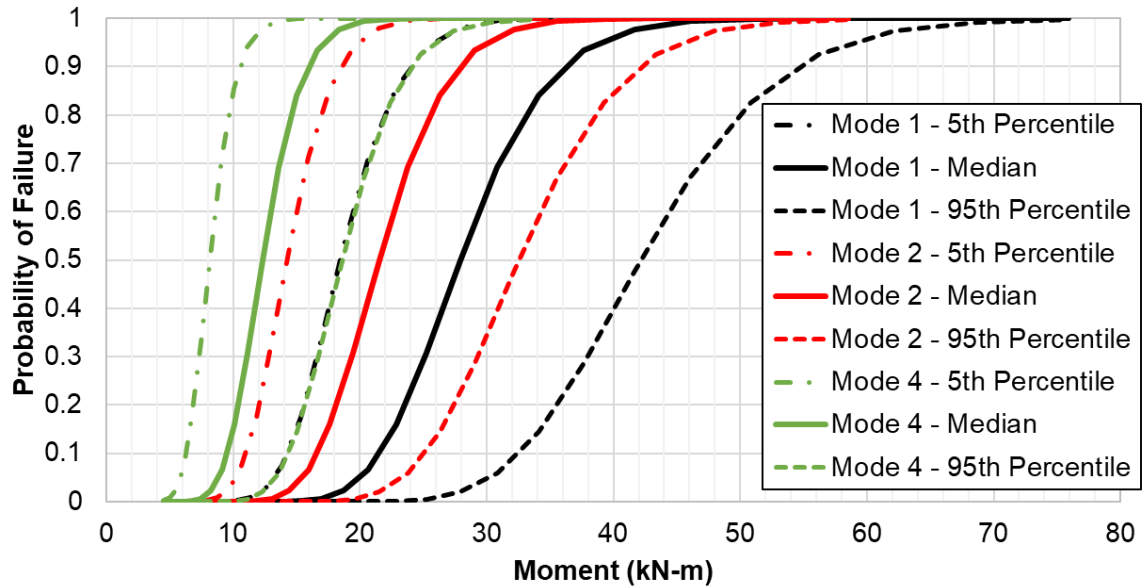


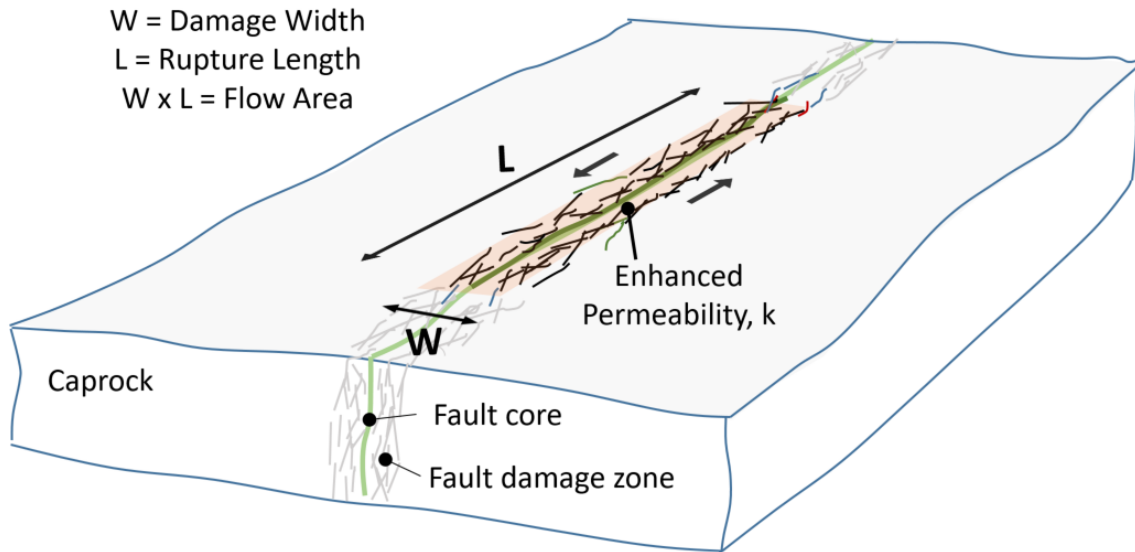
Figure 24: Probability of Failure for Tubing due to Ground Shaking



3.3.2 Fragility of Caprocks

Details to the modeling approach for leakage out of caprocks can be found in the previous CEC report by Rutqvist et al. (2022). The conceptual model for modeling of the upward flow through the caprock is shown in Figure 25.

Figure 25: Conceptual Model of Flow Area of an Activated Fault Crossing a Caprock



Fault transmissivity for vertical flow through the caprock is defined as the permeability multiplied by the flow area, where flow area is damage width (W) multiplied by the rupture length (L).

Source: Zhang et al. (2022)

Sensitivity Analysis

The fragility of caprocks includes six parameters, as such it was not necessary to perform a sensitivity analysis. The six parameters and their ranges are included in Table 9.

Table 9: Parameters for caprock fragilities and their range

Uncertain parameter	Mean	Range
Dslip (m)	0.3	0.2 – 0.5
Pressure (Pa)	7.18E6	6.40E6 – 8.93E6
Reservoir Gas saturation	0.7	0.6 – 0.80
Log (Fault permeability(m ²))	-16	(-16) – (-14)
VG - Log (1/P0) ^[1]	-6.0	(-7) – (-5)
VG – m parameter ^[2]	0.45	0.3 – 0.6

Combined Damage and Failure Model

During the regression analysis it was found that the tested parameters do not show significant influence on the probability of leakage for caprocks. The average probability of leakage for caprocks is 8.9%, with σ_{epi} of 0.86% from the regression analysis.

$$P_{Leakage} = 8.9\% \quad (3.8)$$

3.4 Above Ground Infrastructure

This section expands on the work of Task D: Performance of gas storage and pipeline system surface infrastructure (see Pantoli et al., 2022) and presents the finite element modeling that was performed by Task D and the damage models and fragility models that were developed.

Most of the systems of the surface natural gas infrastructure, as well as similar industrial systems and lifelines, have performed well during past earthquakes. However, some have repeatedly exhibited seismic vulnerability. For example, earthquake damage to industrial facilities including toppling of tall and heavy vessels or pieces of equipment, damage to pipe-to-vessels connections and damage to liquid-filled tanks are amongst the more common vulnerabilities observed. It is noted that many of these observations are not specific to California, since the State has not had a major earthquake in decades. Because of this, it is unknown whether some of the newer technologies used in California might have additional vulnerabilities. More information regarding the analyses and lab testing performed for this project can be found in Pantoli et al. (2022). The fragility development portion of this project focused on well trees at natural gas plants and large pressure vessels.

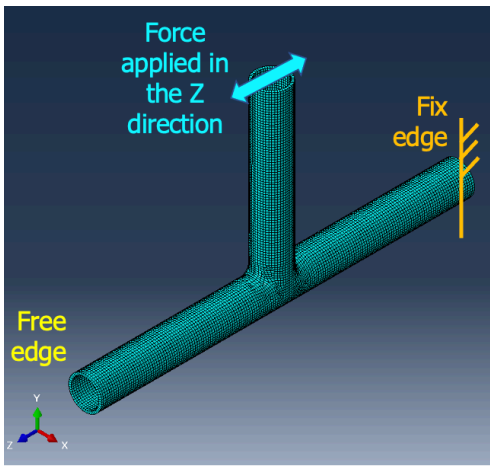
3.4.1.1 WTP subsystem: Tees and Elbows

The critical components selected for the well trees and connecting piping (WTP) subsystem were in-plane and out-of-plane tees and in-plane elbows with 4-inch diameter Schedule 80 pipe. These types of pipes were selected because they were identified as typical of gas storage facilities, according to literature and discussion with utility owners. This model requires the assignment of the following parameters:

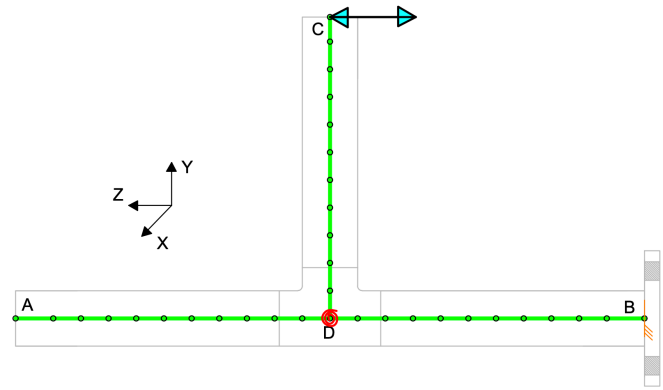
- f_y : yield strength
- E_0 : initial stiffness
- b_k : hardening ratio
- R_0, r_1, r_2 : parameters controlling the exponential transition from linear elastic to hardening asymptote.

Figure 26 shows an example of two of the models used for the fragility development of tee-joints. The parameters that were considered key based on literature or advice from our technical advisory committee (TAC) are outlined in Table 10.

Figure 26: Component models for the tee rotating in-plane



(a)



(b)

(a) Abaqus model, (b) OpenSees model

Table 10: Configurations of WTP subsystem, variables considered and EDP

Conf.	Comp.	Schematic and name	Variables	Dir.*	EDP
P2	Elbow		<p>X₁) Tree Height H_t ($\mu=9$ feet, $\sigma= 3$ feet)</p> <p>X₂) Length of pipe Sh1 L_{p1} ($\mu=5$ feet, $\sigma= 3$ feet)</p>	X	θ_A (in-plane)
				Y	θ_A (in-plane)
	Tee		<p>X₃) Length of pipe Sh2 L_{p2} ($\mu=10$ feet, $\sigma= 6$ feet)</p>	X	θ_A (in-plane)
				Y	θ_A (in-plane)
P3	Elbow		<p>X₁) Tree Height H_t ($\mu=9$ feet, $\sigma= 3$ feet)</p> <p>X₂) Length of pipe Sh1 L_{p1} ($\mu=5$ feet, $\sigma= 3$ feet)</p>	X	θ_B (in-plane)
				Y	θ_A (in-plane)
	Tee		<p>X₃) Length of pipe Sh2 L_{p2} ($\mu=10$ feet, $\sigma= 6$ feet)</p>	X	θ_A (out-of-plane) θ_B (in-plane)

Conf.	Comp.	Schematic and name	Variables	Dir.*	EDP
				Y	θ_A (in-plane)
P4	Elbow		<p>X₁) Tree Height H_t ($\mu=9$ feet, $\sigma= 3$ feet)</p> <p>X₂) Length of pipe Sh2 L_p ($\mu=16$ feet, $\sigma= 6$ feet)</p> <p>X₃) Weight of valves W_v ($\mu=350$ lb, $\sigma= 150$ lb)</p>	X	θ_B (in-plane) θ_C (in-plane)
				Y	θ_A (in-plane)
	Tee			X	θ_A (out-of-plane) θ_B (in-plane) θ_C (in-plane)
				Y	θ_A (in-plane) θ_C (out-of-plane)

*Dir. = direction of the input excitation

3.4.1.2 Pressure Vessels: Base Connection



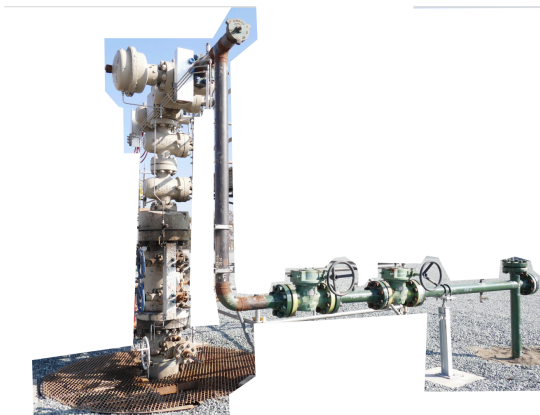
For the pressure vessels, the critical component considered was the base of the pressure vessel. Two types of base connections were considered. The first represents the configuration of older pressure vessels, in which the base anchors are embedded in a concrete footing and thus designed as a fully fixed connection. In this case, no elongation of the anchor will occur, and minimal base rotation is anticipated, consequently the base of these pressure vessels is considered fixed. The second configuration is typical of newer pressure vessels. In this case, the anchors have a designed free stretch length of at least eight times the diameter of the anchor, as recommended by ACI 318-19 (2019). This allows the base to rotate, hence a nonlinear spring is incorporated in the model at the base of the vessel, as shown in Figure 29b. The behavior of this spring was assumed to be elastoplastic with nominal strain hardening of mild steel (e.g. common anchorage material of grade A36 steel is utilized in practice). The yield moment and rotation were obtained from the geometry and material properties of the pressure vessel and anchors.

3.4.2 Damage Model for Wellheads to Ground Shaking

The well tree systems analyzed were split into three configurations and two components. Figure 27 depicts the three configurations and highlights their differences. Based on the literature review a distribution (mean and standard deviation) were assigned to each of the input parameters. 15 combinations of the input parameters were created based on existing well trees. 63 earthquakes were chosen to sample possible ground motions and scaled by four different scale factors, resulting in (63x15x4) 3780 samples.

The Latin Hypercube Sampling results were used to develop the damage model for the cases listed in Table 10 and results can be found in Appendix D.

Figure 27: Summary of configuration of laterals

Configuration	Sample Photograph	Key features
P2	 <p data-bbox="402 1024 613 1052">SoCalGas 2017b</p>	Lateral extends to the top of the wellhead tree, changes direction and then runs along pipe supports
P3	 <p data-bbox="402 1365 613 1392">SoCalGas 2016b</p>	The lateral starts close to the top of the wellhead, runs vertically down and then runs along supports
P4		Pipe starts at the top of the tree, runs vertically down, then runs horizontally and runs vertically into the ground

3.4.3 Fragility Model for Wellheads to Ground Shaking

The probability of shaking induced failure on wellheads is given by Equation (3.9)(3.6) and is plotted in Figure 28. The model is based on the failure model for tensile rupture for below ground pipelines by Bain et al. (2022a).

$$Prob(\text{shaking induced wellhead failure}) = \Phi\left(\frac{\ln(\varepsilon) - \mu}{\sigma}\right) \quad (3.9)$$

Where:

ε is the longitudinal strain (in fraction) in the wellhead joint computed using the damage models in Appendix D;

$\mu = \bar{\mu} + \sigma_{epi}\xi$ is the mean fractional shear strain corresponding to 50% probability of failure;

$\bar{\mu} = \ln(4.68)$ is the median of the distribution of the mean where 50% probability of failure, the value of 4.68% is based on findings by Bain et al. (2022a);

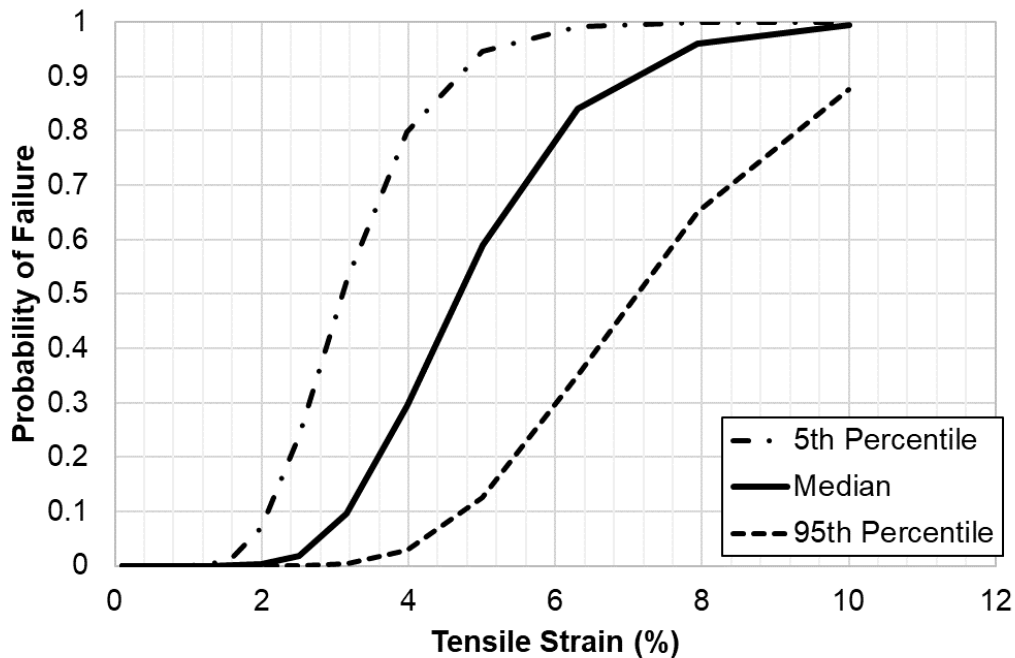
$\sigma = 0.3$ is the aleatory variability for μ ;

$\sigma_{epi} = 0.25$ is the epistemic uncertainty for $\bar{\mu}$;

Φ is the error function operator;

ξ is the standard normal random variable for the epistemic uncertainty;

Figure 28: Probability of Failure for Wellheads due to Ground Shaking



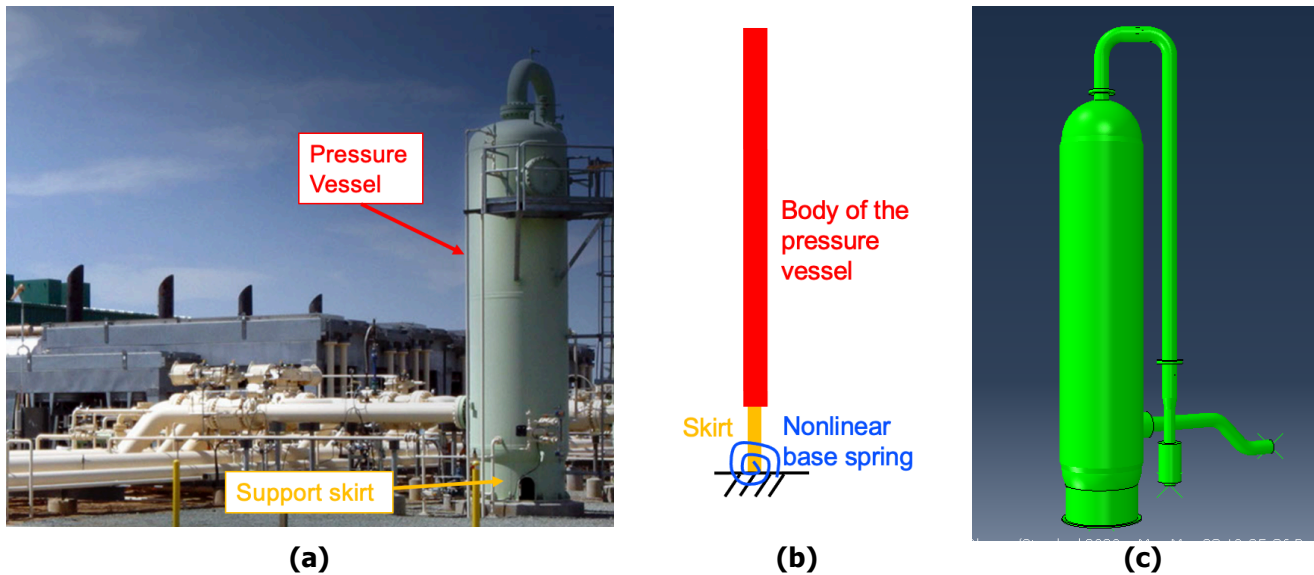
3.4.4 Damage Models for Storage Containers and Pressure Vessels to Ground Shaking

The vertical pressure vessels observed at gas storage facilities comprise a tall cylindrical vessel with hemispherical or elliptical heads supported by a skirt. The skirt is then connected to the concrete base with anchors. These vessels are connected to a pipe at their bottom right above the skirt, and to another pipe either going vertically upward on top of the vessel or laterally close to the head of the vessel (Figure 29a). Tall pressure vessels are particularly vulnerable to

seismic motions, with their behavior often dictated by the base condition and its ensuing flexibility. Hence, the critical component of this subsystem is deemed to be its base. The optimal EDP for these analyses is the ratio between the moment demand at the base imposed by an earthquake (M_d) and the moment capacity at which a limit state is achieved (M_c). For the VPV subsystem under consideration, when the base connection is fixed, the M_c is the moment associated with concrete breakout of the anchorage, as this will occur at an early load stage. Alternatively, when the base connection is designed with anchors that are intended to stretch, the moment associated with expected limit states is evaluated to identify the controlling minimum. For example, the strain beyond yield in the anchors will lead to plastic rotation of the top of the pressure vessel, which could limit functionality of attached piping, particularly for piping attached at the top of the VPV. Pressure vessels were modeled in OpenSees (Mazzoni et al., 2006) as cantilever beams. The areas and moments of inertia assigned to the beam varied, for the lower most portions properties were defined based on the skirt at the base, while the cylindrical portion of the pressure vessel extended for the remainder of the height (Figure 29b). In a first phase of analysis, the inlet and outlet pipes were also modeled. However, the model revealed that the presence of these pipes has very little influence on the dynamic characteristics of the subsystem, and hence these pipes were removed in subsequent phases of the analysis.

Validation of the OpenSees model was performed by comparing the natural frequencies and modes predicted with those predicted using a high-fidelity 3D Abaqus model for a sample VPV subsystem with the pipes connected to it (Figure 29c).

Figure 29: Vertical pressure vessels modeled in OpenSees and Abaqus



(a) Photograph (RockPoint Gas Storage, 2021), (b) Schematic of the OpenSees Model, (c) Abaqus model

3.4.5 Fragility Models for Storage Containers and Pressure Vessels to Ground Shaking

The probability of ground shaking induced failure on storage containers and pressure vessels is given by Equation (3.10) and is plotted in Figure 30. The median moment ratio at which 50% probability of failure occurs is estimated by the Task D researchers.

$$Prob(\text{shaking induced vessel failure}) = \Phi\left(\frac{M_r - \mu}{\sigma}\right) \quad (3.10)$$

Where:

M_r is the moment ratio for pressure vessels computed using the damage models in Appendix D;

$\mu = \bar{\mu} + \sigma_{epi}\xi$ is the mean fractional shear strain corresponding to 50% probability of failure;

$\bar{\mu} = 1$ is the median of the distribution of the mean where 50% probability of failure;

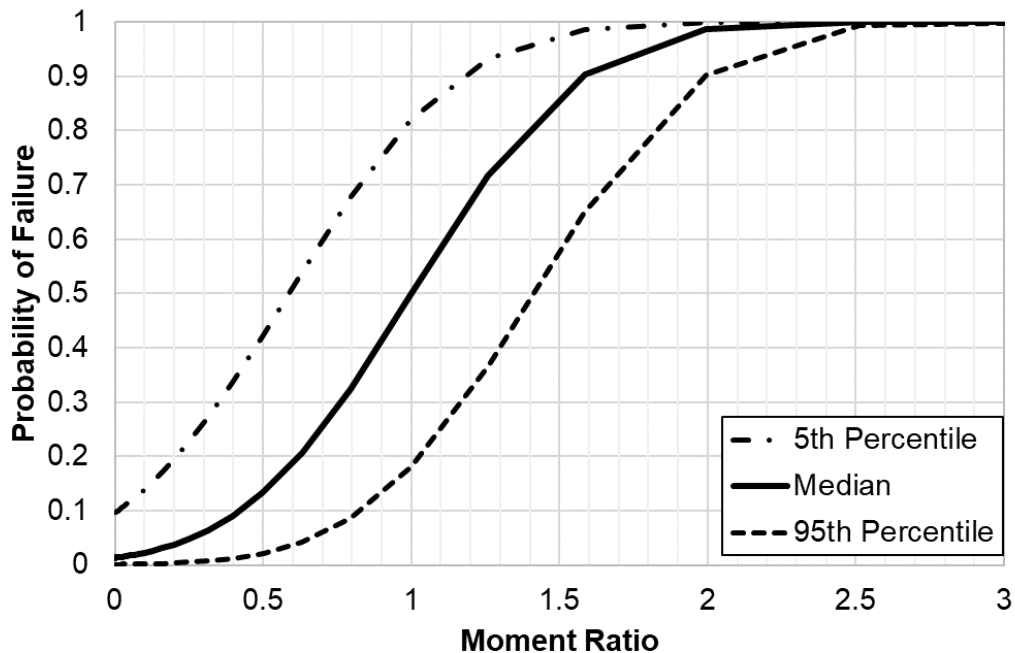
$\sigma = 0.45$ is the aleatory variability for μ ;

$\sigma_{epi} = 0.25$ is the epistemic uncertainty for $\bar{\mu}$;

Φ is the error function operator;

ξ is the standard normal random variable for the epistemic uncertainty;

Figure 30: Probability of Failure for Pressure Vessels due to Ground Shaking



CHAPTER 4:

Conclusions/Recommendations

This report presents the damage models and fragility models, collectively referred to as fragility curves, that were developed based on the finite element modeling of the research task groups. These fragility curves are for below ground pipelines, wells, caprocks and above ground infrastructure under seismic loading due to ground shaking, fault displacement, liquefaction, lateral spreading and landsliding.

The fragility curves presented within this report are developed based on up-to-date information given by utility companies and supplemented with additional laboratory testing or finite element modeling. This addition of laboratory testing and finite element modeling is unique to this project, and makes these fragility curves the most prevalent models to date. With this, multiple representatives from the utility owners aided in the development of the fragility curves, by giving the research team feedback from prior experience and input on the needs of the industry. As with any data set or model, there are limitations. These are listed within the report, and mainly stem from assumptions made in the analysis process. These assumptions are likely based on minimal data (from past earthquakes) and current information on how infrastructure was constructed and the material it was constructed from. As the industry continues to gather more information, the goal of *OpenSRA* is to continue to decrease the amount of limitations, and grow with the industry. As, *OpenSRA* is an open-source software the fragility equations will be open to the public and can be easily updated and changed within the program.

4.1 Implementation in *OpenSRA*

Fragility curves are the direct link between research on infrastructure response to earthquake loading, and calculations within *OpenSRA*. Each section of this report outlines the process and results of the effort to develop fragility curves based on the finite element modeling performed by each of the research task teams. The fragility curves have been implemented into *OpenSRA* and will be validated and demonstrated in upcoming reports (Validation Report and *OpenSRA* report).

4.2 Recommendations for Further Research

This research effort has developed a user friendly, open-source risk software for natural gas. Infrastructure experiencing seismic loading. Given the timeframe of the project, and the lack of existing fragility curves currently available, this project focused on typical infrastructure to be most broadly applicable. Several additional infrastructure types and/or unique configurations would benefit from additional research to develop fragility curves for those cases:

1. Bridge crossings
2. Impact of welds on pipelines

The risk framework implemented into *OpenSRA* is compatible with system types other than natural gas infrastructure, and demands outside of seismicity in California. Additional research would greatly expand the users of *OpenSRA* beyond natural gas providers in California:

1. Seismic demands in the U.S.A.
2. Electrical systems
3. Water distribution systems
4. Dams and levees.

It is the hope of the authors to continue to expand the use of *OpenSRA* through additional research projects in years to come.

GLOSSARY AND LIST OF ACRONYMS

Term	Definition
Abaqus	Finite Element Software
ALA	American Lifelines Alliance
ASCE	American Society of Civil Engineers
CDF	Cumulative Distribution Function
CEC	California Energy Commission
CoV	Coefficient of Variation
DM	Damage Measure
DV	Decision Variable
EDP	Engineering Demand Parameter
FD	Fault Displacement
IM	Intensity Measure
MAOP	Maximum Allowable Operating Pressure
OP	Operating Pressure
<i>OpenSRA</i>	Open Seismic Risk Assessment Tool
PBEE	Performance-Based Earthquake Engineering
PDF	Probability Density Function
PEER	Pacific Earthquake Engineering Research
PGA	Peak Ground Acceleration

Term	Definition
PGD	Permanent Ground Deformation
PRCI	Pipeline Research Council International
SMYS	Specified Minimum Yield Stress
SRSS	Square Root of the Sum of the Squares
α	Soil-Pipeline Adhesion Factor
β	Pipeline-Ground Deformation Zone Interaction Angle (i.e., Crossing Angle)
β_p	Pipe Burial Parameter Defined as Shear Force per Unit Length of Pipeline Divided by the Cross-Section Area of the Pipe
Δ_o	Ground Deformation a Pipe Ultimate Stress
D_a	Diameter of anchor
D_v	Pressure Vessel Diameter
Δ_f	Permanent Ground Deformation
Δ_o	Ground Deformation a Pipe Ultimate Stress
Δ_u	Ground Deformation a Pipe Ultimate Stress Conditioned by Anchorage Length (L_a)
δ	Friction Factor for Peak Cohesionless Soil and Rough Steel Pipe
E_{rock}	Young's Modulus of Rock
ε_{comp}	Longitudinal Compressive Strain
ε_{long}	Longitudinal Pipe Strain
ε_p	Longitudinal Pipe Strain
ε_{p-eq}	Zero Internal Pressure Equivalent Compressive Pipe Strain
ε_{ult}	Pipe Strain at the Ultimate Tensile Stress
γ	Soil Effective Unit Weight
γ_{casing}	Shear Strain on Casing
γ_{tubing}	Shear Strain on Tubing
H_c	Soil Cover
H_t	Entire Height of the Well Tree
H_v	Pressure Vessel Height
h	Height of Wellhead
k	Soil-Pipeline Interface Friction Factor

Term	Definition
L_2	Length of Pipe Segment 2 for Subsystem Types 2 and 3
L_6	Length of Pipe Segment 6 for Subsystem Types 2 and 3
L_p	Length of Pipe Segment 6 for Subsystem Type 4
M	Maximum Moment on Wells
M_p	Plastic Moment
M_r	Pressure Vessel Moment Ratio
m	Mass Per Unit Length of the Height of the Wellhead
μ	Mean
p	Pressure Vessel Design Pressure
Φ	Error Function
ϕ	Friction Angle of Sandy Soil
ϕ_{cmt}	Internal Friction Angle of Cement
Ψ	Polynomial Basis Functions
ψ	Soil-Pipeline Dip Angle
q_{VD}	Soil Bearing Resistance
Rot	Wellhead Component Rotation
s_u	Undrained Shear Strength
σ	Standard Deviation and Aleatory Variability
σ_{epi}	Epistemic Uncertainty
σ_h	Pipe Hoop Stress
σ_μ	Epistemic Uncertainty
σ_{ult}	Pipe Ultimate Stress
σ_y	Pipe Yield Stress
t	Pipe Wall Thickness
t_{ult}	Soil-Pipeline Interface Frictional Resistance
t_v	Pressure Vessel Skirt Thickness
θ	Fault-Well Intersection Angle
UCS_{cmt}	Uniaxial Compressive Strength of Cement
W_{dz}	Damage Zone Width

Term	Definition
W_{fc}	Fault Core Width
W_v	Valve Weight

REFERENCES

- Abrahamson, N. (2022). Personal Communication.
- ACI-318 (2019). Building Code Requirements for Structural Concrete and Commentary. American Concrete Institute, doi: 10.14359/51716937.
- ALA (2001). Guidelines for the Design of Buried Steel Pipe. American Lifelines Alliance. Retrieved March 16, 2022, from <https://www.americanlifelinesalliance.com/pdf/Update061305.pdf>
- ASCE (1984). Guidelines for the Seismic Design of Oil and Gas Pipeline Systems. Committee on Gas and Liquid Fuel Lifelines, American Society of Civil Engineers.
- Bain, Chris; Hutabarat, Daniel; Bray, Jonathan D.; Abrahamson, Norman; O'Rourke, Thomas D.; Lindvall, Scott. (2022a). *Performance-Based Earthquake Engineering Assessment Tool for Natural Gas Storage and Pipeline Systems, Task B - Enhanced Liquefaction and Ground Deformation Report*. California Energy Commission.
- Bain, Chris, O'Rourke, Thomas, Bray, Jonathan, Lindvall, Scott, Hutabarat, Daniel. (2022b). *Performance-Based Earthquake Engineering Assessment Tool for Natural Gas Storage and Pipeline Systems, Validation Report*. Pacific Earthquake Engineering Research (PEER) Center Report, in preparation.
- Harris, L. A., Suer, H. S., Skene, W. T., & Benjamin, R. J. (1957). The Stability of Thin-Walled Unstiffened Circular Cylinders Under Axial Compression Including the Effects of Internal Pressure. *Journal of the Aeronautical Sciences*, 24(8), 587–596. <https://doi.org/10.2514/8.3911>
- Honegger, D. G., & Nyman, D. J. (2004). Guidelines for the Seismic Design and Assessment of Natural Gas and Liquid Hydrocarbon Pipelines. Pipelines Research Council International
- Hutabarat, D., O'Rourke, T.D., Bray, J.D., Bain, C., Lindvall, S. (2022). *Performance-Based Earthquake Engineering Assessment Tool for Natural Gas Storage and Pipeline Systems, Task B - Underground Pipeline Fragilities*. Pacific Earthquake Engineering Research (PEER) Center Report, in preparation.
- Itasca Consulting Group (2020). FLAC3D — Fast Lagrangian Analysis of Continua in Three-Dimensions, Ver. 7.0. <https://www.itascacg.com/software/FLAC3D>.
- Jung, J. K., O'Rourke, T. D., & Argyrou, C. (2016). Multi-Directional Force–Displacement Response of Underground Pipe in Sand. *Canadian Geotechnical Journal*, 53(11), 1763–1781. <https://doi.org/10.1139/cgj-2016-0059>
- Lacour, M., and Abrahamson, N. A. (2021) Efficient Risk Calculation for Performance-Based Earthquake Engineering Distributed Systems. Pacific Earthquake Engineering Research (PEER) Center Report.

- Mazzoni S., McKenna F., Scott M. H., and Fenves G. L. (2006). OpenSees command language manual. Pacific Earthquake Engineering Research (PEER) Center, 264, 137-158.
- Moehle, J.P., and Deierlein, G.G., 2004, A framework methodology for performance-based earthquake engineering, Proc., 13th World Conf. on Earthquake Engineering, Vancouver, BC, Canada, Paper No. 679.
- Mohr, W. (2003). Strain-Based Design of Pipelines. Edison Welding Institute. Retrieved March 16, 2022, from <https://www.bsee.gov/sites/bsee.gov/files/tap-technical-assessment-program/434aa.pdf>
- O'Rourke, M. J., & Liu, J. X. (2012). Seismic Design of Buried and Offshore Pipelines. Monograph MCEER-12-MN04, Multidisciplinary Center for Earthquake Engineering Research, Buffalo, NY.
- O'Rourke, T. D., Jeon, S.-S., Toprak, S., Cubrinovski, M., Hughes, M., van Ballegooy, S., & Bouziou, D. (2014). Earthquake Response of Underground Pipeline Networks in Christchurch, NZ. *Earthquake Spectra*, 30(1), 183–204. <https://doi.org/10.1193/030413eqs062m>
- O'Rourke, T. D., Jung, J. K., & Argyrou, C. (2016). Underground Pipeline Response to Earthquake-Induced Ground Deformation. *Soil Dynamics and Earthquake Engineering*, 91, 272–283. <https://doi.org/10.1016/j.soildyn.2016.09.008>.
- Pantoli, E., Hutchinson, T.C., Elfass, S.A., and McCallen, D.B. (2022). Performance-Based Earthquake Engineering Assessment Tool for Natural Gas Storage and Pipeline Systems, Task D Final Report - Seismic Response of Pipeline and Gas Storage Surface Infrastructure. California Energy Commission.
- Rockpoint Gas Storage. Lodi. Retrieved March 2021, from <https://www.rockpointgs.com/Businesses/Lodi>
- Rutqvist, Jonny; Tsubasa Sasaki; Keurfon Luu; Preston Jordan; Yingqi Zhang; William Foxall, Jennie Watson-Lamprey, Micaela Largent, Barry Zheng, (2022). Performance-Based Earthquake Engineering Assessment Tool for Natural Gas Storage and Pipeline Systems, Task C Final Report - Seismic Response of Wells and Caprocks. California Energy Commission.
- Sasaki, T., Jordan, P., Foxall, W., & Rutqvist J. (2022). Fragility of Wells due to Fault Shearing—The Impact of Fault Displacement on the Integrity of Natural Gas Storage Wells in California. A Report for the "Performance-based Earthquake Engineering Assessment Tool for Natural Gas Storage and Pipeline Systems" Project. PEER Report 2022/##, Pacific Earthquake Engineering Research Center, University of California, Berkeley, CA.
- Thompson, Stephen. 2021. *Fault Displacement Hazard Characterization for OpenSRA*. California Energy Commission.

- Vamvatsikos D, 2014, Seismic performance uncertainty estimation via IDA with progressive accelerogram-wise Latin Hypercube Sampling, *J. Struct. Eng, ASCE*, vol. 140, no. 8, pp. 1–10.
- Watson-Lamprey, Jennie, Bao Li Zheng, Micaela Largent, Norman Abrahamson, Chris Bain, Jonathan Bray, with Jens Birkholzer, Sherif Elfass, William Foxall, Sanjay Govinjee, Peter Hubbard, Tara Hutchinson, Grace Kang, Amarnath Kasalanati, Maxime Lacour, Scott Lindvall, David McCallen, Frank McKenna, Thomas O'Rourke, Elide Pantoli, Floriana Petrone, Jonny Rutqvist, Matt Schoettler, Kenichi Soga, Steve Thompson and Jeff Unruh. 2020. *Sensitivity Report for the Performance-Based Earthquake Engineering Assessment Tool for Natural Gas Storage and Pipeline systems*. California Energy Commission. Publication Number: CEC-500-202X-XXX.
- Wijewickreme, D., Honegger, D., Mitchell, A., & Fitzell, T. (2005). Seismic Vulnerability Assessment and Retrofit of a Major Natural Gas Pipeline System: A Case History. *Earthquake Spectra*, 21(2), 539–567. <https://doi.org/10.1193/1.1898273>.

APPENDIX A:

Failure Mechanism Logic for Buried Pipelines

Three angles describe the problem geometry, and three-dimensional figures showing both the angles and ground movement, Δf , are provided for each type of pipeline-ground deformation crossing. For example, on page 3 the angles and Δf are shown for a pipeline subjected to left lateral strike-slip movement. The three angles are defined as follows:

β – *pipeline obliquity angle* ($0^\circ < \beta < 180^\circ$) is the smallest horizontal angle measured between the orientation of the longitudinal pipeline axis and the strike-slip component of motion on the failure plane. If the failure plane is pure dip-slip, β is the smallest horizontal angle measured between the orientation of the longitudinal pipeline axis and the strike of the failure plane according to the right-hand rule. The orientation of the pipeline is determined by vectorizing the pipeline to be pointing towards the hanging wall side of the fault (i.e., within 90 degrees or less of the dip direction azimuth). Failure planes may be faults or the edges of landslides, lateral spreads, or areas of liquefaction-induced ground settlement.

θ – *rake angle* ($-180^\circ \leq \theta \leq 180^\circ$) is measured on the failure plane, and is the angle measured from the failure plane's strike azimuth to the hanging wall displacement direction (relative to a fixed footwall). End member rake values are as follows: 0° defines pure left-lateral movement, 90° indicates pure reverse-slip movement, $\pm 180^\circ$ indicates pure right-lateral movement, and -90° indicates pure normal-slip movement. Angles between these end members represent a combination of lateral- and dip-slip movement. For example, -135° is right-lateral-normal displacement and 45° is left-lateral-reverse displacement.

ψ – *dip angle* ($0^\circ < \psi \leq 90^\circ$) is the vertical angle (within the range of 0° to 90°) from the horizontal plane to the ground deformation plane measured perpendicular to its strike.

The Logic Tree for *OpenSRA* is defined as follows for pipelines intersecting faults (Section 1), landslides (Section 2), lateral spreads (Section 3), and areas with liquefaction-induced settlement (Section 4).

Section 1: Logic Tree for Pipelines Crossing Faults

At fault crossings, the preferred values of β , Ψ , and θ are derived from information in the Third Uniform California Earthquake Rupture Forecast (UCERF3) model. Specifically, the UCERF3 model prescribes fault-subsection-average values for θ , Ψ , and the azimuth of the down-dip direction (dip direction azimuth) of the fault plane. The strike of the fault plane needed to calculate β can be derived by adding or subtracting 90° to or from the dip direction azimuth.

All three angles are defined by the Uniform California Earthquake Rupture Forecast (UCERF) model (currently Version 3) at fault crossings, but the assessment can be simplified for cases that are predominantly strike-slip, normal-slip, or reverse-slip. This is common in practice (e.g., the Hayward fault has a small vertical component of deformation but is often assessed assuming pure strike-slip deformation). We propose to simplify assessments at fault crossings as follows:

- $$\text{if } \begin{cases} \frac{\text{strike-slip deformation}}{\text{dip-slip deformation}} > 4 \rightarrow \text{Analyze as pure strike - slip} \\ \frac{\text{dip-slip deformation}}{\text{strike-slip deformation}} > 4 \rightarrow \text{Analyze as pure dip - slip} \end{cases}$$
- *else* \rightarrow Use full offset method patch (currently) to assess oblique movements

The limiting ratio values of > 4 noted above translate to rake angles that are more than 14° from the end-member values of 0° and 180° (for strike-slip faulting) or -90° and 90° (for normal and reverse dip-slip faulting, respectively). The analysis method and corresponding rake angle ranges are listed in Table 11:

Table 11: Range of Rake Angles for Analysis Method

Analysis method	Range of Rake Angle (degrees)
Pure Strike-Slip	-14 to 14 (Pure Left-Lateral); $\theta \leq -166$ or $\theta \geq 166$ (Pure Right-Lateral)
Pure Dip-Slip	-104 to -76 (Pure Normal); 76 to 104 (Pure Reverse)
Oblique (Full-Offset Method)	All Other Rakes

The cases outlined here apply at Levels 1, 2, and 3.

Case 1: Left Lateral Strike-Slip Fault Displacement

Parameter Range for Case 1:

$$0^\circ < \beta < 180^\circ$$

$$-14^\circ \leq \theta \leq 14^\circ$$

$$0^\circ < \psi \leq 90^\circ$$

Pipe Strain Assessment Model to Use Based on β :

IF $0^\circ < \beta \leq 90^\circ$: Hutabarat et al. Strike-Slip Tension Model with Parameters:

$$\beta = \beta$$

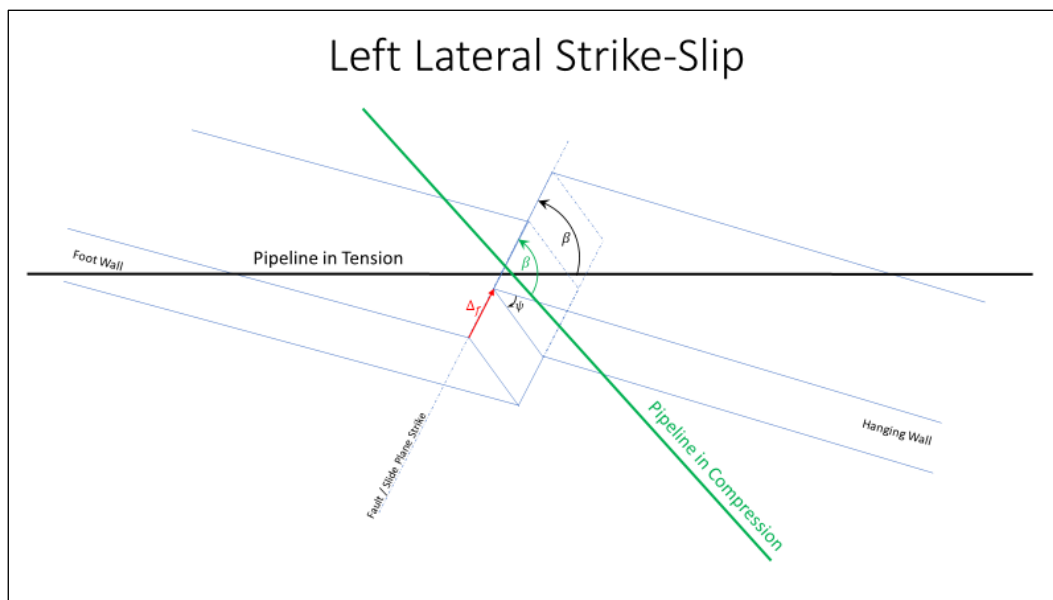
$$\Delta_f = \Delta_f |\cos(\theta)|$$

IF $90^\circ < \beta < 180^\circ$: Hutabarat et al. Strike-Slip Compression Model with Parameters:

$$\beta = \beta$$

$$\Delta_f = \Delta_f |\cos(\theta)|$$

Figure 31: Left Lateral Strike-Slip Fault Displacement Geometry



Case 2: Oblique Normal with Left Lateral Strike-Slip

Parameter Range for Case 2:

$$0^\circ < \beta < 180^\circ$$

$$-76^\circ < \theta < 14^\circ$$

$$0^\circ < \psi \leq 90^\circ$$

Pipe Strain Assessment Model to Use Based on β :

IF $0 < \beta \leq 90^\circ$: Full-Offset Method with Hutabarat et al. Strike-Slip Tension and Normal-Slip Models with Parameters:

$$\beta = \beta \text{ for Strike – Slip Tension Model}$$

$$\Delta_f = \Delta_f \text{ for Strike – Slip Tension Model}$$

$$\psi = \psi \text{ for Normal – Slip Model}$$

$$\Delta_f = \Delta_f \left(\frac{1}{|\cos(90-\beta)|} \right) \text{ for Normal – Slip Model}$$

IF $90^\circ < \beta < 180^\circ$: Worst Case Scenario Between Hutabarat et al. Strike-Slip Compression and Normal-Slip Models (Likely to be Strike-Slip Compression Model) with Parameters:

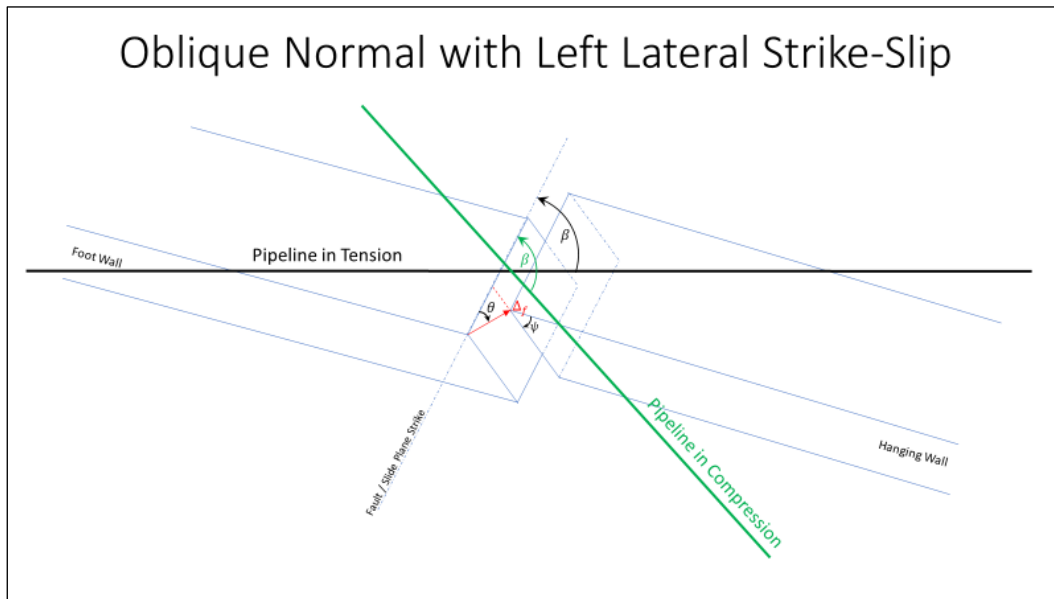
$$\beta = \beta \text{ for Strike – Slip Compression Model}$$

$$\Delta_f = \Delta_f \text{ for Strike – Slip Compression Model}$$

$$\psi = \psi \text{ for Normal – Slip Model}$$

$$\Delta_f = \Delta_f \left(\frac{1}{|\cos(90-\beta)|} \right) \text{ for Normal – Slip Model}$$

Figure 32: Oblique Normal with Left Lateral Strike-Slip Geometry



Case 3: Normal-Slip

Parameter Range for Case 3:

$$0^\circ < \beta < 180^\circ$$

$$-104^\circ \leq \theta \leq -76^\circ$$

$$0^\circ < \psi \leq 90^\circ$$

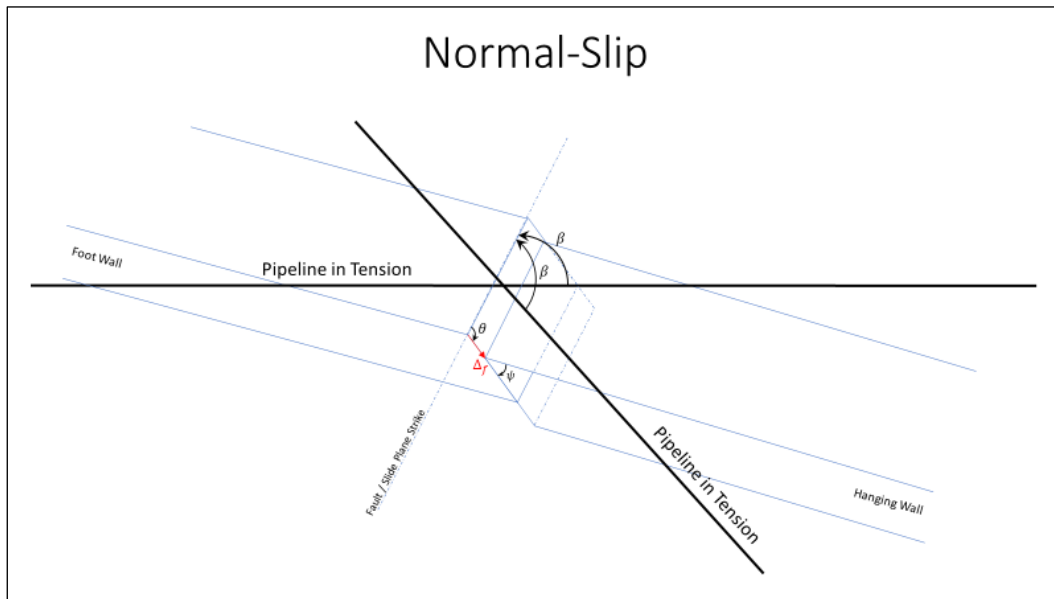
Pipe Strain Assessment Model to Use Based on θ :

Hutabarat et al. Normal-Slip Model with Parameters:

$$\Delta_f = \Delta_f * \left(\frac{1}{|\cos(90-\beta)|} \right) \text{ for Normal - Slip Model}$$

$$\psi = \psi \text{ for Normal - Slip Model}$$

Figure 33: Normal-Slip Geometry



Case 4: Oblique Normal with Right Lateral Strike-Slip

Parameter Range for Case 4:

$$0^\circ < \beta < 180^\circ$$

$$-166^\circ < \theta < -104^\circ$$

$$0^\circ < \psi \leq 90^\circ$$

Pipe Strain Assessment Model to Use Based on β :

IF $0 < \beta \leq 90^\circ$: Full-Offset Method with Hutabarat et al. Strike-Slip Tension and Normal-Slip Models with Parameters:

$$\beta = \beta \text{ for Strike – Slip Tension Model}$$

$$\Delta_f = \Delta_f \text{ for Strike – Slip Tension Model}$$

$$\psi = \psi \text{ for Normal – Slip Model}$$

$$\Delta_f = \Delta_f * \left(\frac{1}{|\cos(90-\beta)|} \right) \text{ for Normal – Slip Model}$$

IF $90^\circ < \beta < 180^\circ$: Worst Case Scenario Between Hutabarat et al. Strike-Slip Compression and Normal-Slip Models (Likely to be Strike-Slip Compression) with Parameters:

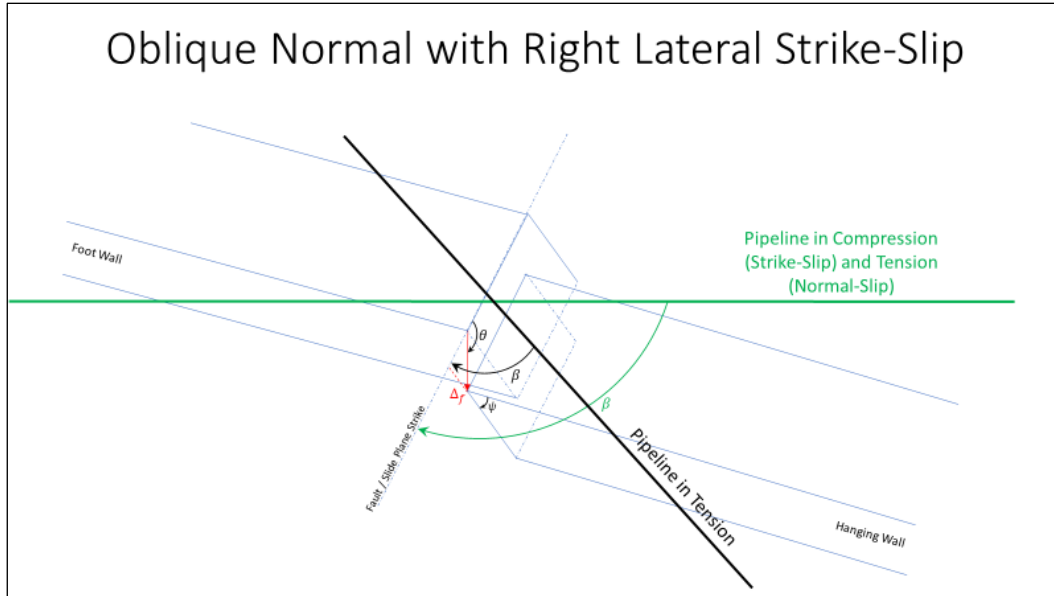
$$\beta = \beta \text{ for Strike – Slip Compression Model}$$

$$\Delta_f = \Delta_f \text{ for Strike – Slip Compression Model}$$

$\psi = \psi$ for Normal – Slip Model

$$\Delta_f = \Delta_f * \left(\frac{1}{|\cos(90-\beta)|} \right) \text{ for Normal – Slip Model}$$

Figure 34: Oblique Normal with Right Lateral Strike-Slip Geometry



Case 5: Right Lateral Strike-Slip

Parameter Range for Case 5:

$$0^\circ < \beta < 180^\circ$$

$$166^\circ \leq \theta \leq -166^\circ$$

$$0^\circ < \psi \leq 90^\circ$$

Pipe Strain Assessment Model to Use Based on β:

IF $0 < \beta \leq 90^\circ$: Hutabarat et al. Strike-Slip Tension Model with Parameters:

$$\beta = \beta$$

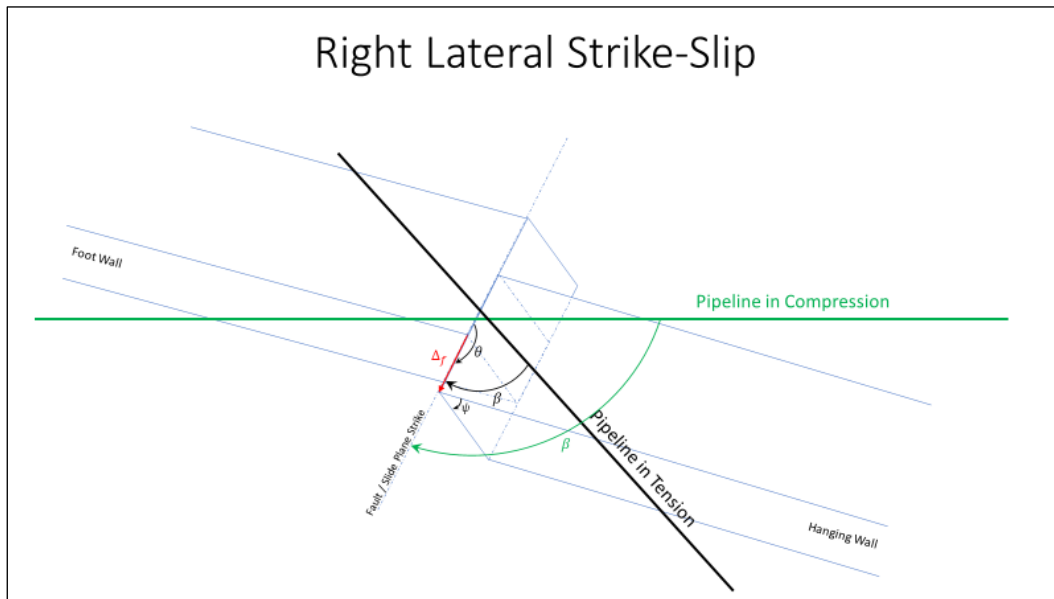
$$\Delta_f = \Delta_f$$

IF $90^\circ < \beta < 180^\circ$: Hutabarat et al. Strike-Slip Compression Model with Parameters:

$$\beta = \beta$$

$$\Delta_f = \Delta_f$$

Figure 35: Right Lateral Strike-Slip Geometry



Case 6: Oblique Reverse with Left Lateral Strike-Slip

Parameter Range for Case 6:

$$0^\circ < \beta < 180^\circ$$

$$14^\circ < \theta < 76^\circ$$

$$0^\circ < \psi \leq 90^\circ$$

Pipe Strain Assessment Model to Use Based on θ :

IF $0 < \beta \leq 90^\circ$: Use Worst Case Scenario Between Hutabarat et al. Strike-Slip Tension and Reverse-Slip Models (Likely to be Reverse-Slip Model) with Parameters:

$$\beta = \beta \text{ for Strike - Slip Tension Model}$$

$$\Delta_f = \Delta_f \text{ for Strike - Slip Tension Model}$$

$$\psi = \psi \text{ for Reverse - Slip Model}$$

$$\Delta_f = \Delta_f * \left(\frac{1}{|\cos(90-\beta)|} \right) \text{ for Reverse - Slip Model}$$

IF $90^\circ < \beta < 180^\circ$: Full-Offset Method with Hutabarat et al. Strike-Slip Compression and Reverse-Slip Models with Parameters:

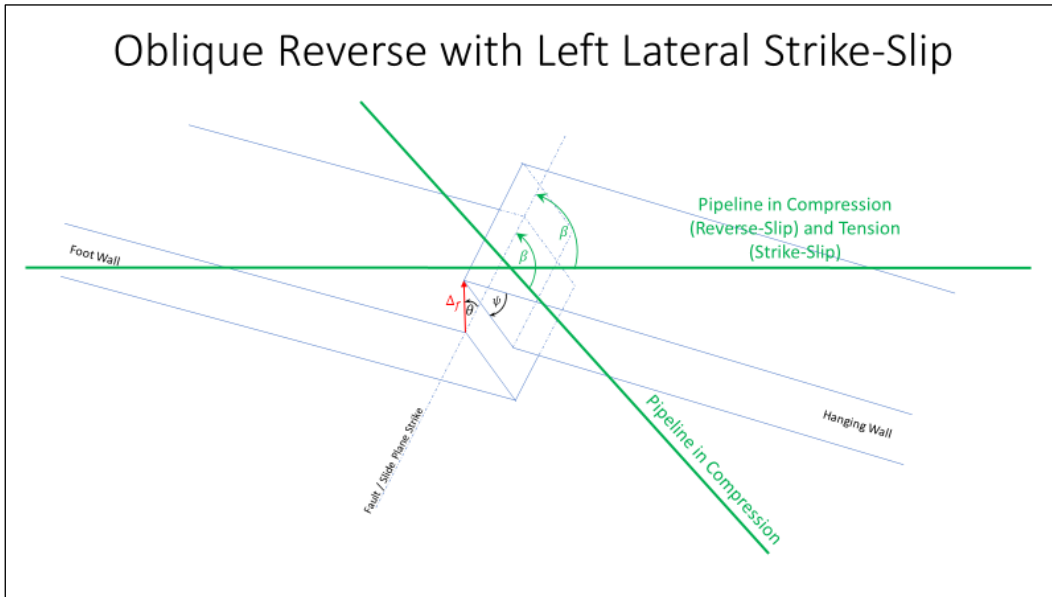
$$\beta = \beta \text{ for Strike - Slip Compression Model}$$

$$\Delta_f = \Delta_f \text{ for Strike - Slip Compression Model}$$

$$\psi = \psi \text{ for Reverse - Slip Model}$$

$$\Delta_f = \Delta_f * \left(\frac{1}{|\cos(90-\beta)|} \right) \text{ for Reverse - Slip Model}$$

Figure 36: Oblique Reverse with Left Lateral Strike-Slip Geometry



Case 7: Reverse-Slip

Parameter Range for Case 7:

$$0^\circ < \beta < 180^\circ$$

$$76^\circ \leq \theta \leq 104^\circ$$

$$0^\circ < \psi \leq 90^\circ$$

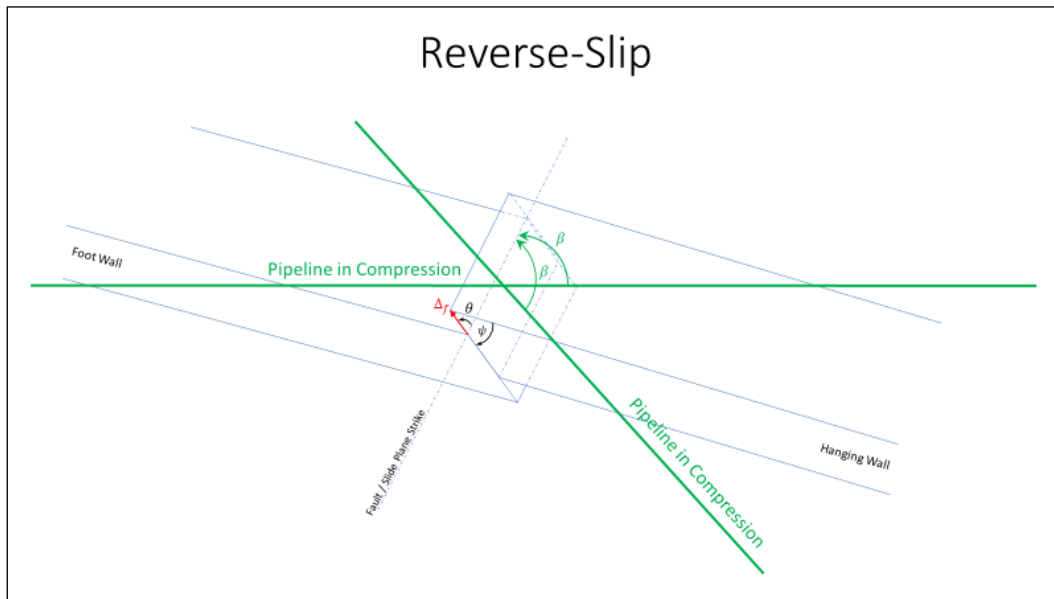
Pipe Strain Assessment Model to Use Based on θ :

Hutabarat et al. Reverse-Slip Model with Parameters:

$$\psi = \psi \text{ for Reverse - Slip Model}$$

$$\Delta_f = \Delta_f * \left(\frac{1}{|\cos(90-\beta)|} \right) \text{ for Reverse - Slip Model}$$

Figure 37: Reverse-Slip Geometry



Case 8: Oblique Reverse with Right Lateral Strike-Slip

Parameter Range for Case 8:

$$0^\circ < \beta < 180^\circ$$

$$104^\circ < \theta < 166^\circ$$

$$0^\circ < \psi \leq 90^\circ$$

Pipe Strain Assessment Model to Use Based on β :

IF $0 < \beta \leq 90^\circ$: Worst Case Scenario Between Hutabarat et al. Strike-Slip Tension and Reverse-Slip Models (Likely to be Reverse-Slip Model) with Parameters:

$$\beta = \beta \text{ for Strike - Slip Tension Model}$$

$$\Delta_f = \Delta_f \text{ for Strike - Slip Tension Model}$$

$$\psi = \psi \text{ for Reverse - Slip Model}$$

$$\Delta_f = \Delta_f * \left(\frac{1}{|\cos(90-\beta)|} \right) \text{ for Reverse - Slip Model}$$

IF $90^\circ < \beta < 180^\circ$: Full-Offset Method with Hutabarat et al. Strike-Slip Compression and Reverse-Slip Models with Parameters:

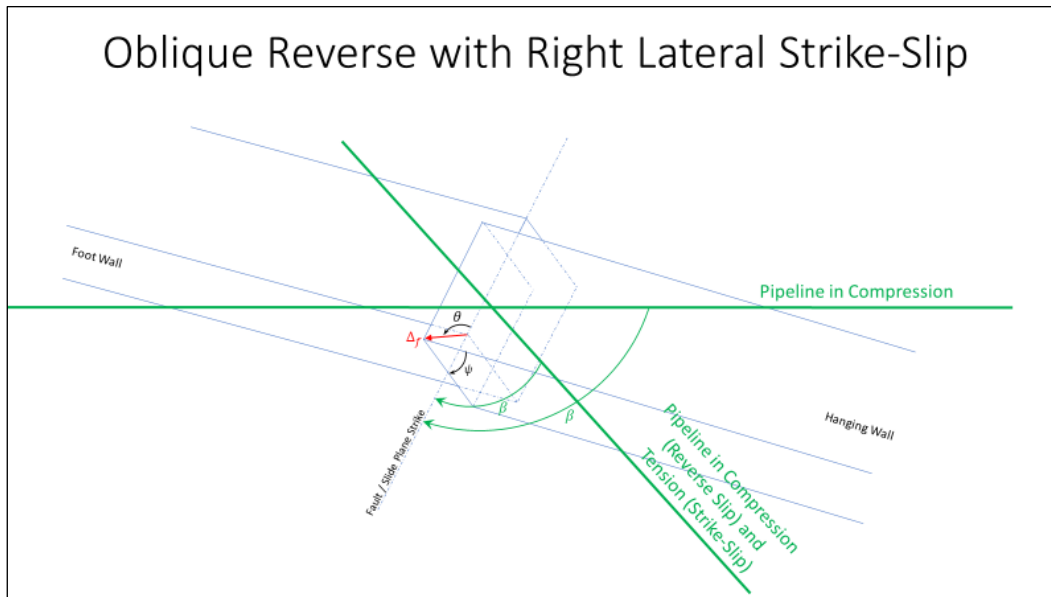
$$\beta = \beta \text{ for Strike - Slip Compression Model}$$

$$\Delta_f = \Delta_f \text{ for Strike - Slip Compression Model}$$

$$\psi = \psi \text{ for Reverse - Slip Model}$$

$$\Delta_f = \Delta_f * \left(\frac{1}{|\cos(90-\beta)|} \right) \text{ for Reverse - Slip Model}$$

Figure 38: Oblique Reverse with Right Lateral Strike-Slip Geometry



Section 2: Logic Tree for Pipelines Crossing Landslides

To assess risk from earthquake-induced slope displacement, *OpenSRA* will first discretize the pipelines into approximately 100-m long segments. At the midpoint of each segment, each of the parameters necessary to perform the seismic slope displacement assessment are sampled from their respective distributions to get a sense of the epistemic uncertainty. For each combination of parameters, the seismic slope displacement is calculated and if the estimated displacement is less than or equal to 5 cm, the displacement is assumed to be negligible (i.e., zero), and the probability of leakage or rupture is assumed to be zero. For non-negligible seismic slope displacement (greater than 5 cm), the probability of tensile leakage or rupture or compressive rupture is estimated. Finally, *OpenSRA* reports the risk as the percentiles (i.e., 5th, 16th, 50th, 84th, and 95th) for the probability of tensile leakage or rupture and the probability of compressive rupture at each pipe segment.

At Level 1, no landslide polygons are available at the statewide level. Rather, the ground displacement hazard is evaluated assuming infinite slope type failures with distributions of geotechnical strength parameters correlated to the units in the statewide Wills et al. (2015) geologic map and slope based on a statewide slope map with approximately 30 m resolution. The steps for assessing risk from seismic slope displacement at Level 1 are outlined below:

1. If the estimated seismic slope displacement for a combination of the input parameters is less than or equal to 5 cm, assume no (i.e., negligible) displacement of the landslide. The probability of tensile leakage or rupture and the probability of compressive rupture is therefore zero for this combination of parameters.
2. If non-negligible seismic slope displacement (greater than 5 cm) is calculated for a combination of the input parameters, assume a pipeline in this zone has a 25% chance of crossing the edge of a landslide. This is applied by multiplying the resulting probability of leakage or rupture by 0.25.
3. At Level 1, there is insufficient information without polygons to check if a pipeline crosses the scarp or toe of a landslide; therefore, assume pipeline/landslide interaction can be assessed as strike-slip ground deformation. Assess the pipeline using the Hutabarat et al. strike-slip compression model.

At Level 2, the landslide polygons from the CGS landslide inventory are used unless the user inputs an alternative set of landslide polygons. A Level 2 assessment does not have site-specific geotechnical strength data. The analysis steps at Level 2 are as follows:

1. First, check location of pipeline crossings in an area defined as a landslide using the polygons from the CGS landslide inventory, or as an alternative, a set of user-defined landslide polygons. The length of the landslide is defined by the length of a line from the highest point of the landslide feature (i.e., scarp) to the

lowest point of the landslide feature (i.e., toe). This vector from the scarp to the toe of the landslide is also assumed to define the direction of the landslide movement. If the pipeline crosses in the upper 15% of the line that defines the landslide length, assume it crosses the scarp. If it crosses in the bottom 15% of the line that defines the landslide length, assume it crosses the toe. If it crosses the middle 70%, assume it crosses the body of the landslide. *OpenSRA* will determine the locations of pipeline/landslide intersections and perform the assessment at those locations.

2. Second, check the pipeline crossing angle relative to the direction of the landslide movement. Refer to Figure 39 and Figure 40 follow which illustrate the cases described in this step.
 - If the pipeline crosses within $\pm 20^\circ$ of the orientation of the line that defines the length of the landslide, assume pure normal-slip at the scarp and pure reverse-slip at the toe.
 - If the pipeline crosses within $20^\circ - 45^\circ$ of the orientation of the line that defines the length of the landslide, assume the pipeline is in a transition zone between pure normal-slip and pure strike-slip at the upper part of the landslide with a linear weighting factor or it is in a transition zone between pure reverse-slip and pure strike-slip at the lower part of the landslide with a linear weighting factor.
 - If the pipeline crosses at an angle greater than 45° from the orientation of the line that defines the length of the landslide AND it crosses the landslide body, assume pure strike-slip displacement.
 - If it crosses at an angle greater than 45° from the orientation of the line that defines the length of the landslide AND it crosses the landslide scarp area, assume pure normal-slip displacement.
 - If it crosses at an angle greater than 45° from the orientation of the line that defines the length of the landslide AND it crosses the landslide toe area, assume pure reverse-slip displacement.
3. For pure normal-slip, assume $\theta = -90^\circ$ and a mean value of $\Psi = 65^\circ$. Lower and upper limits of Ψ are $\Psi = 45^\circ$ and $\Psi = 90^\circ$. For pure reverse-slip, assume $\theta = 90^\circ$ and a mean value of $\Psi = 35^\circ$. Lower and upper limits of Ψ are $\Psi = 25^\circ$ and $\Psi = 50^\circ$.
4. In the transition zones, assume mean value of $\Psi = 65^\circ$ and $\theta = -90^\circ$ for pure normal-slip, a mean value of $\Psi = 35^\circ$ and $\theta = 90^\circ$ for pure reverse-slip, and $\theta = 0^\circ$ or $\theta = 180^\circ$ (pure left or right lateral movement, respectively) for strike-slip. *OpenSRA* will determine if the pipeline will be in the strike-slip compression or tension mode based on the β angle and relative motion (left lateral or right lateral) of the landslide and the stable, non-moving ground.

At Level 3, the user should input landslide polygons; the CGS landslide inventory landslide polygons are used as a default if the user chooses not to input landslide polygons. The analysis steps at Level 3 are as follows:

1. First, check the location of pipeline crossings in an area defined as a landslide using the user input landslide polygons, or if not provided, using the CGS landslide inventory landslide polygons as a default. The user-defined landslide polygons must include an attribute indicating the slip direction azimuth. The length of the landslide is defined by the length of a line from the highest point of the landslide feature (i.e., scarp) to the lowest point of the landslide feature (i.e., toe) by sampling from a DEM map. If the pipeline crosses in the upper 15% of the line that defines the landslide length, assume it crosses the scarp. If it crosses in the bottom 15% of the line that defines the landslide length, assume it crosses the toe. If it crosses the middle 70%, assume it crosses the body of the landslide.
2. Second, check the pipeline crossing angle relative to the direction of the landslide movement. Refer to Figure 39 and Figure 40 which illustrate the cases described in this step. These five assumptions are the same as used in Level 2 analyses.
 - If the pipeline crosses within $\pm 20^\circ$ of the orientation of the landslide slip direction vector, assume pure normal-slip at the scarp and pure reverse-slip at the toe.
 - If the pipeline crosses within $20^\circ - 45^\circ$ of the orientation of the landslide slip direction vector, assume the pipeline is in a transition zone between pure normal-slip and pure strike-slip at the upper part of the landslide with a linear weighting factor or it is in a transition zone between pure reverse-slip and pure strike-slip at the lower part of the landslide with a linear weighting factor.
 - If the pipeline crosses at an angle greater than 45° from the orientation of the landslide slip direction vector AND it crosses the landslide body, assume pure strike-slip displacement.
 - If it crosses at an angle greater than 45° from the orientation of the landslide slip direction vector AND it crosses the landslide scarp area, assume pure normal-slip displacement.
 - If it crosses at an angle greater than 45° from the orientation of the line landslide slip direction vector AND it crosses the landslide toe area, assume pure reverse-slip displacement.
3. For pure normal-slip, assume $\theta = -90^\circ$ and a mean value of $\Psi = 65^\circ$. Lower and upper limits of Ψ are $\Psi = 45^\circ$ and $\Psi = 90^\circ$. For pure reverse-slip, assume $\theta = 90^\circ$ and a mean value of $\Psi = 35^\circ$. Lower and upper limits of Ψ are $\Psi = 25^\circ$ and $\Psi = 50^\circ$.

4. In the transition zones, assume mean value of $\Psi = 65^\circ$ and $\theta = -90^\circ$ for pure normal-slip, a mean value of $\Psi = 35^\circ$ and $\theta = 90^\circ$ for pure reverse-slip, and $\theta = 0^\circ$ or $\theta = 180^\circ$ (pure left or right lateral movement, respectively) for strike-slip. *OpenSRA* will determine if the pipeline will be in strike-slip compression or tension mode based on the β angle.

Figure 39: Landslide Crossing – Level 2 and 3 – Location Logic

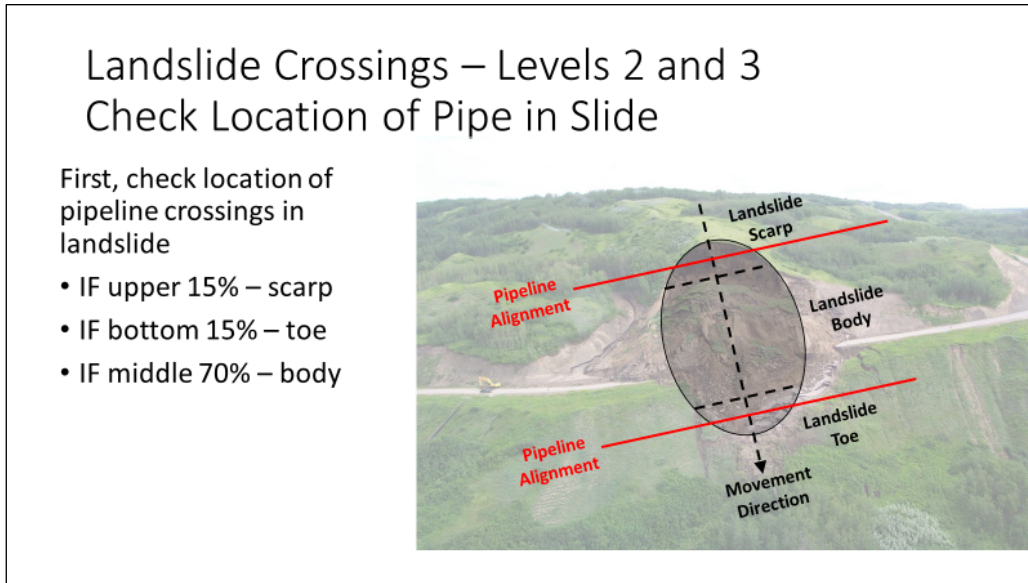
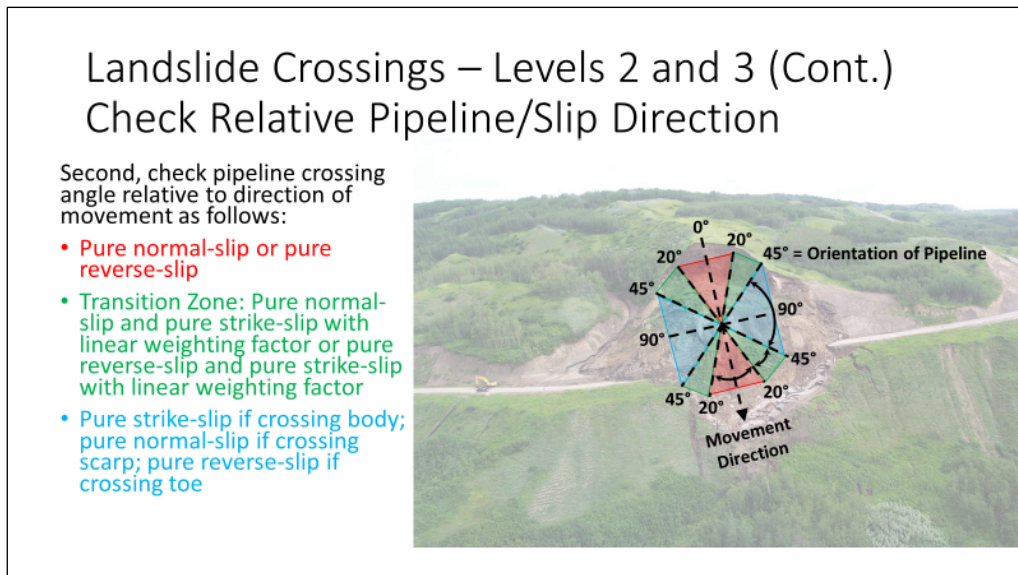


Figure 40: Landslide Crossing – Level 2 and 3 – Angle Logic



Section 3: Logic Tree for Pipelines Crossing Lateral Spreads

To assess risk from liquefaction-induced lateral spreading, *OpenSRA* will first discretize the pipelines into approximately 100-m long segments. At the midpoint of each segment, each of the parameters necessary to perform the lateral spread displacement assessment are sampled from their respective distributions to get a sense of the epistemic uncertainty. For each combination of parameters, the lateral spread displacement (D_H) is calculated and if the estimated displacement is less than or equal to 5 cm, the displacement is assumed to be negligible (i.e., zero), and the probability of leakage or rupture is assumed to be zero. For non-negligible lateral spread displacement (greater than 5 cm), the probability of tensile leakage or rupture or compressive rupture is estimated. Finally, *OpenSRA* reports the risk as the percentiles (i.e., 5th, 16th, 50th, 84th, and 95th) for the probability of tensile leakage or rupture and the probability of compressive rupture at each pipe segment.

Lateral spreading can be differentiating into two cases: lateral spreads influenced by a free-face condition and lateral spreading influenced by a gently sloping ground condition. The free-face ratio (L/H) is used to estimate the displacement for lateral spreads near a free-face condition and is defined as the distance from a point in question to the bottom of the free-face (L) divided by the height of the free-face (H). Topographic slope (%) is used to estimate the displacement for lateral spreads on gently sloping ground.

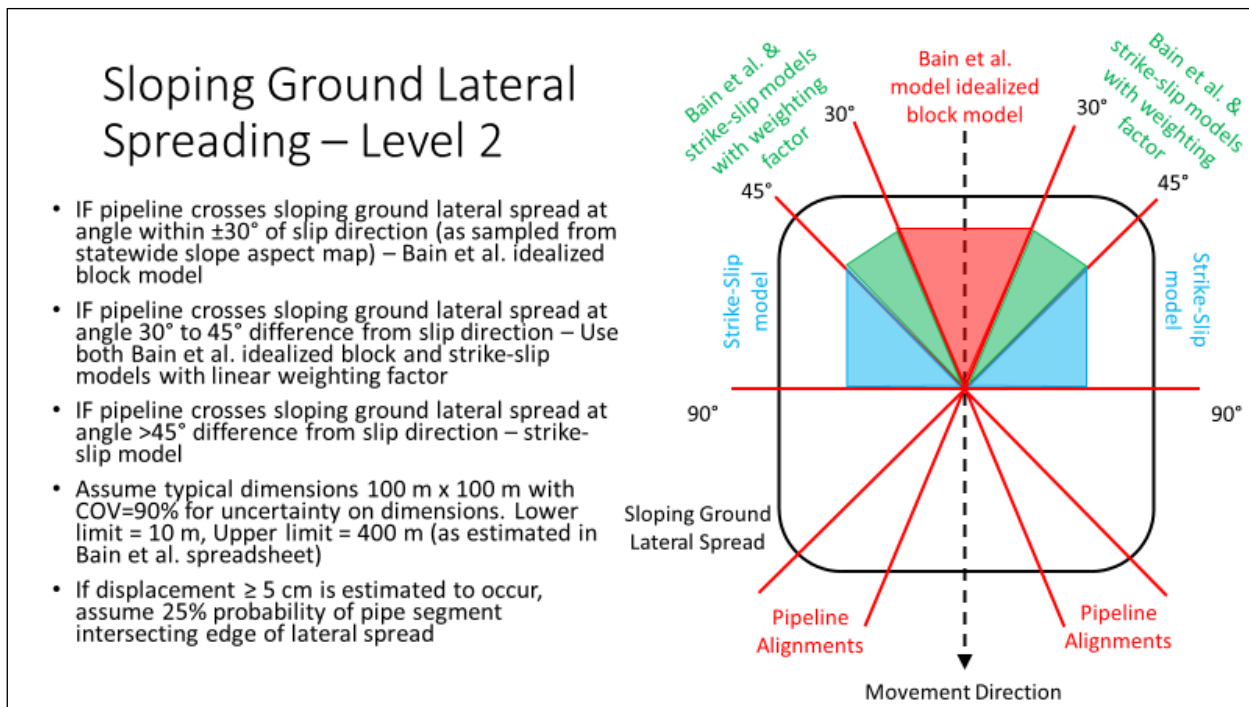
At Level 1, we do not differentiate between the free face condition and the gently sloping ground condition. At Level 1, if the estimated lateral spread displacement is less than or equal to 5 cm, the displacement is negligible and the probability of tensile leakage or rupture or compressive rupture is zero. For non-negligible displacement (displacement greater than 5 cm), assume that a pipeline has a 25% probability of crossing the edge of a lateral spread. This is applied by multiplying the resulting probability of leakage or rupture by 0.25. Use the Bain et al. idealized block model to estimate pipe strain, assume the estimated pipe strain is in compression.

At Level 2, regardless of which Level 2 method is used to estimate lateral spread displacement, we assume geometry for a generic lateral spread. As at Level 1, if the displacement is negligible (less than or equal to 5 cm), the displacement is assumed to be zero. For non-negligible displacement (displacement greater than 5 cm), assume that a pipeline has a 25% probability of crossing the edge of a lateral spread. This is applied by multiplying the resulting probability of leakage or rupture by 0.25. Next, check the pipeline crossing angle relative to the direction of the lateral spread displacement movement. Refer to Figure 41, which illustrate the cases described in this step.

- If the pipeline crosses within $\pm 30^\circ$ of the orientation of the lateral spread slip direction vector, assess the pipe strain using the Bain et al. model. Assume the strain is compressive.
- If the pipeline crosses within $30^\circ - 45^\circ$ of the orientation of the lateral spread slip direction vector, assume the pipeline is in a transition zone between the Bain et al. model and the Hutabarat et al. strike-slip with a linear weighting factor. Assume the pipe strain is compressive.

- If the pipeline crosses at an angle greater than 45° from the orientation of the lateral spread, assess the pipe strain with the Hutabarat et al. strike-slip model. Assume the pipe strain is compressive.
- The lateral spread slip direction is estimated by sampling a statewide slope aspect map.

Figure 41: Lateral Spreading – Level 2 – Angle of Crossing Logic



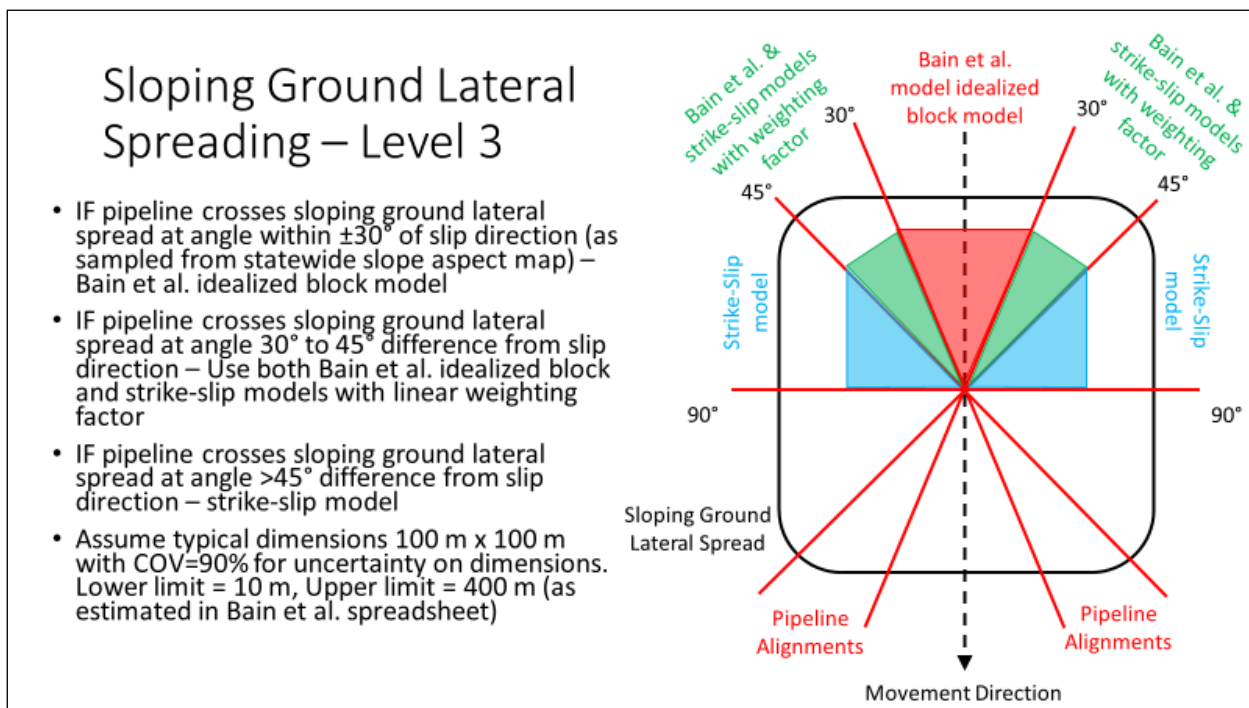
At Level 3, the liquefaction triggering and lateral spread displacement assessment is performed using CPTs, or soil exploratory borings if CPTs are not available. A Level 3 assessment cannot be performed without site-specific data from a CPT or a soil boring. *OpenSRA* takes the CPTs or soil borings data and estimates a lateral spread polygon rather than assuming generic dimensions for a lateral spread. As at Levels 1 and 2, if the estimated displacement is negligible (less than or equal to 5 cm), assume that the displacement is zero.

At Level 3, *OpenSRA* determines whether the free-face condition or gently sloping ground condition controls. To do this, for gently sloping ground lateral spreads, *OpenSRA* will sample an approximately 30 m resolution slope map to estimate the topographic slope at the site in question and calculate the lateral spread displacement. If near a free-face condition, the user should input a shapefile (line feature) indicating the location of the bottom of nearby free-face features and it must include an attribute indicating the height of the free-face feature. *OpenSRA* will then calculate the shortest distance to the free-face feature (L), calculate the free-face ratio (L/H) using the height attribute (H) in the user provided shapefile, and calculate the lateral spread displacement (D_H). The lateral spread displacement is taken as the maximum from the gently sloping ground and free-face conditions. If the user does not provide a shapefile indicating the location of the bottom of nearby free-face feature, *OpenSRA*

will assume the gently sloping ground condition controls. If the gently sloping ground condition controls, the pipe strain is calculated as follows (and shown in Figure 42):

- If the pipeline crosses within $\pm 30^\circ$ of the orientation of the lateral spread slip direction vector, assess the pipe strain using the Bain et al. model. Assume the strain is tensile on the upslope side of the lateral spread and compressive on the downslope side.
- If the pipeline crosses within $30^\circ - 45^\circ$ of the orientation of the lateral spread slip direction vector, assume the pipeline is in a transition zone between the Bain et al. model and the Hutabarat et al. strike-slip models with a linear weighting factor. Assume the strain is tensile on the upslope side of the lateral spread and compressive on the downslope side.
- If the pipeline crosses at an angle greater than 45° from the orientation of the lateral spread slip direction vector, assess the pipe strain with the Hutabarat et al. strike-slip models. Assume the strain is tensile on the upslope side of the lateral spread and compressive on the downslope side.

Figure 42: Lateral Spreading – Level 3 – Angle of Crossing Logic



If the free-face condition controls, the logic for assessing pipe strain is as follows:

- If the pipeline crosses a free-face lateral spread, the free-face ratio (L/H) is less than or equal to 10, and the pipeline crosses within $\pm 30^\circ$ of the orientation of the lateral spread slip direction vector, estimate the pipe strain as the maximum value calculated from the Bain et al. model and the Hutabarat et al. pure normal-slip tension model with a mean value of dip angle, $\Psi = 45^\circ$ (assumes equal vertical and outward horizontal ground deformation). Assume the strain in both models is tensile because the lateral spread

extension zone typically produces the greatest displacement demand on a buried pipeline in a free-face lateral spread.

- If the pipeline crosses a free-face lateral spread, the free-face ratio (L/H) is less than or equal to 10, and the pipeline crosses at an angle within 30° - 45° of the orientation of the lateral spread slip direction vector, estimate the pipe strain as the maximum value calculated from the Bain et al. model and the Hutabarat et al. pure normal-slip tension model with a value of dip angle, $\Psi = 45^\circ$. Apply a linear weighting factor to the two models.
- If the pipeline crosses a free-face lateral spread, the free-face ratio (L/H) is less than or equal to 10, and the pipeline crosses at angle greater than 45° from the slip direction vector, estimate the pipe strain as the maximum value calculated from the Hutabarat et al. pure normal-slip tension model.
- If the pipeline crosses within $\pm 30^\circ$ of the orientation of the lateral spread slip direction vector and $L/H > 10$, assess the pipe strain using the Bain et al. model. Assume the strain is tensile, because the lateral spread extension zone typically produces the greatest displacement demand on a buried pipeline in a free-face lateral spread.
- If the pipeline crosses within 30° - 45° of the orientation of the lateral spread slip direction vector and $L/H > 10$, assume the pipeline is in a transition zone between the Bain et al. model and the Hutabarat et al. pure strike-slip model with a linear weighting factor. Assume the strain is tensile.
- If the pipeline crosses at an angle greater than 45° from the orientation of the lateral spread slip direction vector and $L/H > 10$, assess the pipe strain with the Hutabarat et al. pure strike-slip tension model. Assume the strain is tensile for a free-face lateral spread.

Section 4: Logic Tree for Pipelines Crossing Areas of Liquefaction-Induced Settlement

To assess risk from liquefaction-induced ground settlement, *OpenSRA* will first discretize the pipelines into approximately 100-m long segments. At the midpoint of each segment, each of the parameters necessary to perform the liquefaction-induced settlement assessment are sampled from their respective distributions to get a sense of the epistemic uncertainty. For each combination of parameters, the liquefaction-induced settlement is calculated and if the estimated settlement is less than or equal to 5 cm, the settlement is assumed to be negligible (i.e., zero), and the probability of leakage or rupture is assumed to be zero. For non-negligible liquefaction-induced settlement (greater than 5 cm), the probability of tensile leakage or rupture or compressive rupture is estimated. Finally, *OpenSRA* reports the risk as the percentiles (i.e., 5th, 16th, 50th, 84th, and 95th) for the probability of tensile leakage or rupture and the probability of compressive rupture at each pipe segment.

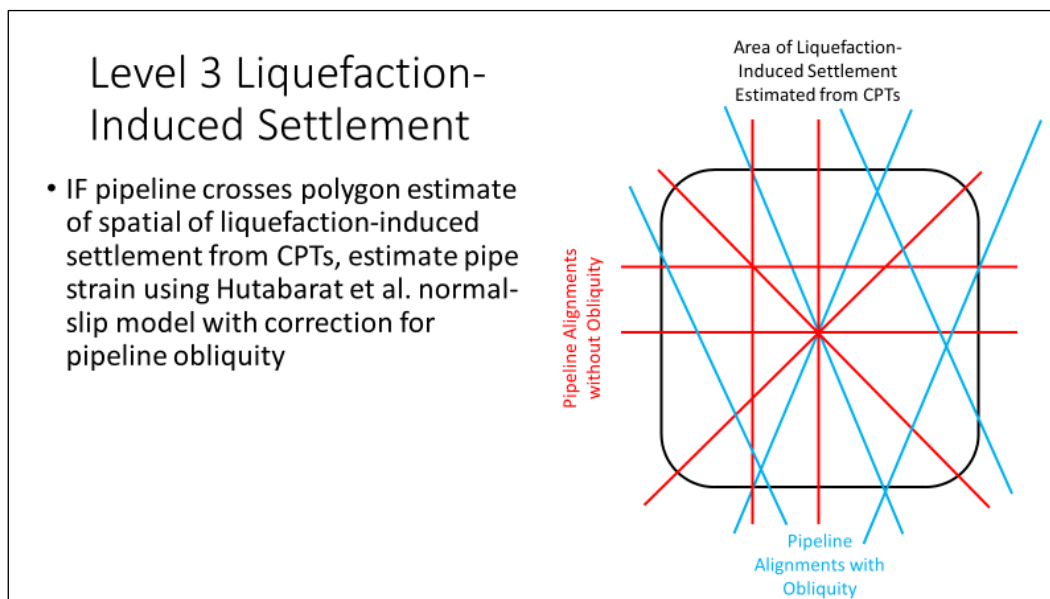
At Level 1, if the estimated liquefaction-induced settlement is less than or equal to 5 cm, the settlement is negligible, and the probability of rupture is zero. For non-negligible settlement (settlement greater than 5 cm), assume that a pipeline has a 25% probability of crossing the edge of an area with liquefaction-induced ground settlement. This is applied by multiplying the resulting probability of leakage or rupture by 0.25. Use the Hutabarat et al. pure normal-slip

(rake angle, $\theta = -90^\circ$) model to estimate pipe strain given the estimate of liquefaction-induced ground settlement, assuming the dip angle, $\Psi = 75^\circ$ and the pipeline obliquity, $\beta = 90^\circ$.

At Level 2, the quality of the data used to calculate liquefaction-induced settlement is improved (see data matrix) and the pipeline data are also improved. However, the logic tree for performing the liquefaction-induced ground settlement assessment is similar at Level 1 and Level 2. If the settlement is negligible (less than or equal to 5 cm), the settlement is assumed to be zero. For non-negligible settlement (greater than 5 cm), assume that a pipeline has a 25% probability of crossing the edge of an area with liquefaction-induced ground settlement. This is applied by multiplying the resulting probability of leakage or rupture by 0.25. Use the Hutabarat et al. pure normal-slip (rake angle, $\theta = -90^\circ$) model to estimate pipe strain given the estimate of liquefaction-induced ground settlement, assuming the dip angle, $\Psi = 75^\circ$ and the pipeline obliquity, $\beta = 90^\circ$.

At Level 3, the liquefaction triggering and ground settlement assessment is performed using CPT or soil boring data, which is a significant improvement in the quality of the geotechnical data relative to the data available at Levels 1 and 2. A Level 3 assessment cannot be performed without site-specific data from a CPT or a soil boring. *OpenSRA* takes the CPTs or soil borings data and creates a polygon to estimate the spatial extent of liquefaction-induced ground settlement. If the estimated settlement is negligible (less than or equal to 5 cm), assume that the ground settlement is zero, and the probability of leakage or rupture due to this hazard is zero. For non-negligible estimated liquefaction-induced ground settlement (greater than 5 cm), use the Hutabarat et al. pure normal-slip (rake angle, $\theta = -90^\circ$) model to estimate pipe strain for given the estimate of liquefaction-induced ground settlement, assuming a default dip angle, $\Psi = 75^\circ$, which can be overridden by a user-defined dip angle based on the geometry of the ground settlement area. *OpenSRA* will estimate the pipeline obliquity (β) based on the intersection angle of the pipeline with the edges of the ground settlement area (see Figure 43). If insufficient information is available for *OpenSRA* to estimate pipeline obliquity, β will be assumed to be equal to 90° .

Figure 43: Liquefaction-Induced Settlement – Level 3 – Analysis Logic



APPENDIX B: Damage Models of Below Ground Pipelines

Tensile and Compressive Strain Damage Models

Using the parameters listed in Table 12, more than one million numerical simulations of pipelines subjected to permanent ground deformation were performed. The simulation results are used to develop relationships that estimate a distribution of longitudinal pipe strain as a function of the soil-pipeline system parameters.

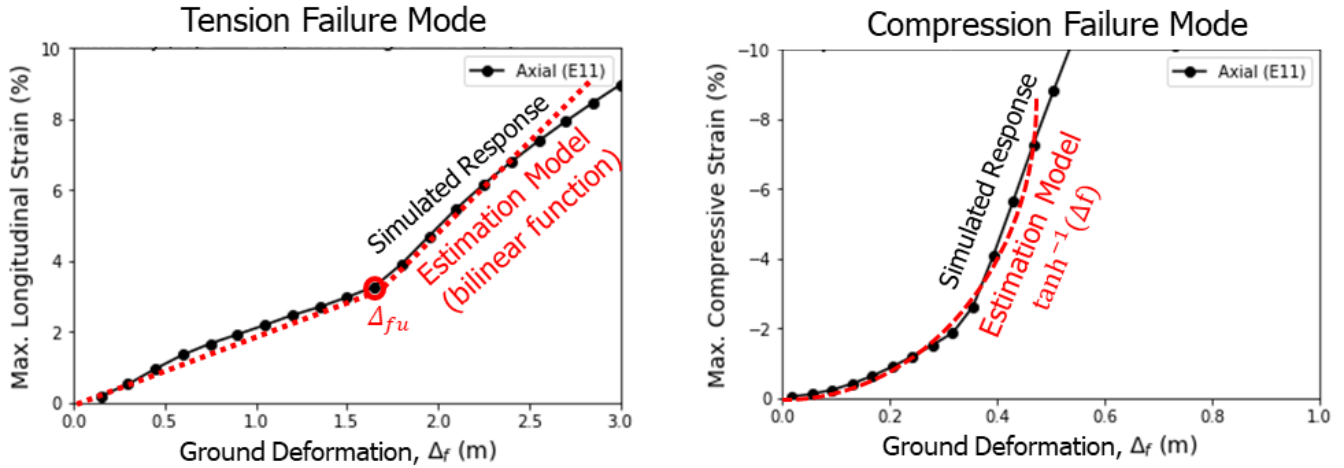
Table 12: Range of Parameters Used in Numerical Simulations

Parameter	Range
Outside Diameter (cm)	10.2, 20.3, 30.5, 40.6, 50.8, 61.0, 76.2, 86.4, 106.7
Wall Thickness (mm)	2 to 22 (realistically paired with pipe diameter)
Burial Depth (m)	0.3 to 4.5
Soil Friction Angle (°)	37 to 43
Undrained Shear Strength (kPa)	25 to 75
Strike-Slip Crossing Angle (°)	15, 45, 75, 90
Normal-Slip Dip Angle (°)	15, 45, 75, 90
Reverse-Slip Dip Angle (°)	15, 45, 75, 90
Pipe Material	Grade-A, Grade-B, X-42, X-52, X-60, X-70
Class Location	0, 1, 4
Sand Relative Density	Medium Dense to Very Dense
Clay Undrained Shear Strength	Soft to Stiff

The pipe strain estimation models have been developed to capture the strain response of pipelines responding to the modes of ground deformation illustrated Figure 10. The slope of pipe strain versus the ground deformation changes significantly at up to two locations for pipeline responding to tensile ground deformation (depending on the strike-slip crossing angle) and at one location for pipelines responding to compressive ground deformation.

Figure 44 presents numerical results in terms of the longitudinal strain for representative tensile and compressive failure mode cases. Pipe strain estimation models for the strike-slip tension and strike-slip compression ground deformation modes, which are based on the Abaqus finite element analyses, and the case with ground deformation parallel to the longitudinal axis of the pipeline, which is based on the results of an analytical model, are provided in this report to illustrate the form of these models. The complete suite of pipe strain estimation models for all cases are provided below. For oblique fault shearing, the logic for model selection is additionally conditioned on the slip direction.

Figure 44: Modeled Pipeline Response to Tensile and Compressive Pipe Strain



Modeled pipeline response to tensile pipe strain (strike-slip tension or normal-slip mode) and compressive pipe strain (strike-slip compression or reverse-slip mode) with examples of bi-linear and inverse hyperbolic tangent regression models used to capture the simulated responses.

Mode A: Pipe Strain Estimation Model for Strike-Slip Tension Ground Deformation

The model to estimate pipe strain for pipes subjected to strike-slip tension ground deformation with presented as Equations (B.11) through (B.14). This model is suitable for: (1) ground deformation interaction angle, β , is greater than 90 degrees and slip direction, θ , between 90 and 180 degrees relative to North for fault displacement; (2) β greater than 10 degrees and less than 90 degrees for landslide displacement; and (3) β greater than 10 degrees and less than 90 degrees for lateral-spread displacement.

$$t_{ult} = \begin{cases} \pi * D * \gamma * H * \tan(\delta * \phi) & - \text{Sand} \\ \pi * D * \alpha * s_u & - \text{Clay} \end{cases} \quad (B.11)$$

where:

- t_{ult} is the ultimate K_0 condition soil frictional resistance (kN/m);
- D is the outside pipe diameter (m);
- H is the burial depth to the pipe centerline (m);
- γ is the soil effective unit weight (kN/m³);
- δ is the friction factor for peak cohesionless soil and rough steel pipe (unitless);
- ϕ is the friction angle of sandy soil (°);
- α is the soil-pipeline adhesion factor (unitless);
- s_u is the undrained shear strength of clayey soil (kPa);

$$\ln(\Delta_o) = a_0 + a_1 \ln(D/t) + a_2 \ln(L_a) \quad (B.12)$$

where:

Δ_o is the estimated ground deformation at the pipe ultimate stress (m);

a_0, a_1, a_2 are model regression coefficients (see Table 13);

$$a_1 = c_3 t_{ult} + c_4 \ln(\varepsilon_{ult})$$

D/t is the pipe diameter-to-thickness ratio;

L_a is the pipeline anchorage length (m);

Table 13: Model Regression Coefficients to Estimate Δ_o

Coefficient	Value
a_0	-0.15507
a_2	0.05203
c_3	0.00081
c_4	0.00314

$$a_1 = c_3 t_{ult} + c_4 \ln(\varepsilon_{ult})$$

where:

c_3, c_4 are model regression coefficient given in Table 13;

ε_{ult} is the estimated pipe strain at the ultimate tensile stress estimated with the Ramberg-

Osgood model using $\varepsilon_{ult} = 100 \frac{\sigma_{ult}}{E} \left[1 + \frac{n}{1+r} \left(\frac{\sigma_{ult}}{\sigma_y} \right)^r \right]$ (%);

$E = 2 * 10^8$ kPa is the Young's Modulus of steel;

σ_y is the pipe steel yield stress (MPa);

n, r are the Ramberg-Osgood model parameters;

Recommended default values for ε_{ult} are provided in Table 14.

Table 14: Recommended Default ε_{ult} (%) Values Based on Steel Grade

Steel Grade	σ_y (MPa)	n	r	σ_{ult} (MPa)	ε_{ult} (%)
Grade-B	241	3	8	344	1.09
X-42	290	3	9	414	1.64
X-52	359	8	10	455	1.90
X-60	414	8	12	517	2.43
X-70	483	14	15	565	2.77
X-80	552	15	20	625	2.85

Once Δ_o is calculated with Equation (B.12), it has to be adjusted by the pipeline anchorage length (m) based on Equation (B.13):

$$\ln(\Delta_u) = \begin{cases} \ln(\Delta_o) + 0.75 & - \text{for } L_a < 15m \\ \ln(\Delta_o) + 1.0 & - \text{for } 15m \leq L_a \leq 50m \\ \ln(\Delta_o) + 0.75 & - \text{for } L_a > 50m \end{cases} \quad (\text{B.13})$$

Equation (B.14) is used to calculate the pipe longitudinal strain in tension.

$$\ln(\varepsilon_{long}) = b_0 + b_1 \ln(\Delta_f) + b_2 \ln\left(\frac{D}{t}\right) + F_{soil} b_3 \ln t_{ult} \pm \sigma_{\ln \varepsilon} \quad (\text{B.14})$$

where:

ε_{long} is the estimated pipe longitudinal (tensile) strain (%);

Δ_f is the input permanent ground deformation (m);

D/t is the pipe diameter-to-thickness ratio;

t_{ult} is the ultimate K_0 condition soil frictional resistance (kN/m) – see Equation (B.11);

b_0, b_1, b_2, b_3 are model regression coefficients given in Table 15;

$\sigma_{\ln \varepsilon}$ is the model standard deviation (natural log units) given in Table 15;

$\beta_u=0.3$ is the estimated model epistemic uncertainty;

$$F_{\Delta_o} = \begin{cases} 1, & \text{for } \Delta_f < \Delta_o; \\ 0, & \text{otherwise;} \end{cases}$$

$$F_{\Delta_u} = \begin{cases} 1, & \text{for } \Delta_f > \Delta_u; \\ 0, & \text{otherwise;} \end{cases}$$

$$F_{soil} = \begin{cases} 1, & \text{Sand} \\ 0, & \text{Clay} \end{cases}$$

$$b_1 = \left[F_{\Delta_o} \ln\left(\frac{\Delta_f}{\Delta_o}\right) \left(e_1 + e_2 t_{ult} + e_3 \left(\frac{D}{t}\right) \right) \right] + \left[F_{\Delta_u} \ln\left(\frac{\Delta_f}{\Delta_u}\right) \left(e_4 + e_5 t_{ult} + e_6 L_a + e_7 \left(\frac{D}{t}\right) + d_8 (\ln \varepsilon_{ult}) \right) \right]$$

where:

$e_1, e_2, e_3, e_4, e_5, e_6, e_7, e_8$ are model regression coefficients given in Table 15;

Table 15: Model Regression Coefficients to Estimate ε_{long}

Coefficient	Value
b_0	-2.307229
b_2	0.5852366
b_3	0.201322
e_1	1.4274935
e_2	-0.007105
e_3	0.0051416
e_4	-1.429059
e_5	0.0492003
e_6	0.145136
e_7	0.0201703
e_8	-1.032025
σ	0.723

Mode B: Pipe Strain Estimation Model for Strike-Slip Compression Ground Deformation

The model to estimate pipe strain for pipes subjected to strike-slip compression ground deformation is presented as Equation (B.15). This model is suitable: (1) for ground deformation interaction angle, β , less than or equal to 90 degrees and slip direction, θ , between -180 and -90 degrees relative to North for fault displacement; (2) β greater than or equal to 90 degrees and less than 170 degrees for landslide displacement; and (3) β greater than or equal to 90 degrees and less than 170 degrees for lateral-spread displacement.

$$\ln(\varepsilon_{comp}) = \frac{\tanh^{-1}\left(\frac{\ln \Delta_f - b_0}{b_1}\right)}{b_2} - 4 \pm \sigma_{\ln \varepsilon} \quad (\text{B.15})$$

where:

ε_{comp} is the pipe longitudinal compressive strain (%);

Δ_f is the input ground deformation (m);

$\sigma_{\ln \varepsilon} = 0.571$ is the standard deviation of the model (natural log units);

$\beta_u = 0.3$ is the estimated model epistemic uncertainty;

$b_0 = -6.50785 + 0.98692 D + 0.01601 L_a + (-0.04575 F_\beta)$;

$b_1 = 4.54097 - 0.01093 L_a$;

$b_2 = 0.34262 + (-0.10918 D) + 0.00197 L_a + 0.0027 F_\beta$;

$F_\beta = \begin{cases} 0, & \text{for } 120 < \beta < 175. \\ \beta - 120, & \text{for } 95 < \beta \leq 120' \end{cases}$

where:

D is the outside pipe diameter (m);

L_a is the pipeline anchorage length (m);

Mode C: Pipe Strain Estimation Model for Normal-Slip Ground Deformation

The model to estimate pipe strain for pipes subjected to normal-slip ground deformation is presented as Equations (B.16) to (B.18). There are three steps to the model, as explained below. This model is suitable for: (1) ground deformation interaction angle, β , less than or equal to 90 degrees and slip direction, θ , between -180 and -90 degrees relative to North for fault displacement; (2) β less than 10 degrees or greater than 170 degrees for landslide displacement at the head scarp; and (3) all angles for liquefaction-induced vertical settlement.

The first step is to calculate the soil frictional resistance, t_{ult} , and the soil bearing resistance, q_{VD} . Please refer to Equation (B.11) for t_{ult} . For q_{VD} , use Equation (B.16) below:

$$q_{VD} = \begin{cases} N_{qVD} \gamma H D + 0.5 \gamma D^2 N_{\gamma d} - \text{Sand} \\ 5.14 S_u D - \text{Clay} \end{cases} \quad (\text{B.16})$$

where:

γ is the soil effective unit weight (kN/m³);

D is the outside pipe diameter (m);

H is the burial depth to the pipe centerline (m);

s_u is the undrained shear strength of clayey soil (kPa);

$$N_{\gamma d} = \min(80, \exp(0.18\phi - 2.5));$$

ϕ is the friction angle of sandy soil ($^\circ$);

$$N_{qVD} = \begin{cases} 13.082 - 1.038\frac{H}{D} + 0.579\left(\frac{H}{D}\right)^2 - 0.072\left(\frac{H}{D}\right)^3 + 0.0027\left(\frac{H}{D}\right)^4; & \text{medium dense sand} \\ 17.168 - 1.571\frac{H}{D} + 0.585\left(\frac{H}{D}\right)^2 - 0.063\left(\frac{H}{D}\right)^3 + 0.0022\left(\frac{H}{D}\right)^4; & \text{dense sand} \\ 22.265 - 3.567\frac{H}{D} + 1.083\left(\frac{H}{D}\right)^2 - 0.103\left(\frac{H}{D}\right)^3 + 0.0032\left(\frac{H}{D}\right)^4; & \text{very dense sand} \end{cases}$$

Note that the H/D value must be greater than 1.8 and smaller than 11.5

The second step is to calculate the ground deformation when pipe reach its ultimate stress capacity, Δ_u , using Equation (B.17) below:

$$\ln \Delta_u = a_0 + a_1 \ln(L_a) + a_2 \ln D + a_3 \ln\left(\frac{D}{t}\right) + a_4 \ln \varepsilon_{ult} + a_5 \ln q_{VD} + a_6 \ln t_{ult} \quad (\text{B.17})$$

where:

Δ_u is the estimated ground deformation when pipe reach its ultimate stress capacity (m);

t is the pipe wall thickness (m);

$a_0, a_1, a_2, a_3, a_4, a_5$ are regression coefficients given in Table 16;

L_a is the pipeline anchored length (m);

ε_{ult} is the estimated pipe strain at the ultimate tensile stress estimated with the Ramberg-

Osgood model using $\varepsilon_{ult} = 100 \frac{\sigma_{ult}}{E} \left[1 + \frac{n}{1+r} \left(\frac{\sigma_{ult}}{\sigma_y} \right)^r \right]$ (%) – see Table 14 for default values;

$E = 2 * 10^8$ kPa is the Young's Modulus of steel;

σ_y is the pipe steel yield stress (MPa);

n, r are the Ramberg-Osgood model parameters;

Table 16: Regression Coefficient to estimate Δ_u

Coefficient	$\psi \leq 30^\circ$	$\psi = 45^\circ$	$\psi = 60^\circ$	$\psi = 75^\circ$	$\psi = 90^\circ$
a_0	3.9633	3.7533	4.3183	5.5951	14.5751
a_1	0.2937	0.1451	-0.0279	0.0160	0.1356
a_2	1.2438	1.2497	1.0497	1.2641	2.9990
a_3	-0.7020	-0.4610	-0.4691	-0.5243	-0.9471
a_4	-0.3957	0.3914	0.2915	0.3583	0.6603
a_5	-0.4051	-0.2131	-0.2861	-0.3592	-1.2489
a_6	0.0001	-0.3414	-0.1348	-0.2482	-0.4414

Note: For values of ψ not listed in the above table (e.g., $\psi = 55^\circ$), calculate $\ln \Delta_u$ for the upper and lower cases and propagate these values through Step 3, and then linearly interpolate between the upper and lower cases of natural log of the strain values.

The third step is to calculate the longitudinal pipe strain (tensile), ε_{long} , using Equation (B.18) below:

$$\ln \varepsilon_{long} = b_0 + b_1 \ln \left(\frac{\Delta_f}{\Delta_u} \right) + b_2 \ln \left(\frac{D}{t} \right) + [b_3 F_{soil} \ln t_{ult} + b_4 \ln q_{VD}] + b_5 \ln D \pm \sigma_{\ln \varepsilon} \quad (\text{B.18})$$

where:

ε_{long} is the pipe longitudinal (tensile) strain (%);

Δ_f is the input ground deformation (m);

D is the outside pipe diameter (m);

D/t is the pipe diameter-to-thickness ratio;

$b_0, b_1, b_2, b_3, b_4, b_5$ are regression coefficient given in Table 17;

$\sigma_{\ln \varepsilon}$ is the standard deviation of the model (natural log units) interpolated using Table 17;

$\beta_u=0.3$ is the estimated model epistemic uncertainty;

$$F_{\Delta_f} = \begin{cases} 1, & \text{for } \Delta_f < \Delta_u, \\ 0, & \text{otherwise} \end{cases}$$

$$F_{L_a} = \begin{cases} 1, & \text{for } L_a < 100m, \\ 0, & \text{otherwise} \end{cases}$$

$$F_{soil} = \begin{cases} 1, & \text{Sand} \\ 0, & \text{Clay} \end{cases}$$

$$b_1 = \left[F_{\Delta_f} \left(d_2 + d_3 t_{ult} + d_{41} F_{L_a} (L_a - 100) + d_{42} (1 - F_{L_a}) + d_5 \left(\frac{D}{t} \right) \right) \right] + \left[(1 - F_{\Delta_f}) (d_6 + d_{71} F_{L_a} (L_a - 100) + d_{72} (1 - F_{L_a}) + d_8 (\ln \varepsilon_{ult})) \right]$$

Table 17: Regression Coefficient to estimate ε_{long}

Coefficient	$\psi \leq 30^\circ$	$\psi = 45^\circ$	$\psi = 60^\circ$	$\psi = 75^\circ$	$\psi = 90^\circ$
b_0	0.8018	-1.1082	-2.1277	-2.3450	5.1354
b_2	0.0265	0.1063	0.1476	0.1947	-0.0496
b_3	0	-0.1439	-0.2183	-0.2044	0.4459
b_4	0.0180	0.2788	0.4227	0.4143	-0.8371
b_5	0.1417	-0.3103	-0.5372	-0.5571	0.6309
d_2	1.1363	1.2553	1.2520	1.0931	0.9139
d_3	0.0012	0.0003	-0.0006	0.0001	0.0025
d_{41}	0.0038	0.0052	0.0053	0.0035	0.0016
d_{42}	0	-0.0859	-0.0485	-0.0407	-0.0975
d_5	0.0032	0.0006	0.0013	0.0016	0.0012
d_6	2.1297	-0.2176	-0.5660	-0.6595	0.4648
d_{71}	0.0010	-0.0269	-0.0321	-0.0301	0.0008

d_{72}	0	0.5739	0.8497	0.8422	0.0679
d_8	-0.3867	0.3446	0.0901	0.5068	0.5898
$\sigma_{\ln \varepsilon}$	0.349	0.3997	0.5017	0.4378	0.3475

Mode D: Pipe Strain Estimation Model for Reverse-Slip Ground Deformation

The model to estimate pipe strain for pipes subjected to reverse-slip ground deformation is presented as Equation (B.19). This model is suitable for: (1) ground deformation interaction angle, β , less than or equal to 90 degrees and slip direction, θ , between -180 and -90 degrees relative to North for fault displacement; and (2) β less than 10 degrees or greater than 170 degrees for landslide displacement at the toe of the landmass.

$$\ln(\varepsilon_{comp}) = \frac{\tanh^{-1}\left(\frac{\ln \Delta_f - b_0}{b_1}\right)}{b_2} - b_3 + b_4 \pm \sigma \quad (\text{B.19})$$

where:

ε_{comp} is the pipe longitudinal compressive strain (%);

Δ_f is the input ground deformation (m);

σ is the standard deviation of the model (natural log units) based on a normal 2 mixture distribution model, with model parameters given in Table 18;

$\sigma_{epi}=0.3$ is the estimated model epistemic uncertainty;

$b_0 = -4.11127 + 0.60640 D + 0.002805 L_a + 0.038944 F_\psi$;

$b_1 = 2.29445 + (-0.04675 D) + (-0.00104) L_a + (-0.09201 F_\psi)$;

$b_2 = 0.42882 + 0.09845 D + 0.0006 L_a + 0.01203 F_\psi$;

$b_3 = 2.64335 + (-0.36353) D + 0.00086 L_a + (-0.05422 F_\psi)$;

$b_4 = -4.57877 - 0.04142 \left(\ln^2\left(\frac{D}{t}\right)\right) + 0.9346 \ln\left(\frac{D}{t}\right) + 0.4714 \ln(t_{ult}) + 0.00007 (180 - \psi) - 5.2467 F_D (D - 0.5) - 0.28986 (1 - F_D)$;

$$F_\psi = \begin{cases} 0, & \text{for } 15 < \psi \leq 60, \\ 60 - \psi, & \text{for } 60 < \psi \leq 90 \end{cases}$$

$$F_D = \begin{cases} 1, & \text{for } D < 0.5 \text{ cm}, \\ 0, & \text{for } D > 0.5 \text{ cm} \end{cases}$$

where:

D is the outside pipe diameter (m);

L_a is the pipeline anchorage length (m);

D/t is the pipe diameter-to-thickness ratio;

t_{ult} is the ultimate K_0 condition soil frictional resistance (kN/m) – see Equation (B.11);

ψ is the dip angle (degree);

Table 18: Model Regression Coefficients to Estimate $\sigma_{ln \epsilon}$

Coefficient	Value
μ_1	-0.283
μ_2	-0.625
σ_1	0.46
σ_2	0.709
π_1	0.688
π_2	0.312

Mode E: Pipe Strain Estimation Model for Ground Deformation Parallel to Pipeline Axis

Models were also developed to estimate pipe strain for the case of lateral spread permanent ground deformation parallel to the pipe where no bending strains are induced. Further explanation of this mode of ground deformation and of the fragility model development can be found in Bain et al. (2022b) and Hutabarat et al. (2022). For the case of pipelines buried in sand, Equation (B.20) is used to estimate an intermediate parameter called the embedment length, L_e , and for the case of pipelines buried in clay, Equation (B.21) is used to estimate the embedment length.

$$\ln(L_e) = 0.188 + 0.853 * \ln(t) - 0.018 * \ln(D) + 0.751 * \ln(\sigma_y) - 0.862 * \ln(H) - 0.863 * \ln(\gamma) - 1.005 * \ln(\phi) - \ln(\delta) + 0.136 * \ln(PGD) + \epsilon\sigma \quad (B.20)$$

$$\ln(L_e) = -4.019 + 0.876 * \ln(t) + 0.787 * \ln(\sigma_y) - 0.886 * \ln(s_u) - 0.889 * \ln(\alpha) + 0.114 * \ln(PGD) + \epsilon\sigma \quad (B.21)$$

where:

L_e is an intermediate parameter to estimate the pipe strain, termed the embedment length (m);

t is the pipe wall thickness (mm);

D is the pipe diameter (mm);

σ_y is the pipe steel yield stress (kPa);

H is the soil cover to the pipe centerline (m);

γ is the soil effective unit weight (kN/m³);

δ is the sand-pipeline interface friction angle ratio (sand-pipeline interface friction angle divided by sand friction angle);

ϕ is the sand friction angle (deg);

α is the clay-pipeline adhesion factor;

s_u is the undrained shear strength of clay (kPa);

ϵ is the number of standard deviations from the mean;

σ is the model standard deviation

From regression, Equations (B.20) and (B.21) have small aleatory variability of 0.06 and 0.03, respectively. After evaluating Equations (B.20) and (B.21) to estimate the value of L_e ,

longitudinal pipe strain is calculated using the analytical model given in Equation (B.22). The recommended epistemic uncertainty for this model is 0.3.

$$\varepsilon_p = \frac{\beta_p * L^*}{E} * \left[1 + \frac{n}{1+r} * \left(\frac{\beta_p * L^*}{\sigma_y} \right)^r \right] \quad (\text{B.22})$$

where:

$$L^* = \min \left\{ \begin{array}{l} L_e \\ L/2 \end{array} \right.$$

$$\beta_p = t_{ult} / A$$

$$t_{ult} = \begin{cases} \pi * D * \gamma * H * \tan(\delta * \phi') & - \text{Sand} \\ \pi * D * \alpha * s_u & - \text{Clay} \end{cases}$$

where:

β_p is termed the pipe burial parameter (kPa);

A is the pipe cross-sectional area (m²);

$E = 2 * 10^8$ kPa is the Young's Modulus of steel;

n and r are Ramberg-Osgood parameters.

APPENDIX C:

Damage Models of Wells

Fault Displacement Damage Models for Wells

Using the three modes (1,2, and 4) outlined in Section 3.3, a sensitivity analysis was performed to see which parameters impacted the fault shear through a well the most. Results for the sensitivity analysis of the 12 cases in Table 4 are presented below, accompanied plots presented in by Figure 45 through Figure 56.

First Well Mode – Casing

Figure 45 shows the results of the sensitivity analysis for the casing in the first well mode (cemented annulus case). The results are organized as bar charts representing the values of SRSS for each of the 27 parameters in ascending order. The x-axis represents the percent of the variability in the model. For example, changing the fault angle accounts for a little over 50% of the variability of the model.

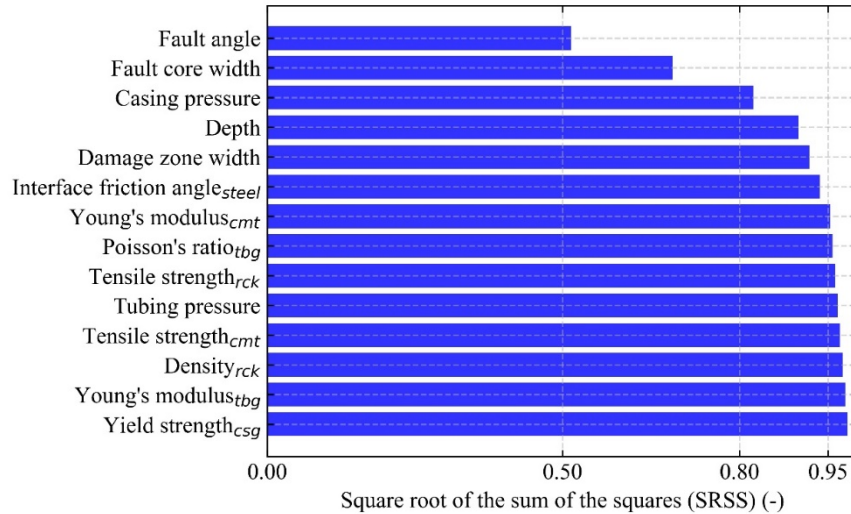
Results show that the top three parameters (i.e., fault angle, fault core width, and casing pressure) accounts for over 80% of the variability of the critical fault displacement. To account for 95% of the variability, additional four parameters (i.e., depth, damage zone width, interface friction angle of steel, and Young's modulus of cement) were needed.

It was found that the geometric parameters had the largest impact on the analysis. Three of the seven parameters are geometric parameters (i.e., fault angle, fault core width, and damage zone width), which directly effect the geometry of the sheared casing. For example, a different fault angle changes the angle at which the casing is sheared.

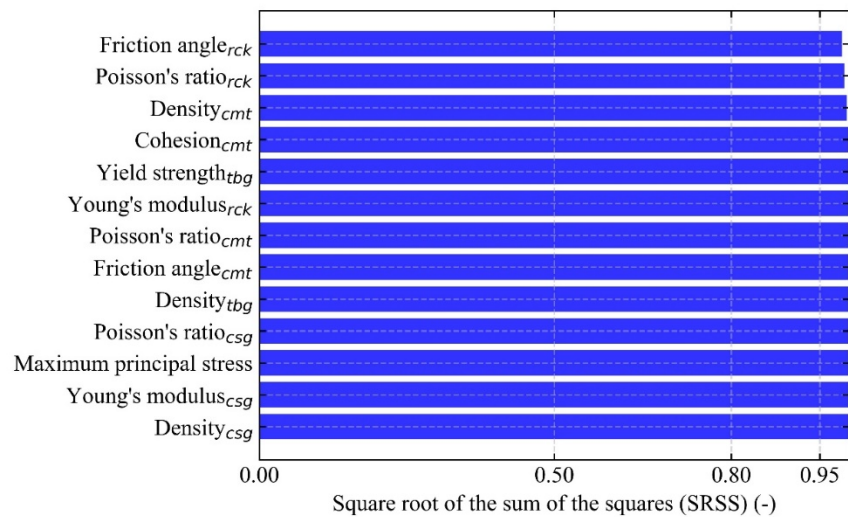
The significance of the other parameters is not as straightforward. The depth and casing pressure both effect the initial stresses of the casing (e.g., rock stresses change with depth, which in turn effects the cement and casing's initial stresses). Whereas the interface friction angle and Young's modulus of the cement effect the stress-strain development of the casing during shearing (e.g., casing is sheared more easily if the cement in the annulus is stiffer).

Figure 45: SRSS values of the model parameters for the casing in the first well mode (cemented annulus case): (a) first to 14th parameters; (b) 15th to 27th parameters

(a)



(b)



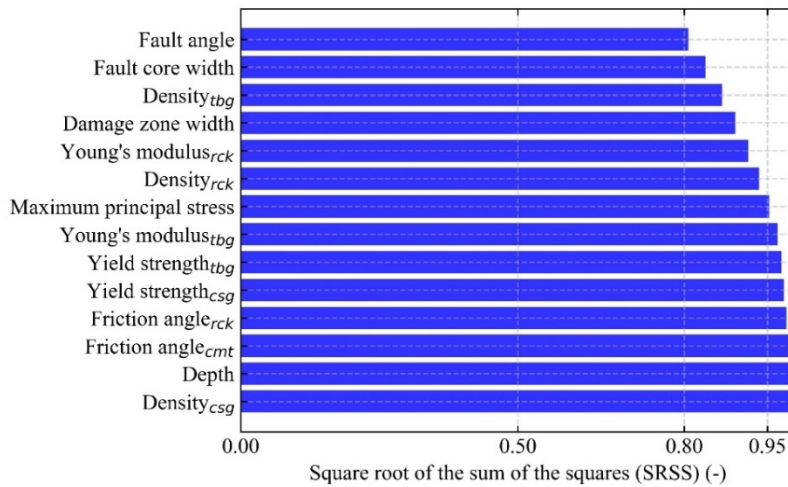
First Well Mode – Tubing

Figure 46 shows the results of the sensitivity analysis for the tubing in the first well mode (cemented annulus case). Similar to the results for the casing, the geometry parameters significantly impacted the tubing sensitivity as they were among the seven key parameters that accounted for 95% of the variability of the critical fault displacement, with fault angle making up 80% of the variability

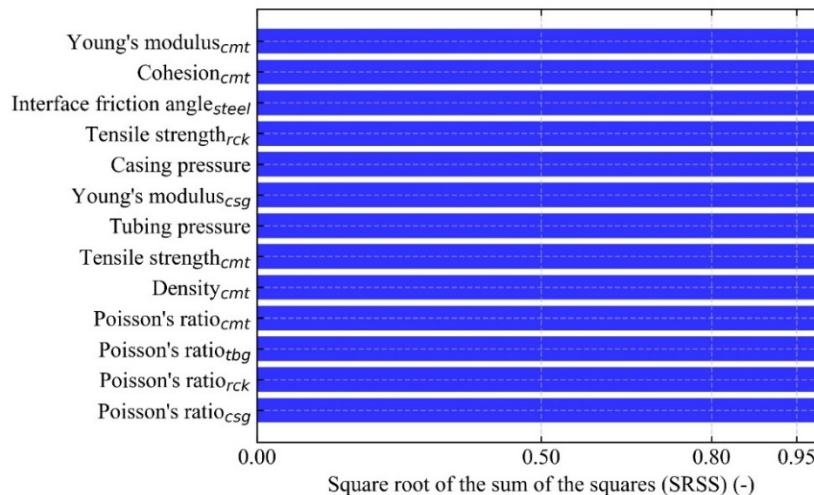
Three of the seven parameters were related to the stiffness and stress levels of the rock (i.e., Young's modulus, density, and maximum horizontal stress of the rock), and the remaining parameter was associated with the tubing stress (i.e., tubing density). Although these rock parameters are not directly related to the well's plastic behavior, different initial stresses and stiffness will result in different plastic deformation profiles in the rock. This could in turn effect the plastic behavior of the tubing. It was also found that the cement and casing behaviors had minor impact on the tubing sensitivity as cement and casing parameters were not included in the seven key parameters.

Figure 46: SRSS values of the model parameters for the tubing in the first well mode (cemented annulus case): (a) first to 14th parameters; (b) 15th to 27th parameters

(a)



(b)



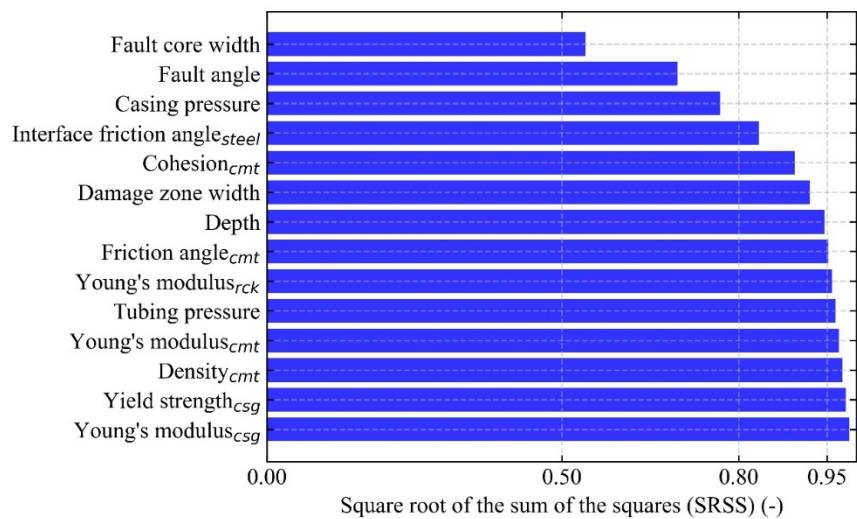
Second Well Mode – Casing

Geometrically, the main differences between the first and second well modes are the borehole and casing diameters. The first mode has a larger diameter borehole (12.25 in vs. 9.875 in) and casing diameter (8.625 in vs. 7 in), with this the thickness of the cement in the first mode is also larger (1.813 in vs. 1.438 in). The casing grades in both well modes are identical (K-55). Thus, it can be hypothesized that the casing sensitivity in a smaller diameter borehole will be more effected by the plastic deformation of the cement rather than that in a larger diameter borehole.

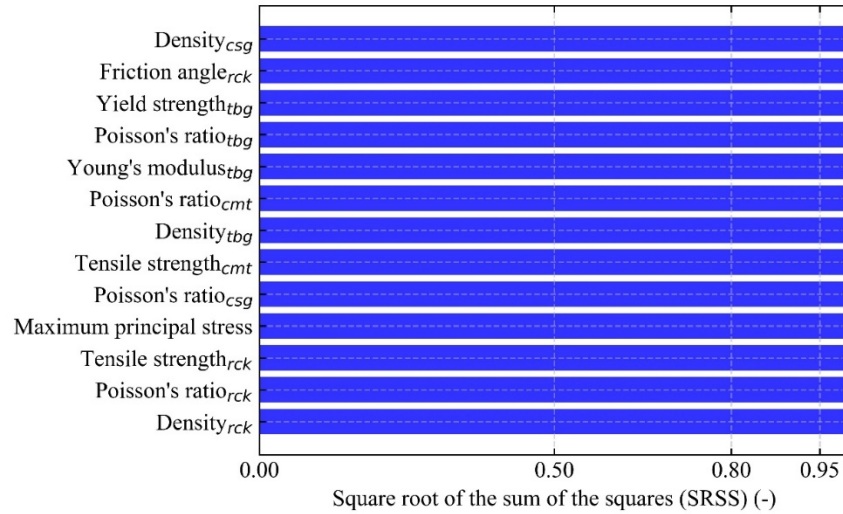
Figure 47 shows the results of the sensitivity analysis for the casing in the second well mode (cemented annulus case). Similar to the first mode, the geometry parameters (i.e., fault angle, fault core width, damage zone width) were among the key parameters that made up 95% of the variability of the critical fault displacement. Depth and casing pressure were also among these key parameters, which change the initial stress levels in the casing. Finally, interface friction angle was also included, which effects how casing deforms during fault shear. The primary difference from the first mode is that cement parameters proved to make up a significant portion of the variability (approximately 20%), namely the cohesion and friction angle of the cement.

Figure 47: SRSS values of the model parameters for the casing in the second well mode (cemented annulus case): (a) first to 14th parameters; (b) 15th to 27th parameters

(a)



(b)

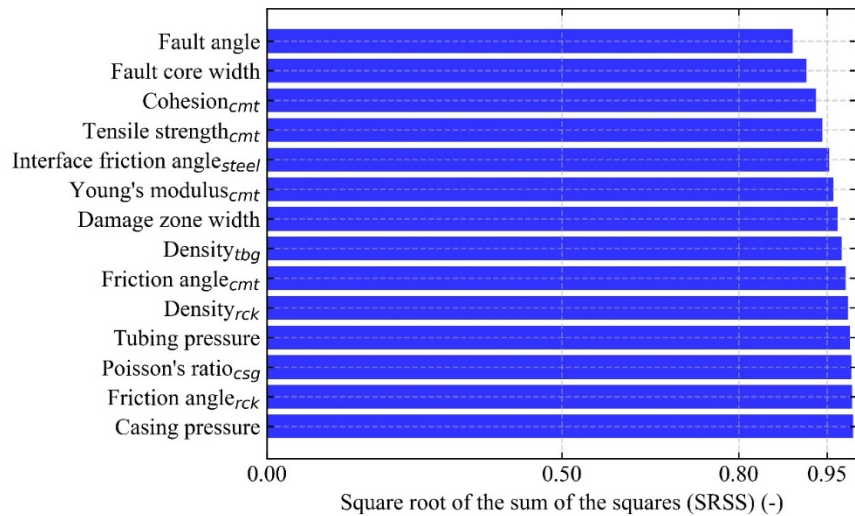


Second Well Mode – Tubing

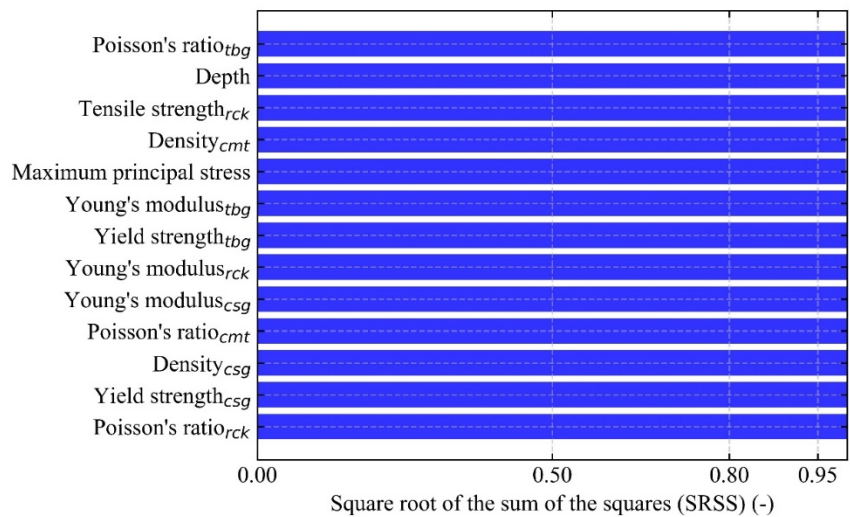
Figure 48 shows the results of the sensitivity analysis for the tubing in the second well mode (cemented annulus case). Results show similar trends discussed for the casing above; cement parameters had greater impact on the tubing sensitivity in the second mode than in the first mode. The cohesion and tensile strength of the cement were included in the top five parameters accounting for 95% of the variability, whereas no cement parameters were included among the key parameters in the first mode results (i.e., rock parameters were included instead). It is also noted, however, that the fault angle alone made up nearly 90% of the variability in the second mode, compared to slightly over 80% in the first mode.

Figure 48: SRSS values of the model parameters for the tubing in the second well mode (cemented annulus case): (a) first to 14th parameters; (b) 15th to 27th parameters

(a)



(b)



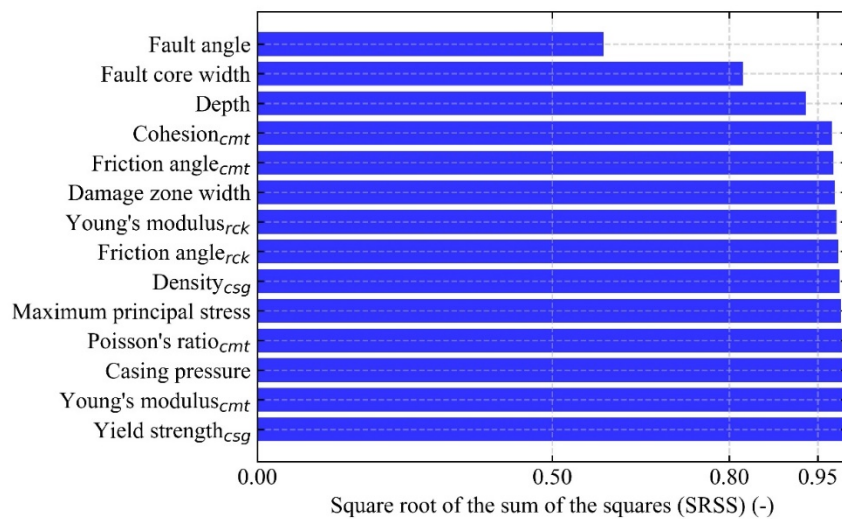
Fourth Well Mode – Casing

Figure 49 shows the results of the sensitivity analysis for the casing in the fourth well mode (cemented annulus case). The parameters that made up 95% of the variability included: fault angle, fault core width, depth, and cement cohesion. It should be noted that fault angle and fault core width were the top two parameters in all the examined well modes (for the cemented annulus cases). In the fourth mode, the geometry parameters (i.e., fault angle and fault core width) were more impactful than in the first and second modes. In fact, these two parameters accounted for roughly 80% of the variability in the fourth mode, whereas they only accounted for around 70% in the first and second modes.

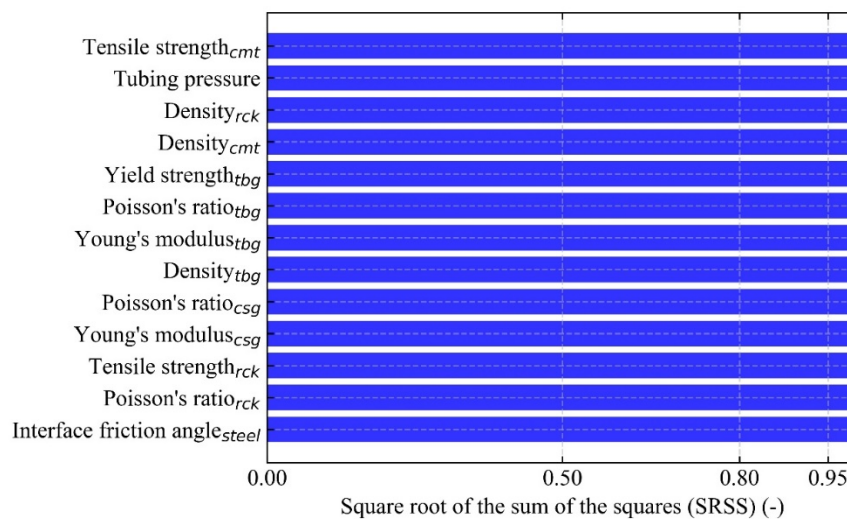
In the fourth mode, the casing grade is different from the first and second modes: N-80 vs. K-55. The diameters are somewhat similar to those of the second mode with a slightly larger borehole (10.625 in vs. 9.875 in) and a slightly smaller casing (6.625 in vs. 7 in). The greater impact of the fault angle and fault core width in the fourth mode could be attributed to the difference in the casing grade. N-80 casing has about 1.4 times greater yield strength than K-55 casing. Also, the minimum elongation of the casing, at which it was assumed to be damaged (i.e., casing elements were removed) was set to a lower value for N-80 casing (26% strain) than for K-55 casing (35-38% strain). Thus, the higher yield strength and smaller minimum elongation are likely the cause of the greater impact of the geometry parameters in the fourth mode.

Figure 49: SRSS values of the model parameters for the casing in the fourth well mode (cemented annulus case): (a) first to 14th parameters; (b) 15th to 27th parameters

(a)



(b)



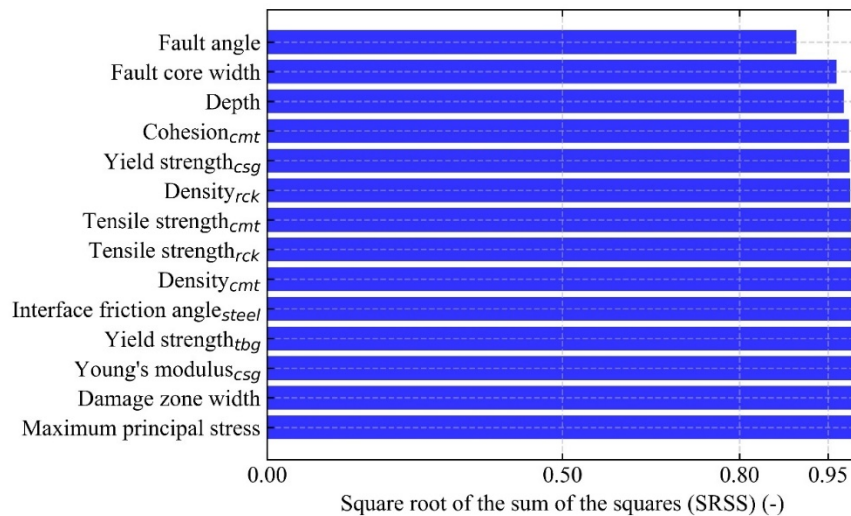
Fourth Well Mode – Tubing

Figure 50 shows the results of the sensitivity analysis for the tubing in the fourth well mode (cemented annulus case). Results were distinctively different from the first and second mode for the tubing; only the top two parameters (i.e., fault angle and fault core width) were enough to exceed the 95% variability threshold.

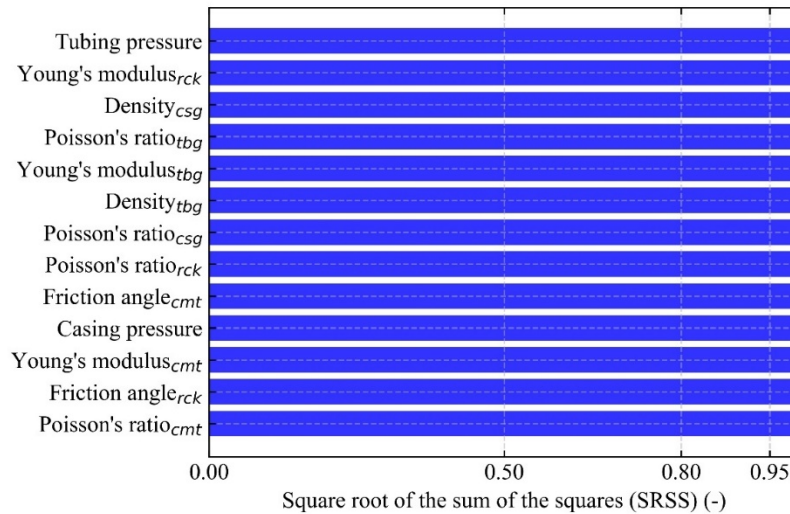
Similar to the results for the fourth mode casing, the number of the key parameters for the fourth mode tubing was much less than for the first and second mode. This again, could be because the stronger casing (N-80) in the fourth mode somewhat nullifies the influence from outside the casing (i.e., rock and cement), therefore increasing the impact of fault angle and fault core width relative to other parameters. It could also be because of the smaller tubing diameter in the fourth mode (2.875 in) compared to that in the other modes (3.5 in). More simulations are necessary to uncover the mechanism behind the reduced number of key parameters in the fourth mode.

Figure 50: SRSS values of the model parameters for the tubing in the fourth well mode (cemented annulus case): (a) first to 14th parameters; (b) 15th to 27th parameters

(a)



(b)



First Well Mode (without cement) – Casing

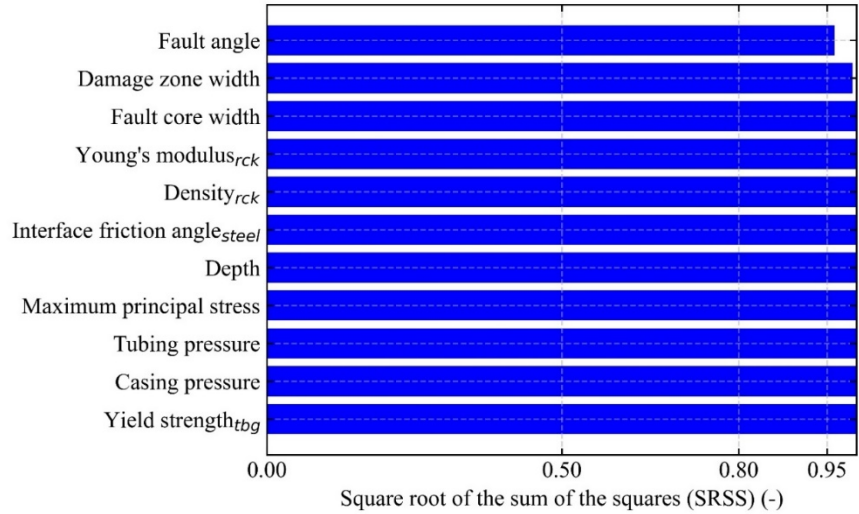
Figure 51 shows the results of the sensitivity analysis for the casing in the first well mode without the cement (i.e., uncemented annulus case). In the uncemented annulus case, the total number of parameters was 22, as the cement parameters were no longer relevant.

Results show that the fault angle alone accounted for over 95% of the variability of the critical fault displacement. The percentage increased to 99% if the second most variable parameter (i.e., damage zone width) was included.

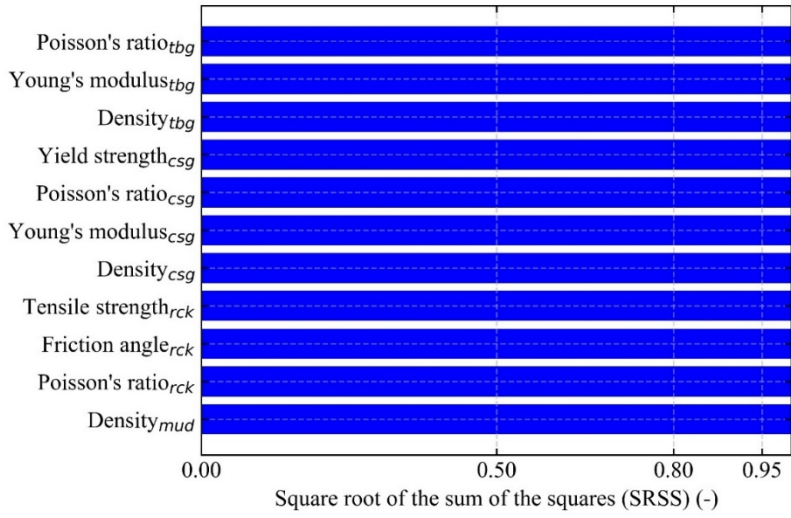
Without the cement, the fault displacement needed to fail the casing differed a lot with fault angle. The damage zone width also proved to be a key parameter. As the damage zone changed, the distribution of the fault displacement perpendicular to the fault also changed significantly (the fault displacement linearly decreased by 20% within the damage zone).

Figure 51: SRSS values of the model parameters for the casing in the first well mode (uncemented annulus case): (a) first to 11th parameters; (b) 12th to 22nd parameters

(a)



(b)

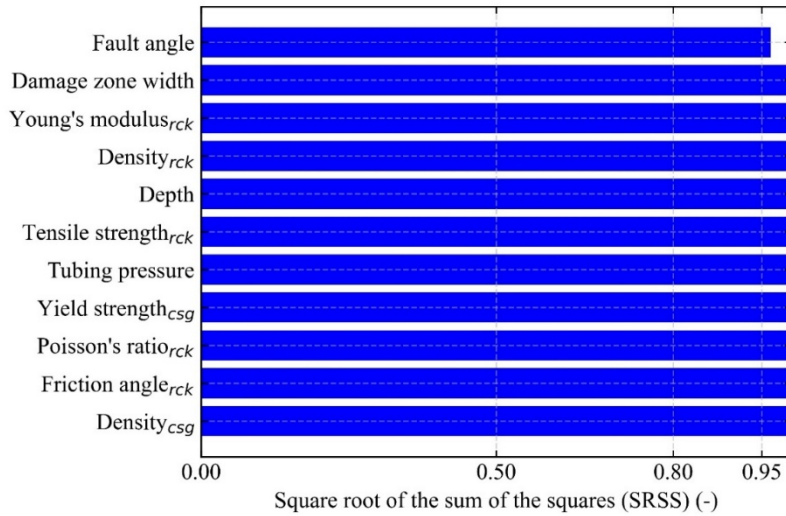


First Well Mode (without cement) – Tubing

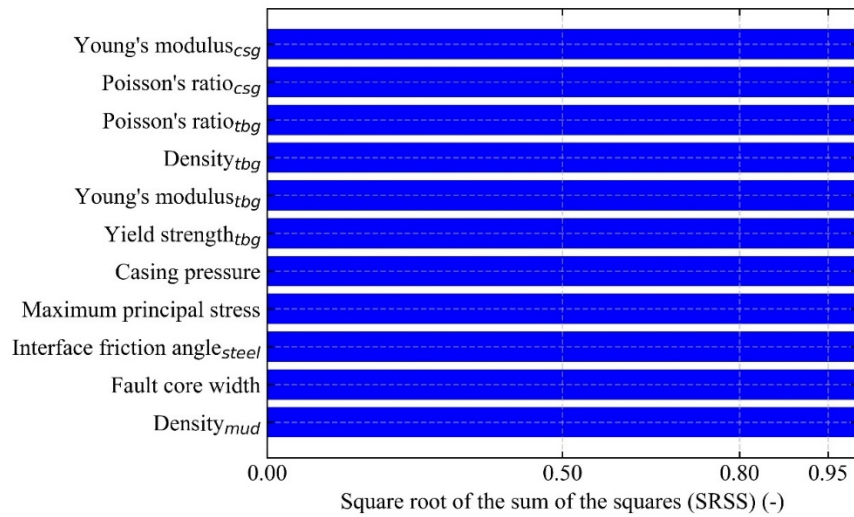
Figure 52 shows the results of the sensitivity analysis for the tubing in the first well mode, uncemented annulus case. Results for the tubing are similar to the results for the casing provided above; the fault angle alone made up over 95% of the variability and the percentage increased to nearly 100% if the damage zone width was included.

Figure 52: SRSS values of the model parameters for the tubing in the first well mode (uncemented annulus case): (a) first to 11th parameters; (b) 12th to 22nd parameters

(a)



(b)

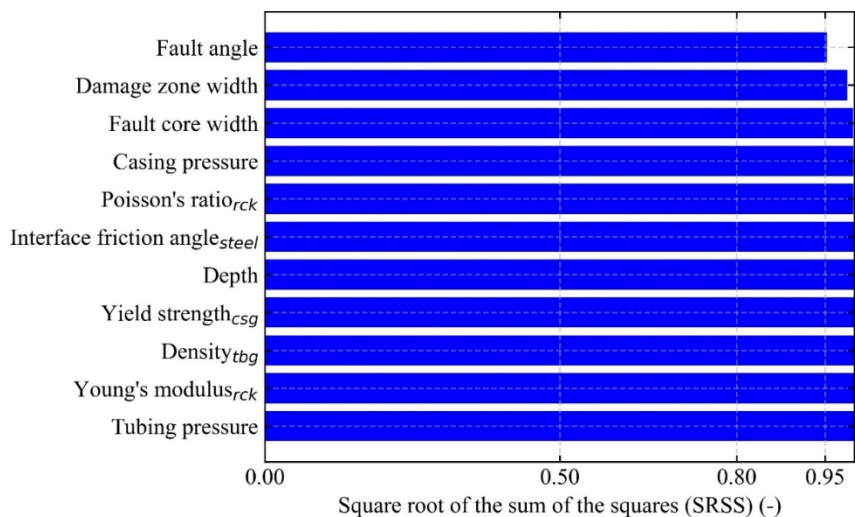


Second Well Mode (without cement) – Casing

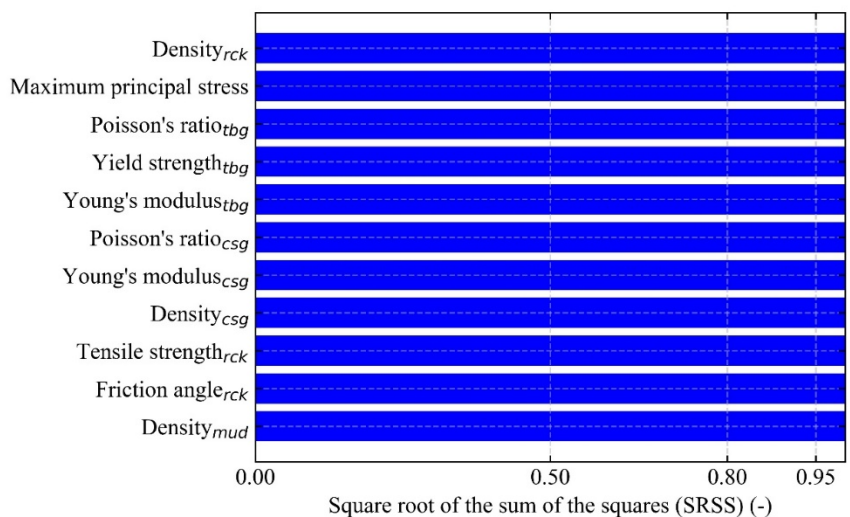
Figure 53 shows the results of the sensitivity analysis for the casing in the second well mode, uncemented annulus case. Results for the second mode were similar to those for the first mode; the key parameter was the fault angle alone. It was also similar that the damage zone width was the second most impactful parameter, which increased the SRSS percentage to nearly 99% when combined with the fault angle.

Figure 53: SRSS values of the model parameters for the casing in the second well mode (uncemented annulus case): (a) first to 11th parameters; (b) 12th to 22nd parameters

(a)



(b)

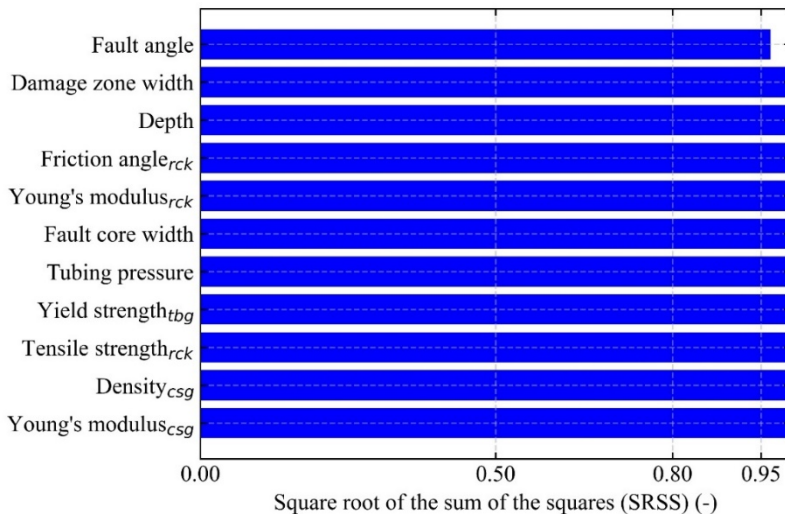


Second Well Mode (without cement) – Tubing

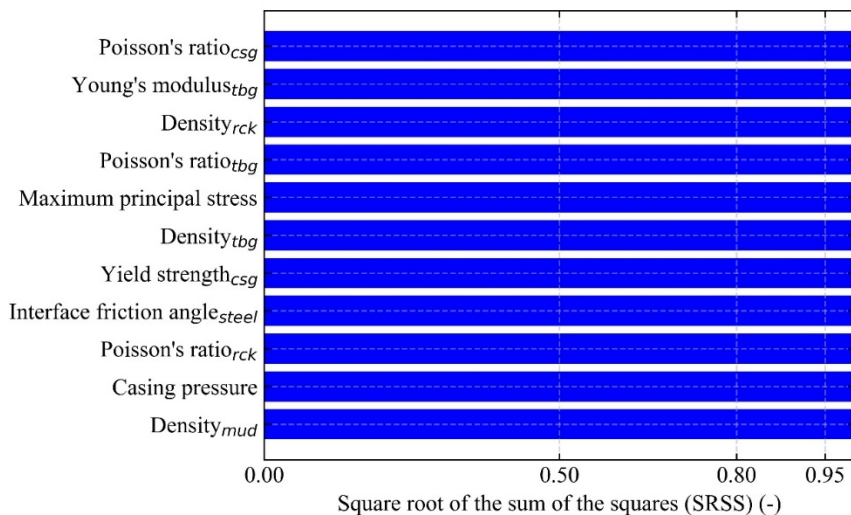
Figure 54 shows the results of the sensitivity analysis for the tubing in the second well mode, uncemented annulus case. Again, trends for the second mode were identical to those for the first mode; the fault angle alone was enough to account for over 95% of the variability. The other parameters would not need to be considered (i.e., fixed at their mean values) in the fragility analysis in the uncemented annulus case.

Figure 54: SRSS values of the model parameters for the tubing in the second well mode (uncemented annulus case): (a) first to 11th parameters; (b) 12th to 22nd parameters

(a)



(b)

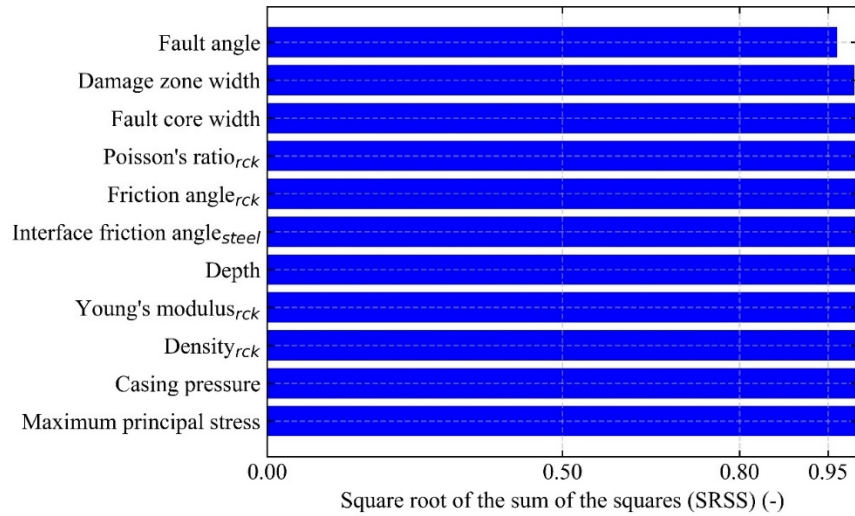


Fourth Well Mode (without cement) – Casing

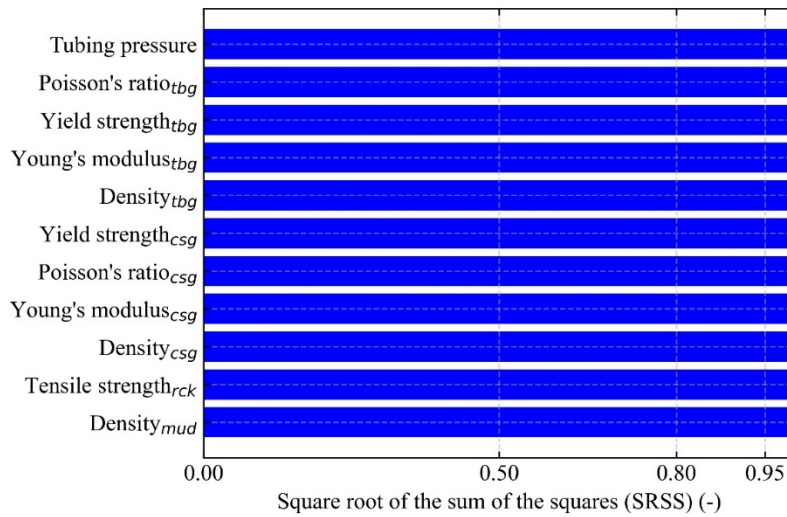
Figure 55 shows the results of the sensitivity analysis for the casing in the fourth well mode, uncemented annulus case. Again, results show that the key parameter in the uncemented annulus case was the fault angle alone, as it exceeded the 95% threshold in SRSS.

Figure 55: SRSS values of the model parameters for the casing in the fourth well mode (uncemented annulus case): (a) first to 11th parameters; (b) 12th to 22nd parameters

(a)



(b)

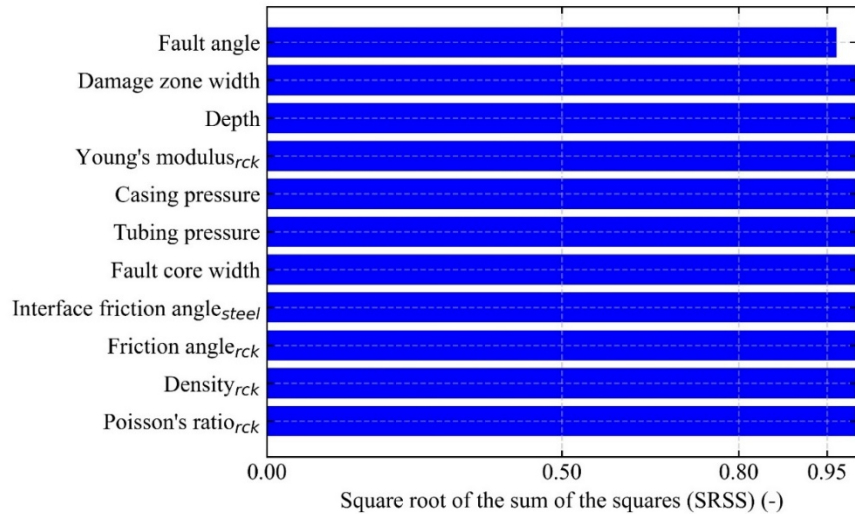


Fourth Well Mode (without cement) – Tubing

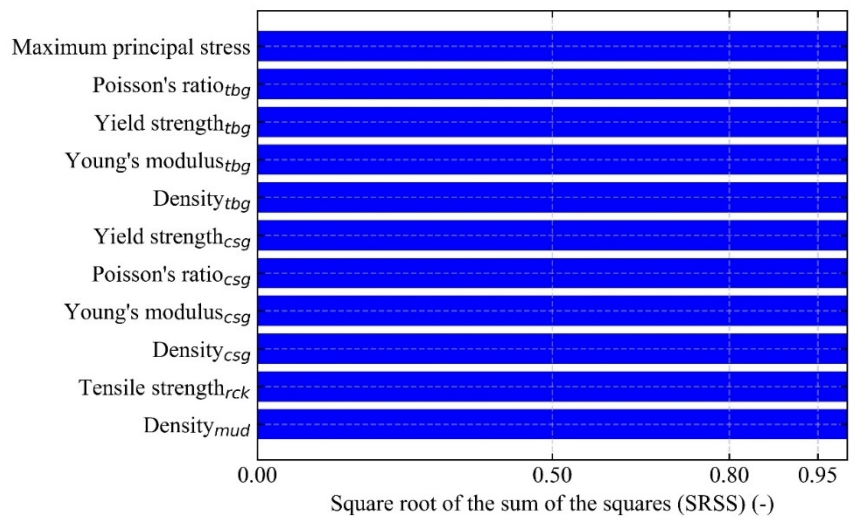
Figure 56 shows the results of the sensitivity analysis for the tubing in the fourth well mode, uncemented annulus case. In this case, too, the only key parameter was the fault angle. Hence, it was shown that, regardless of the well modes, the fault angle alone would account for over 95% of the variability of the critical fault displacement for both casing and tubing in the uncemented annulus case.

Figure 56: SRSS values of the model parameters for the tubing in the fourth well mode (uncemented annulus case): (a) first to 11th parameters; (b) 12th to 22nd parameters

(a)



(b)



Fault Displacement Damage Model

Using the results from the sensitivity analysis, the seven to eight key parameters were used to develop the fragility functions for wells resistance to fault shear. First a relationship for estimating the strain in the well was made and then based on the strain the probability of failure.

First and Second Well Mode with Cement – Casing

$$\gamma_{casing} = (b_0 + b_1\theta + b_2\theta^2)FD \quad (B.23)$$

Where:

γ_{casing} is the mean shear strain on the casing (fractional strains);

θ is the fault intersection angle with the well (degree);

FD is the fault displacement (m);

b_0, b_1, b_2 are the model coefficients given in Table 19;

σ for the model is also provided in Table 19;

Table 19: Coefficients for first and second well mode, with cement for well casing

	First Well Mode		Second Well Mode	
	Value	Coefficient Uncertainty	Value	Coefficient Uncertainty
b_0	-8.275538	2.5874396	11.618	2.8066112
b_1	1.80629	0.1122855	0.768	0.1201202
b_2	-0.022917	0.0011638	-0.011	0.0012453
σ	0.0358501	--	0.03999	--

First Well Mode with Cement – Tubing

$$\gamma_{tubing} = b_0 + b_1\theta + b_2\theta^2 + b_3W_{fc} + b_4W_{dz} + b_5E_{rock} + b_6E_{rock}^2 + b_7(FD - \text{Inflection}) \quad (B.24)$$

Where:

$$\text{Inflection} = 0.1605 - 0.004\theta + 7 * 10^{-5}\theta^2$$

γ_{tubing} is the mean shear strain on the tubing (fractional strains);

θ is the fault intersection angle with the well (degree);

W_{fc} is the fault core width (m);

W_{dz} is the damage zone width (m);

E_{rock} is the Young's modulus of the rock (GPa);

FD is the fault displacement (m);

$b_0, b_1, b_2, b_3, b_4, b_5, b_6, b_7$ are the model coefficients given in Table 20;

σ for the model is also provided in Table 20;

Table 20: Coefficients for first well mode, with cement for well tubing

	Value	Coefficient Uncertainty
b_0	0.0687	0.0418221
b_1	0.0071	0.0007307
b_2	-1E-04	8.38E-06
b_3	-5.468	0.2037631

b_4	-0.07	0.0047576
b_5	-0.015	0.0062922
b_6	0.0007	0.0002768
b_7	7.9829	0.048894
σ	0.0758868	--

Second Well Mode with Cement – Tubing

$$\ln(\gamma_{tubing}) = b_0 + b_1\theta + b_2\theta^2 + b_3W_{fc} + b_4W_{dz} + b_5\phi_{cmt} + b_6(FD - Inflection) \quad (B.25)$$

Where:

$$Inflection = 0.1051 - 0.0026\theta + 5 * 10^{-5}\theta^2$$

$\ln(\gamma_{tubing})$ is the mean shear strain on the tubing (fractional strains);

θ is the fault intersection angle with the well (degree);

W_{fc} is the fault core width (m);

W_{dz} is the damage zone width (m);

ϕ_{cmt} is the internal friction angle of cement (degree);

FD is the fault displacement (m);

$b_0, b_1, b_2, b_3, b_4, b_5, b_6$ are the model coefficients given in Table 21;

σ for the model is also provided in Table 21;

Table 21: Coefficients for second well mode, with cement for well tubing

	Value	Coefficient Uncertainty
b_0	-0.01446323	0.0312007
b_1	0.001322172	0.0010284
b_2	-3.7928E-05	1.18E-05
b_3	-7.12563043	0.2701342
b_4	0.025936262	0.0060125
b_5	0.004351959	0.0008291
b_6	7.985906205	0.0627638
σ	0.1015194	--

Fourth Well Mode with Cement – Tubing

$$\gamma_{tubing} = b_0 + b_1\theta + b_2\theta^2 + b_3W_{fc} + b_4W_{dz} + b_5UCS_{cmt} + b_6(FD - Inflection) \quad (B.26)$$

Where:

$$Inflection = 0.982 - 0.0023\theta + 5 * 10^{-5}\theta^2$$

γ_{tubing} is the mean shear strain on the tubing (fractional strains);

θ is the fault intersection angle with the well (degree);

W_{fc} is the fault core width (m);
 W_{dz} is the damage zone width (m);
 UCS_{cmt} is the uniaxial compressive strength of cement (MPa);
 FD is the fault displacement (m);
 $b_0, b_1, b_2, b_3, b_4, b_5, b_6$ are the model coefficients given in Table 22;
 σ for the model is also provided in Table 22;

Table 22: Coefficients for fourth well mode, with cement for well tubing

	Value	Coefficient Uncertainty
b_0	-0.13191017	0.0310005
b_1	0.006023247	0.0011196
b_2	-5.7215E-05	1.28E-05
b_3	-6.62380392	0.2793475
b_4	-0.01366112	0.0062429
b_5	0.00223905	0.000316
b_6	9.01981912	0.08368
σ	0.092901	--

Fourth Well Mode with Cement – Casing

$$\gamma_{casing} = (b_0 + b_1\theta)FD \quad (B.27)$$

Where:

γ_{casing} is the mean shear strain on the casing (fractional strains);
 θ is the fault intersection angle with the well (degree);
 FD is the fault displacement (m);
 b_0, b_1 are the model coefficients given in Table 23;
 σ for the model is also provided in Table 23;

Table 23: Coefficients for fourth well mode, with cement for well casing

	Value	Coefficient Uncertainty
b_0	21.999	0.5923428
b_1	-0.176	0.0120133
σ	0.0290133	--

First and Second Well Mode without Cement – Casing

$$\ln(\gamma_{casing}) = b_0 + b_1\theta + b_2\theta^2 + b_3(\ln(FD)) + b_4(\ln(FD))^2 \quad (B.28)$$

Where:

$\ln(\gamma_{casing})$ is the mean shear strain on the casing (fractional strains);

θ is the fault intersection angle with the well (degree);
 FD is the fault displacement (m);
 b_0, b_1, b_2, b_3, b_4 are the model coefficients given in Table 24;
 σ for the model is also provided in Table 24;

Table 24: Coefficients for well modes, with no cement for the well casing

	First Well Mode		Second Well Mode	
	Value	Coefficient Uncertainty	Value	Coefficient Uncertainty
b_0	1.277195	0.1010673	1.0635	0.1287453
b_1	0.003095	0.0010972	0.0033	0.001084
b_2	-0.000142124	1.312E-05	-1E-04	1.29E-05
b_3	0.326506	0.1220671	0.1508	0.1378227
b_4	-0.103797	0.0334055	-0.112	0.0339996
σ	0.0358501	--	0.0306518	--

First, Second, and Fourth without Cement – Tubing

$$\ln(\gamma_{tubing}) = b_0 + b_1\theta + b_2\theta^2 + b_3(FD) + b_4(FD)^2 \tag{B.29}$$

Where:

$\ln(\gamma_{tubing})$ is the mean shear strain on the tubing (fractional strains);
 θ is the fault intersection angle with the well (degree);
 FD is the fault displacement (m);
 b_0, b_1, b_2, b_3, b_4 are the model coefficients given in Table 25;
 σ for the model is also provided in Table 25;

Table 25: Coefficients for first, second, and fourth without cement - tubing

	First Well Mode		Second Well Mode		Fourth Well Mode	
	Value	Uncertainty	Value	Uncertainty	Value	Uncertainty
b_0	-22.8	0.5091342	-17.2	0.4542599	-20.96	0.6306581
b_1	0.139	0.0162092	0.132	0.0150843	0.1935	0.0193646
b_2	-0.005	0.0002068	-0.004	0.0001885	-0.005	0.0002456
b_3	112.3	3.6056369	105.03	4.165491	109.62	5.0903327
b_4	-90.96	4.9563222	-104.1	7.6911975	-93.05	7.9074171
σ	0.554448	--	0.5203696	--	0.6253589	--

Fourth Well Mode without Cement – Casing

$$\ln(\gamma_{casing}) = b_0 + b_1\theta + b_2\theta^2 + b_3\ln(FD) + b_4\ln(FD)^2 \tag{B.30}$$

Where:

$\ln(\gamma_{casing})$ is the mean shear strain on the casing (fractional strains);

θ is the fault intersection angle with the well (degree);
 FD is the fault displacement (m);
 b_0, b_1, b_2, b_3, b_4 are the model coefficients given in Table 26;
 σ for the model is also provided in Table 26;

Table 26: Coefficients for fourth well mode without cement - casing

	Value	Coefficient Uncertainty
b_0	1.4167	0.1079491
b_1	0.0049	0.0007755
b_2	-1E-04	9.79E-06
b_3	0.75	0.1269571
b_4	0.0445	0.0345247
σ	0.0184673	--

Ground Shaking Damage Models for Wells

The following subsections are for ground shaking induced damage on wells. Figure 57 to Figure 80 show the results of the sensitivity analysis for the casings and tubing for three different ground motions, namely RSN548_CHALFANT.A_A-BEN (PGA = 0.2 g), RSN77_SFERN_PUL (PGA = 1.2 g), and RSN825_CAPEMEND_CPM (PGA = 1.5 g). Only the top 12 parameters are shown, i.e., the bottom 12 parameters are cropped out but were accounted for in the analysis. The vertical red solid line corresponds to a SRSS value of 0.95, allowing to visually identify which parameters account for 95% of the model variability.

First Well Mode

This subsection summarizes the results of the sensitivity analysis for the first well mode for a selection of ground motions, namely RSN548_CHALFANT.A_A-BEN and RSN77_SFERN_PUL.

RSN548_CHALFANT.A_A-BEN

Figure 57 to Figure 60 show the results of the sensitivity analysis for the ground motion RSN548_CHALFANT.A_A-BEN for all the casings and tubing of the first well mode.

For the casings, the mass of the wellhead accounts by itself for more than 90% of the model variability, yet the angle of internal friction of the soil is required to reach a SRSS value of 95%. For the tubing, the mass of the wellhead alone already accounts for 95% of the model variability.

RSN77_SFERN_PUL

Figure 61 to Figure 64 show the results of the sensitivity analysis for the ground motion RSN77_SFERN_PUL for all the casings and tubing of the first well mode.

For the casings, the height and mass of the wellhead appear to contribute the most, and account for more than 95% of the model variability. This can be associated to the fact that these parameters effect the inertia due to the free motion of the wellhead attached to the casing system. For the tubing, the top parameter is the mass of the wellhead as well explaining about 77% of the model variability. However, for that sensitivity case, the tubing’s Young’s modulus and yield strength, and the conductor casing Young’s modulus, each contribute to the SRSS by 5%. The fifth top parameter is the height of the wellhead which should be considered to reach the 95% SRSS threshold.

Figure 57: Sensitivity Analysis Result for Conductor Casing (RSN548_CHALFANT.A_A-BEN)

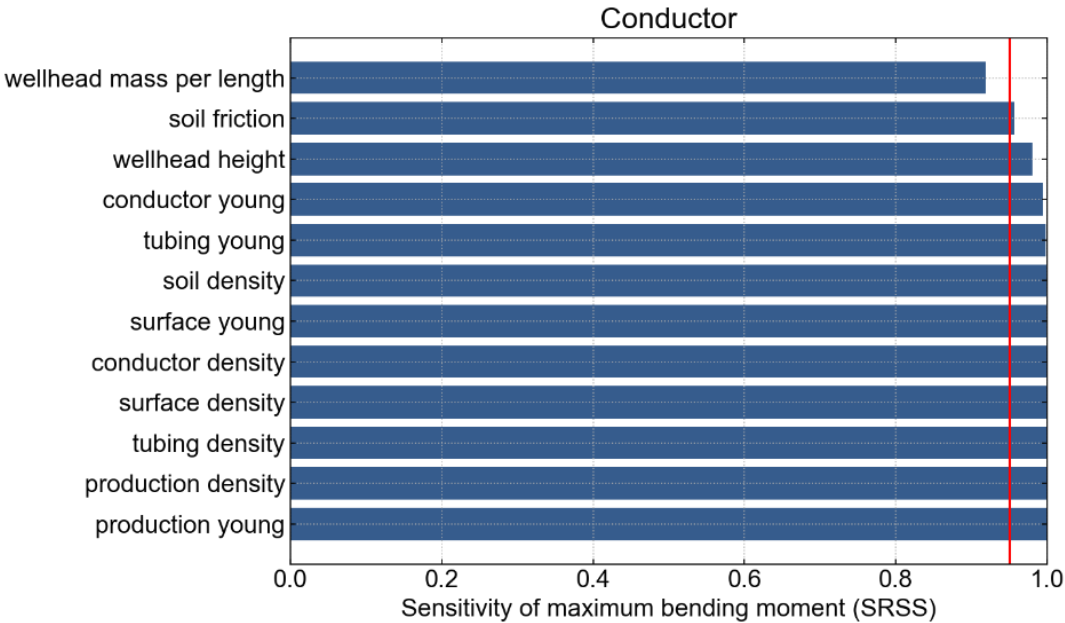


Figure 58: Sensitivity Analysis Result for Surface Casing (RSN548_CHALFANT.A_A-BEN)

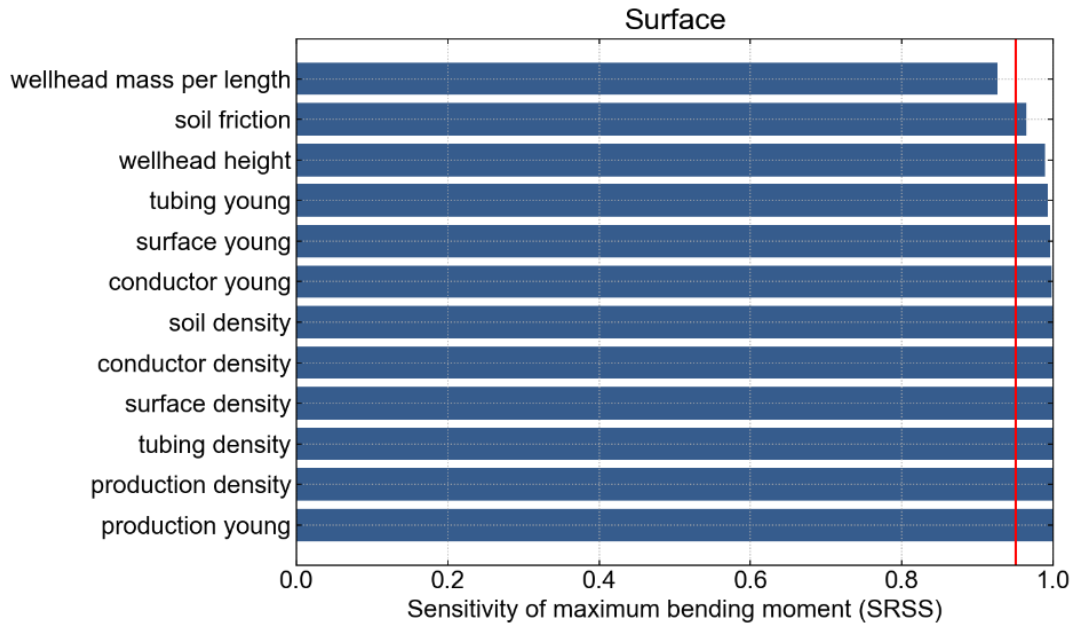


Figure 59: Sensitivity Analysis Result for Production Casing (RSN548_CHALFANT.A_A-BEN)

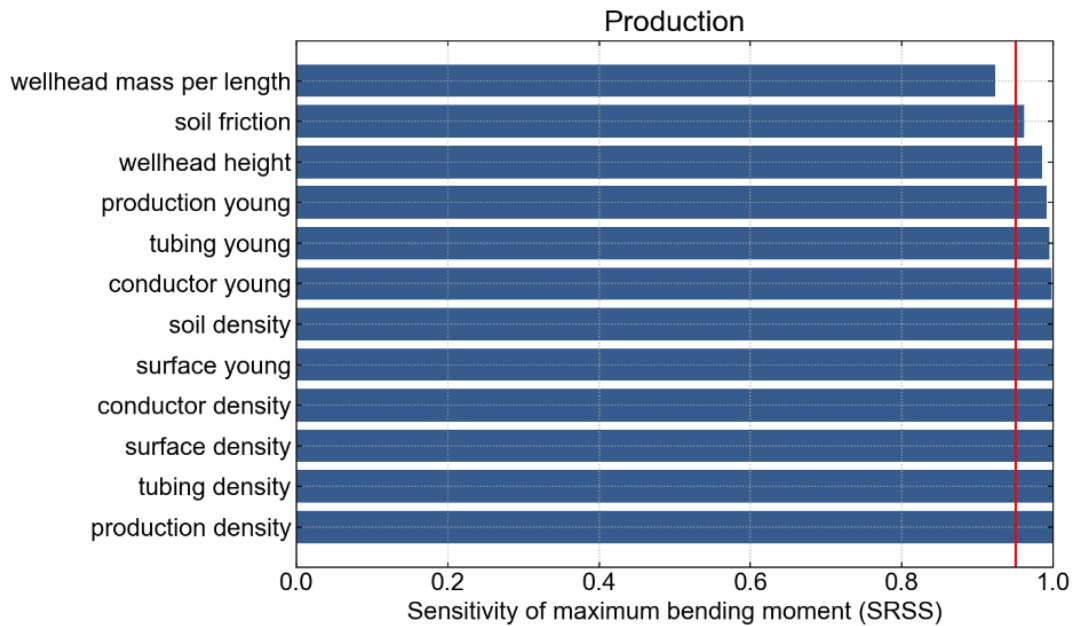


Figure 60: Sensitivity Analysis Result for Tubing (RSN548_CHALFANT.A_A-BEN)

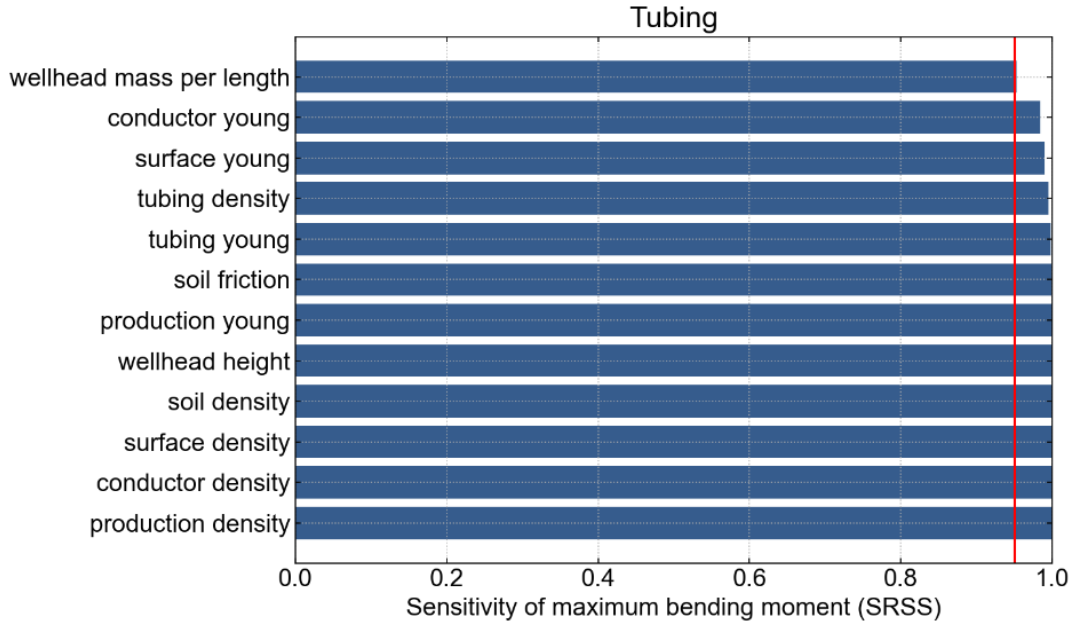


Figure 61: Sensitivity Analysis Result for Conductor Casing (RSN77_SFERN_PUL)

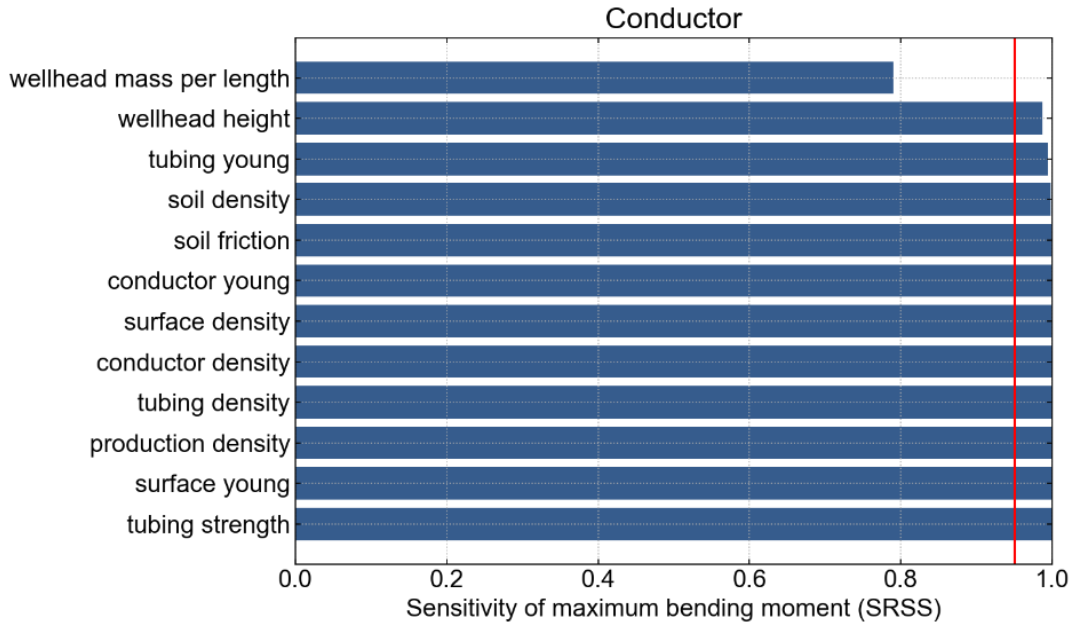


Figure 62: Sensitivity Analysis Result for Surface Casing (RSN77_SFERN_PUL)

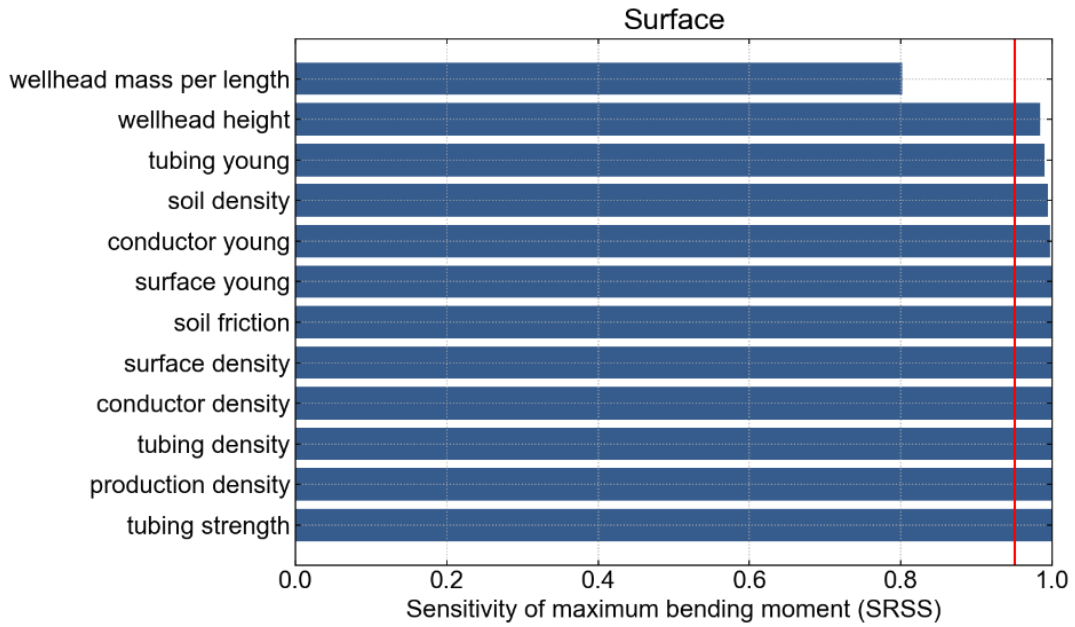


Figure 63: Sensitivity Analysis Result for Production Casing (RSN77_SFERN_PUL)

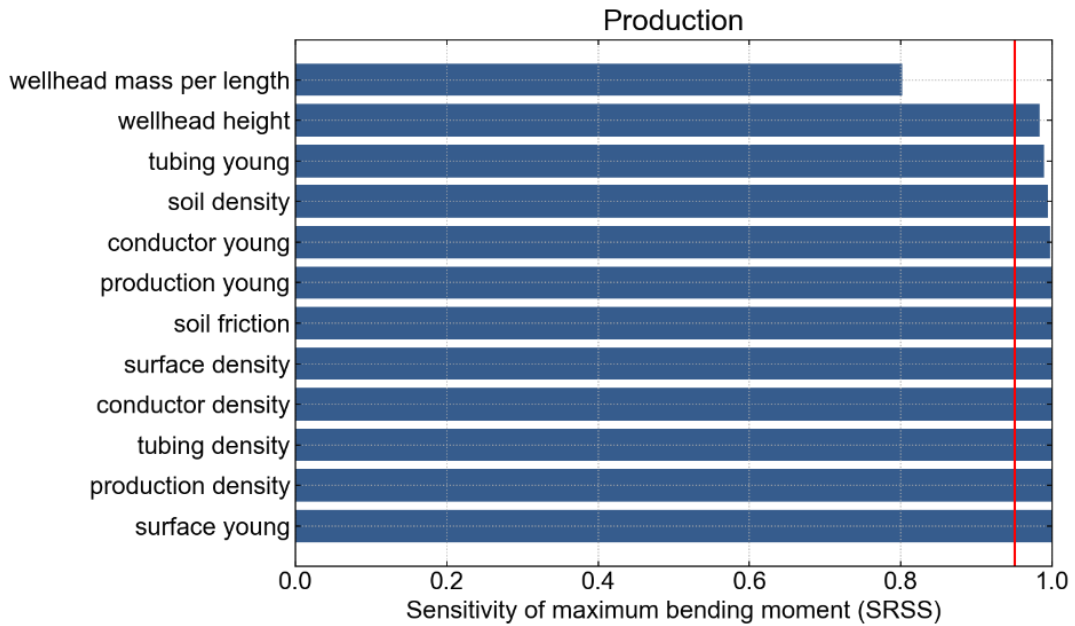
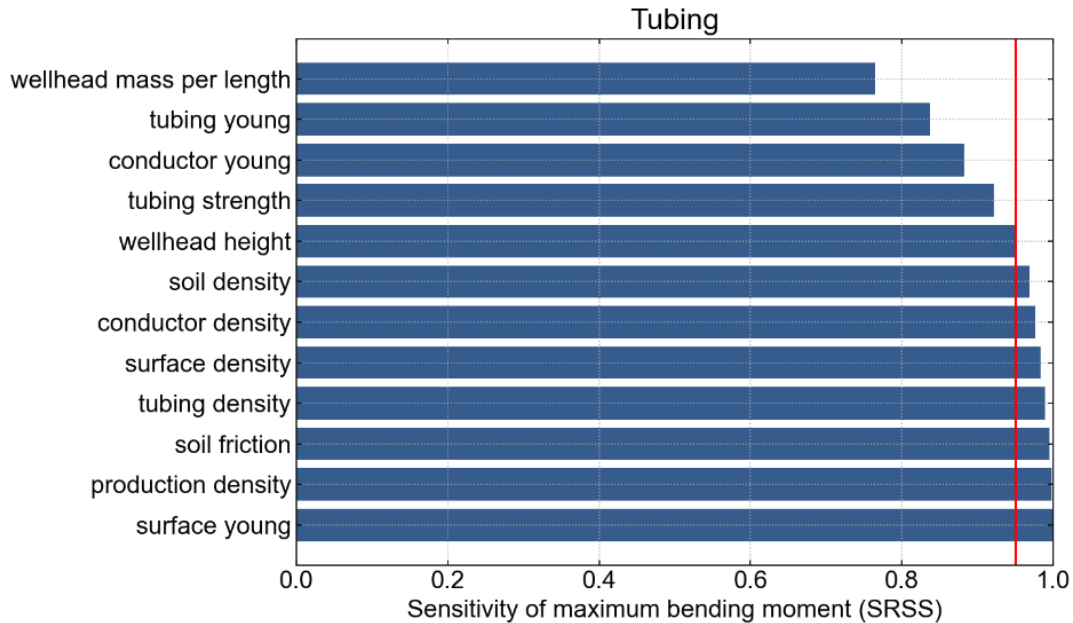


Figure 64: Sensitivity Analysis Result for Tubing (RSN77_SFERN_PUL)



Second Well Mode

This subsection summarizes the results of the sensitivity analysis for the second well mode for a selection of ground motions, namely RSN548_CHALFANT.A_A-BEN and RSN77_SFERN_PUL.

RSN548_CHALFANT.A_A-BEN

Figure 65 to Figure 68 show the results of the sensitivity analysis for the ground motion RSN548_CHALFANT.A_A-BEN for all the casings and tubing of the second well mode.

For the casings, the mass and the height of the wellhead accounts for more than 95% of the model variability. For the tubing, the results of the sensitivity analysis are similar to first well mode and the mass of the wellhead alone already accounts for 95% of the model variability.

RSN77_SFERN_PUL

Figure 69 to Figure 72 show the results of the sensitivity analysis for the ground motion RSN77_SFERN_PUL for all the casings and tubing of the second well mode.

For the casings, the top parameters are the same as that of First well mode with the height and mass of the wellhead contributing up to 99% of the model variability. For the tubing, the top two parameters are the tubing’s Young’s modulus and yield strength, accounting for 80% of the model variability, followed by the mass of the wellhead and the angle of internal friction of the soil. These four parameters constitute 95% of the overall SRSS.

Figure 65: Sensitivity Analysis Result for Conductor Casing (RSN548_CHALFANT.A_A-BEN)

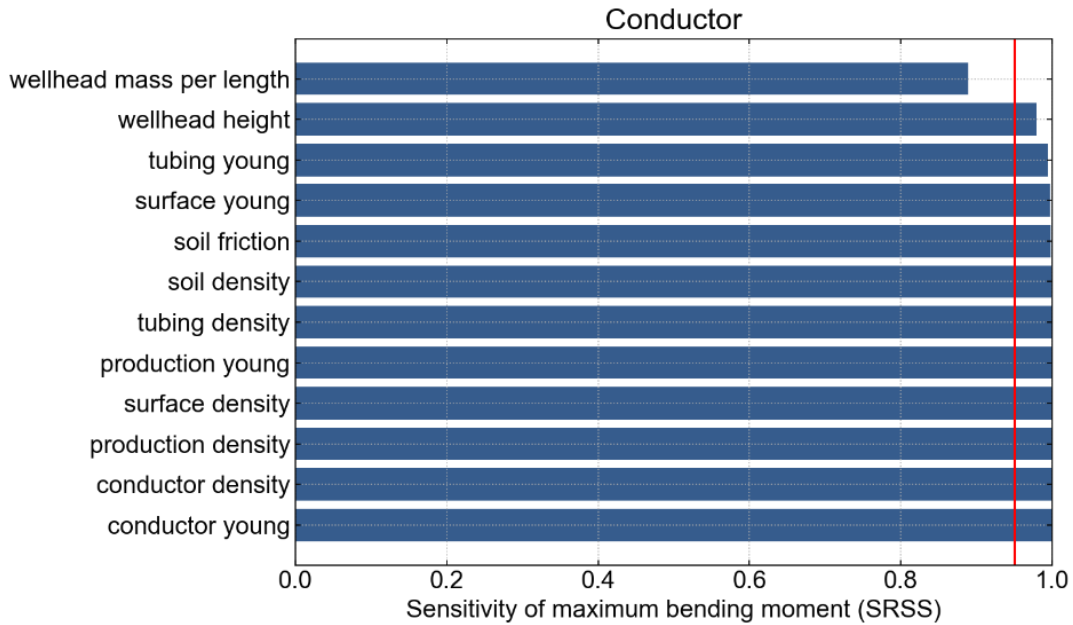


Figure 66: Sensitivity Analysis Result for Surface Casing (RSN548_CHALFANT.A_A-BEN)

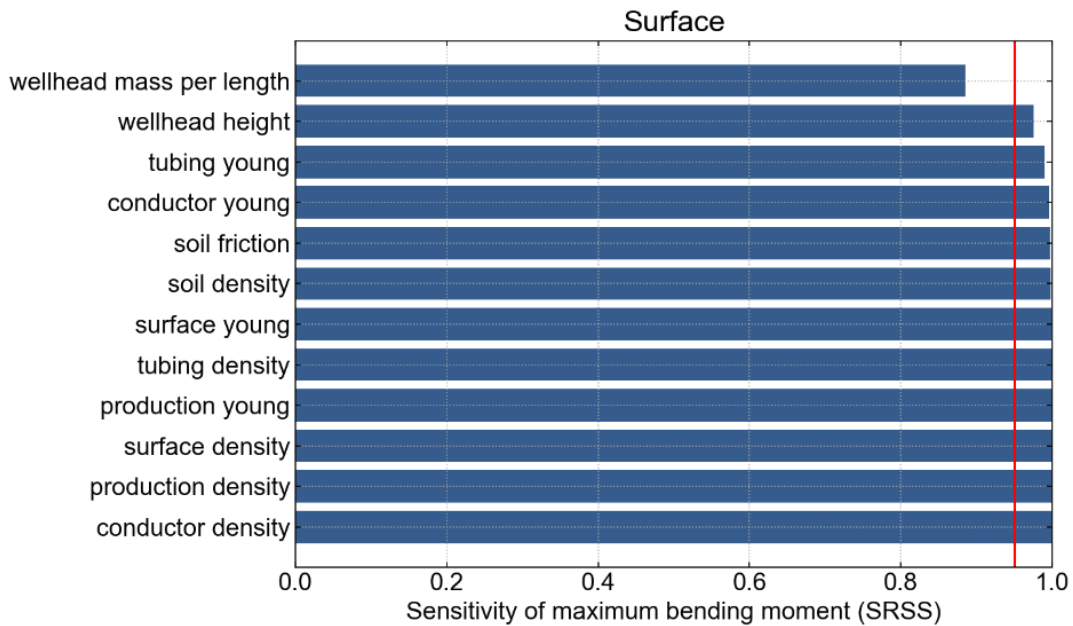


Figure 67: Sensitivity Analysis Result for Production Casing (RSN548_CHALFANT.A_A-BEN)

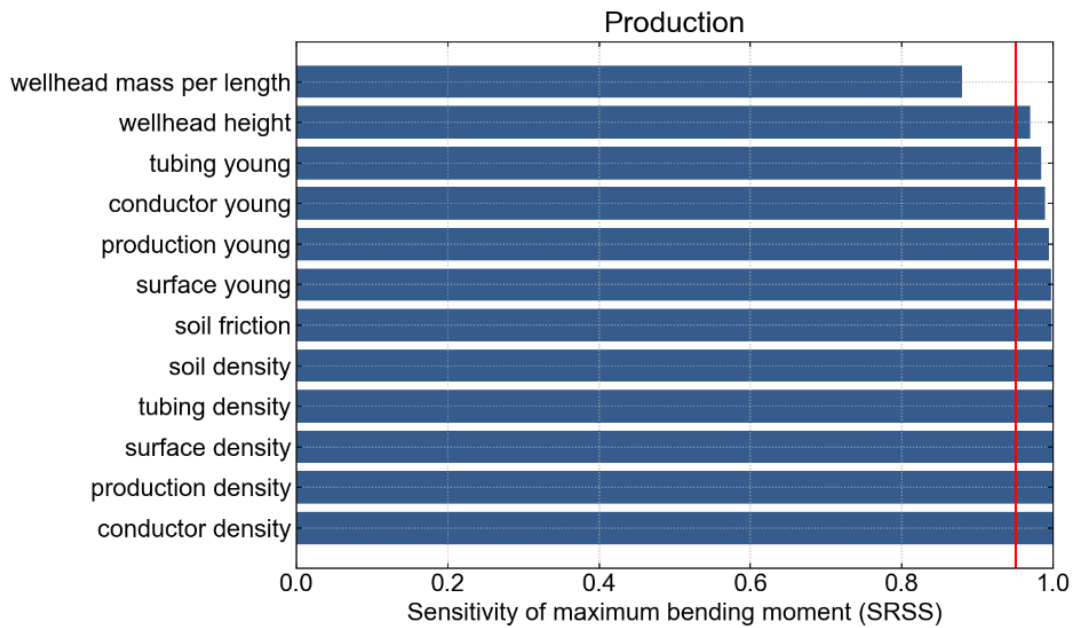


Figure 68: Sensitivity Analysis Result for Tubing (RSN548_CHALFANT.A_A-BEN)

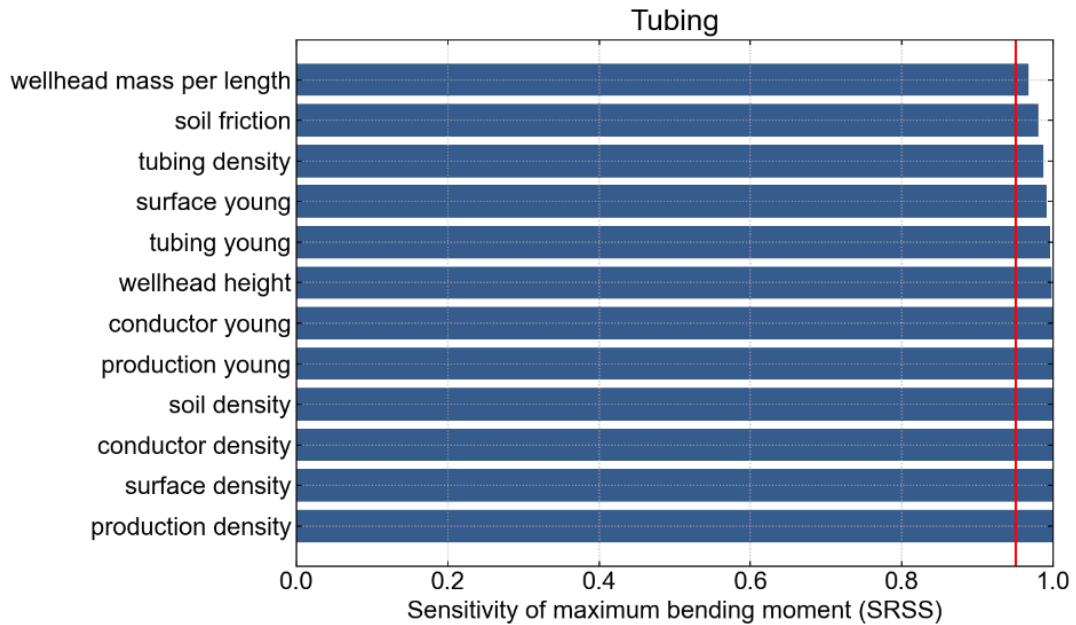


Figure 69: Sensitivity Analysis Result for Conductor Casing (RSN77_SFERN_PUL)

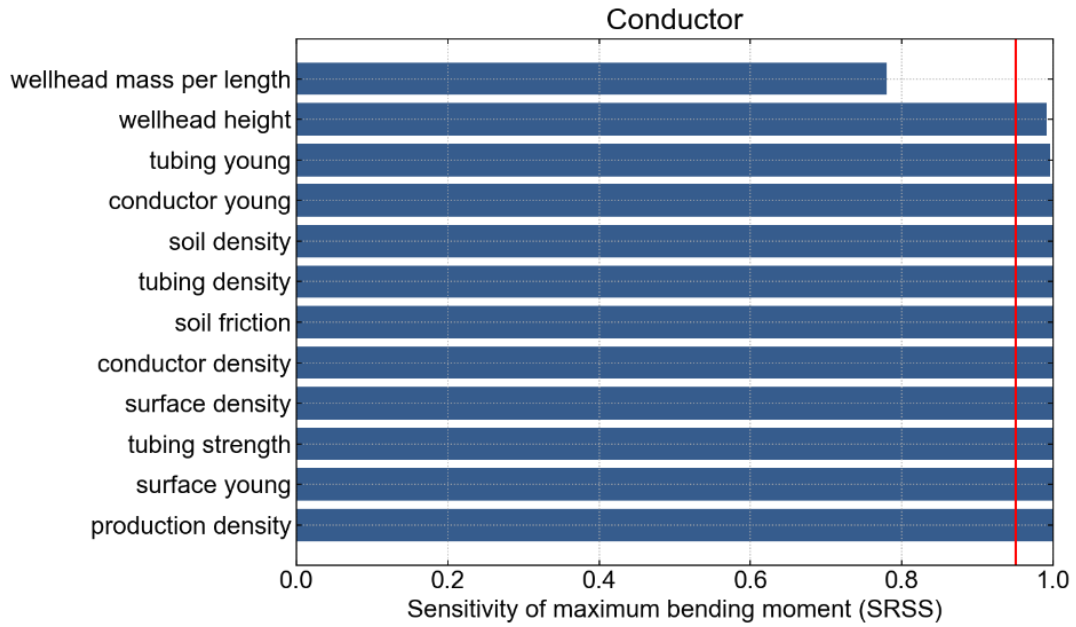


Figure 70: Sensitivity Analysis Result for Surface Casing (RSN77_SFERN_PUL)

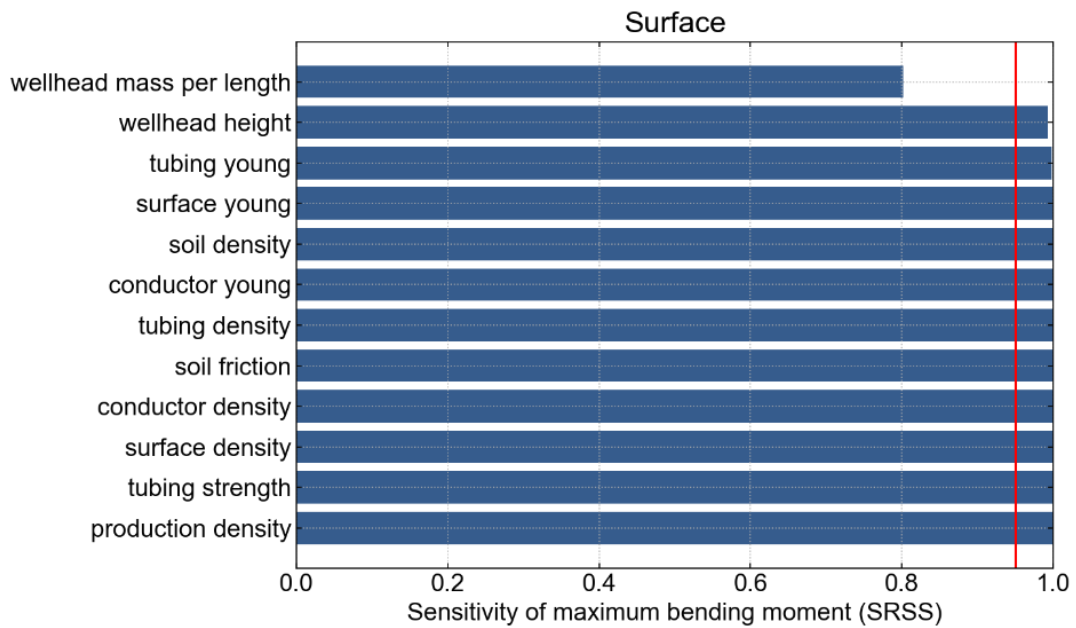


Figure 71: Sensitivity Analysis Result for Production Casing (RSN77_SFERN_PUL)

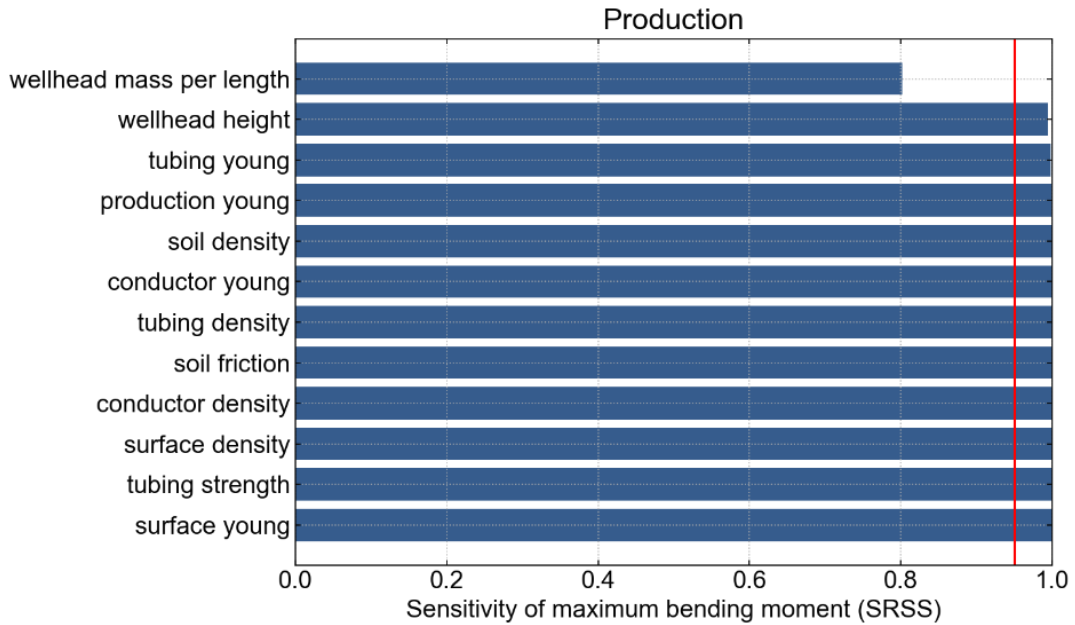
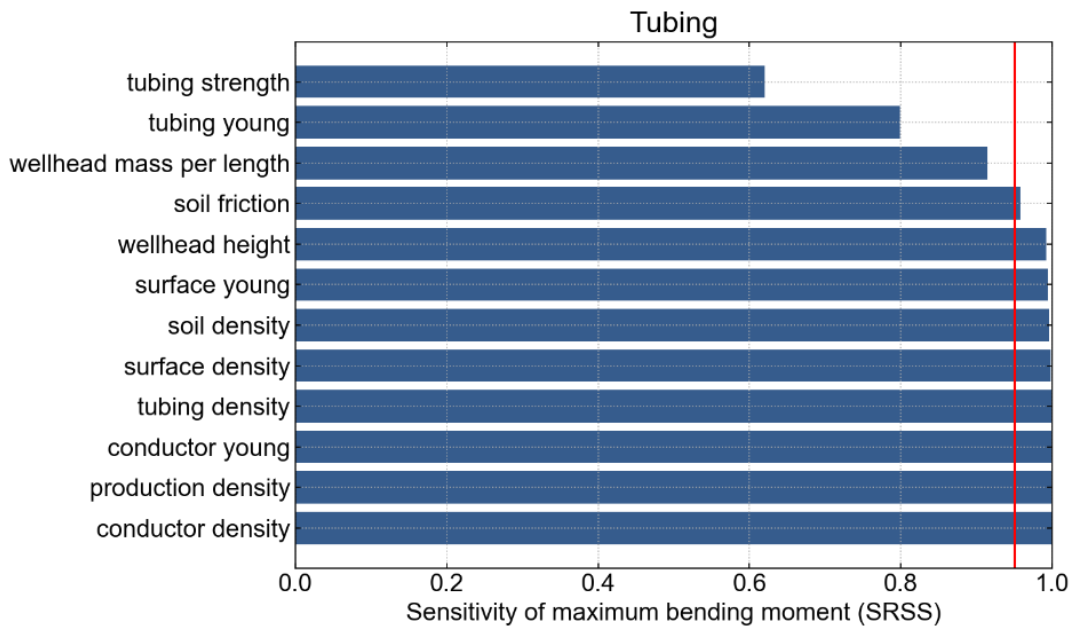


Figure 72: Sensitivity Analysis Result for Tubing (RSN77_SFERN_PUL)



Fourth Well Mode

This subsection summarizes the results of the sensitivity analysis for the fourth well mode for a selection of ground motions, namely RSN548_CHALFANT.A_A-BEN and RSN77_SFERN_PUL.

RSN548_CHALFANT.A_A-BEN

Figure 73 to Figure 76 show the results of the sensitivity analysis for the ground motion RSN548_CHALFANT.A_A-BEN for all the casings and tubing of the fourth well mode.

For the casings, the results of the sensitivity analysis are comparable to second well mode with the mass and height of the wellhead accounting for more than 90% of the model variability. However, the angle of internal friction of the soil must be accounted for to reach the 95% SRSS threshold. For the tubing, only the mass and height of the wellhead are required to explain more than 95% of the model variability.

RSN77_SFERN_PUL

Figure 77 to Figure 80 show the results of the sensitivity analysis for the ground motion RSN77_SFERN_PUL for all the casings and tubing of the fourth well mode.

For the casings, the results are comparable to the weaker ground motion with the mass and height of the wellhead, along with the angle of internal friction of the soil contributing to 95% of the SRSS. For the tubing, the top four parameters are the tubing's yield strength, the mass of the wellhead, the angle of internal friction of the soil, and the tubing's Young's modulus, accounting for more than 95% of the model variability.

Figure 73: Sensitivity Analysis Result for Conductor Casing (RSN548_CHALFANT.A_A-BEN)

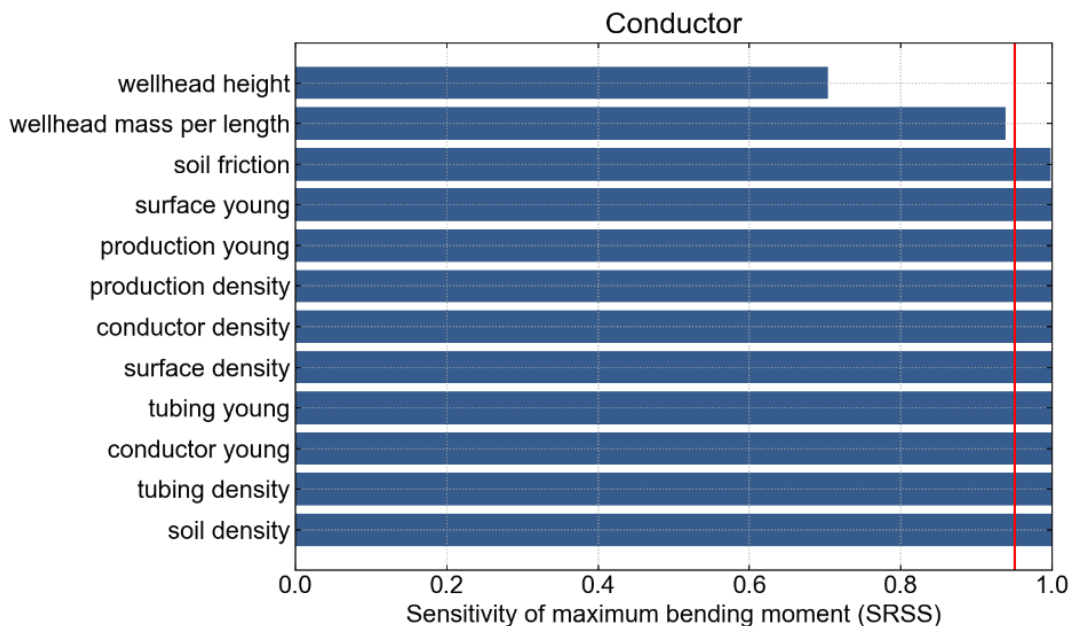


Figure 74: Sensitivity Analysis Result for Surface Casing (RSN548_CHALFANT.A_A-BEN)

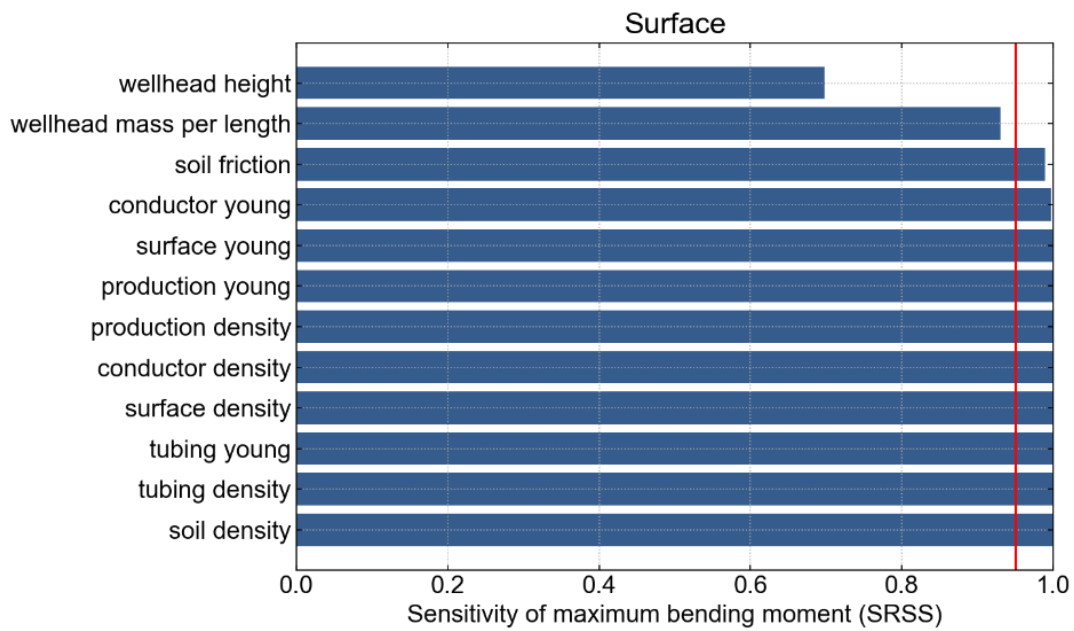


Figure 75: Sensitivity Analysis Result for Production Casing (RSN548_CHALFANT.A_A-BEN)

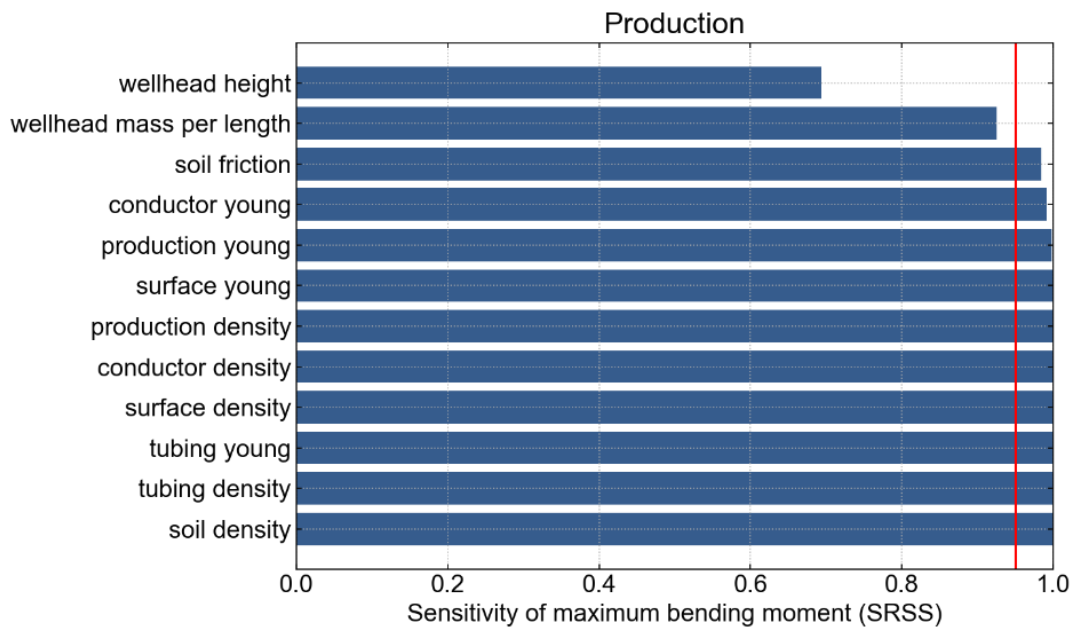


Figure 76: Sensitivity Analysis Result for Tubing (RSN548_CHALFANT.A_A-BEN)

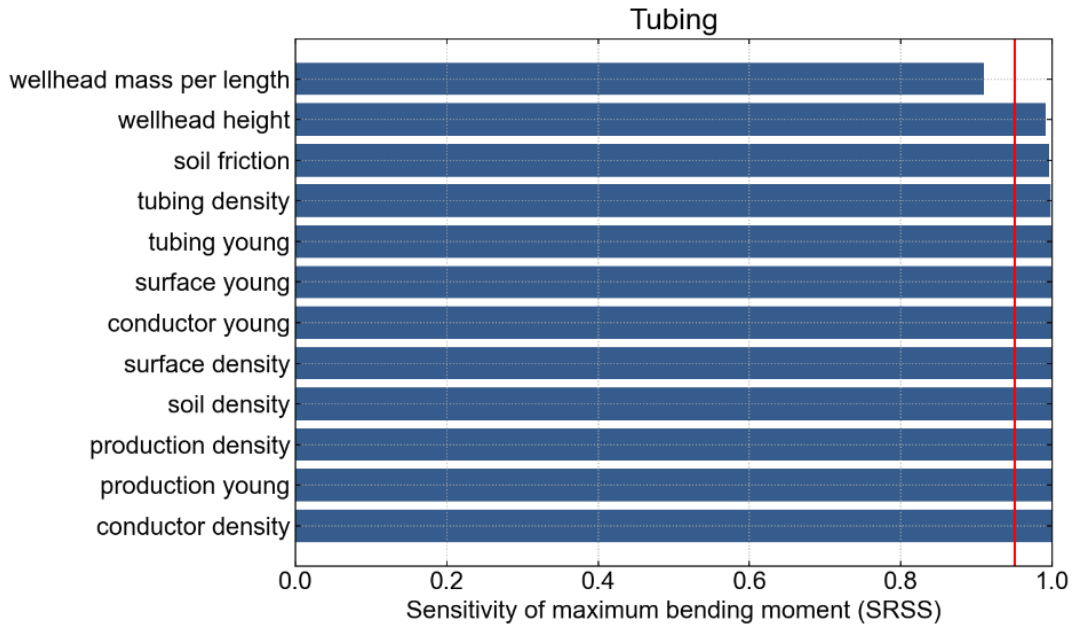


Figure 77: Sensitivity Analysis Result for Conductor Casing (RSN77_SFERN_PUL)

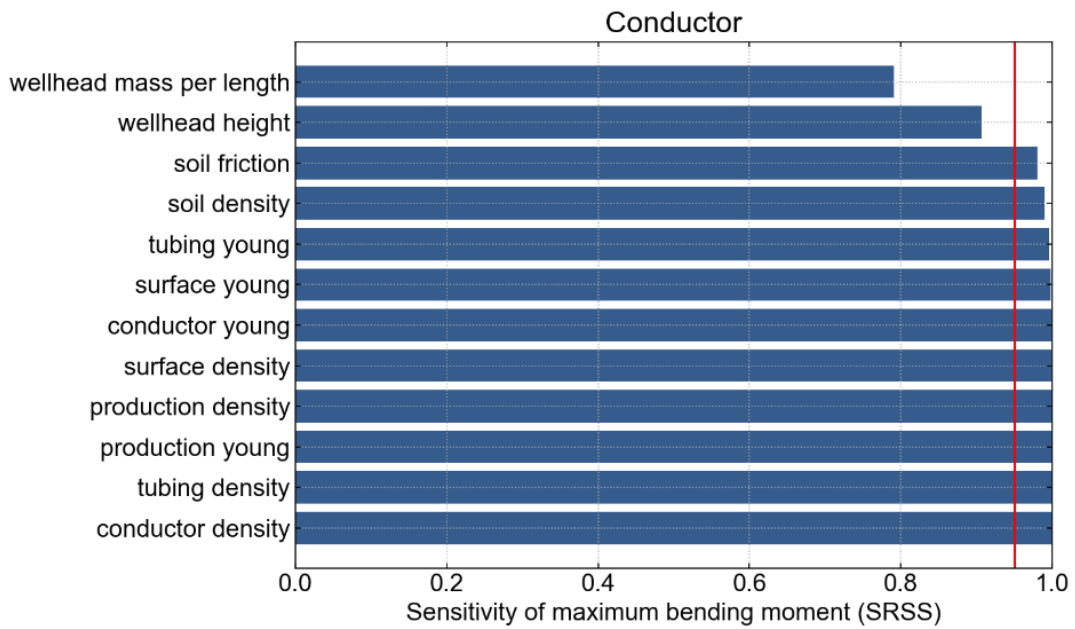


Figure 78: Sensitivity Analysis Result for Surface Casing (RSN77_SFERN_PUL)

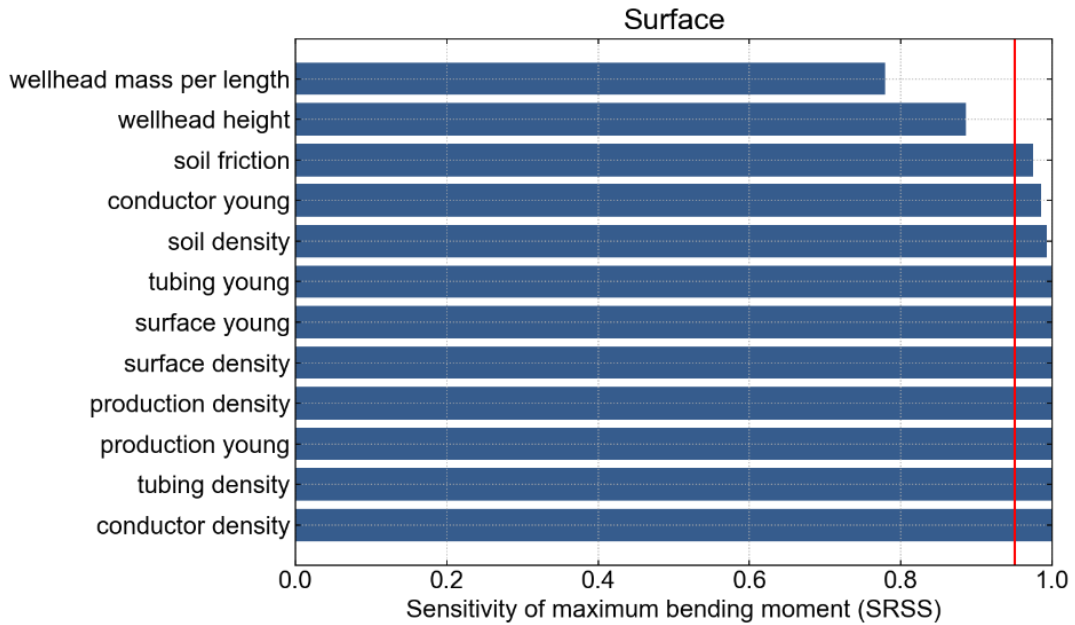


Figure 79: Sensitivity Analysis Result for Production Casing (RSN77_SFERN_PUL)

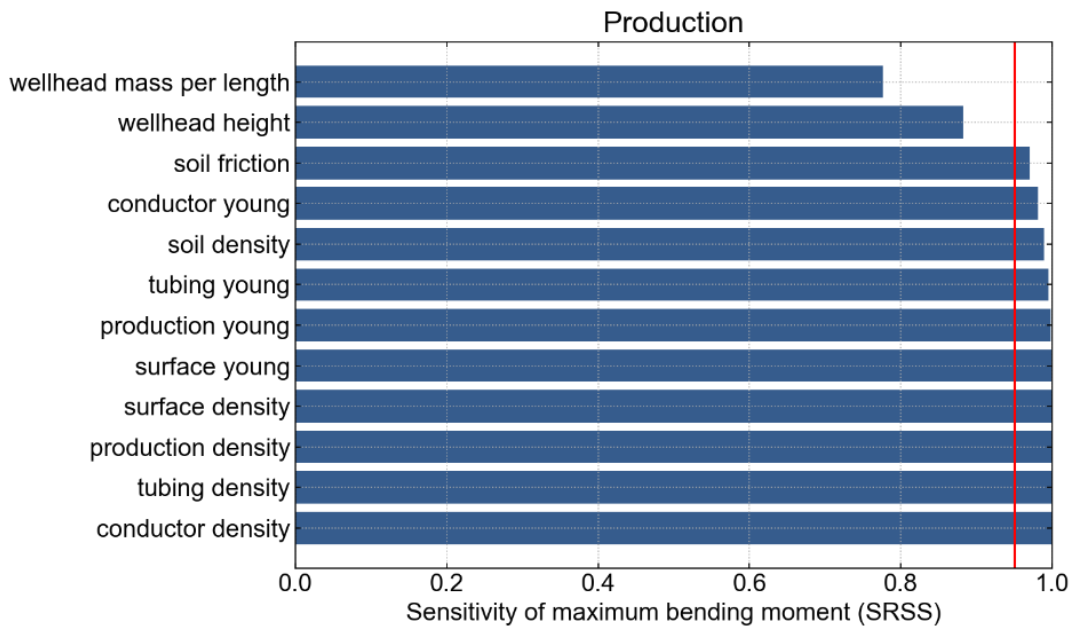
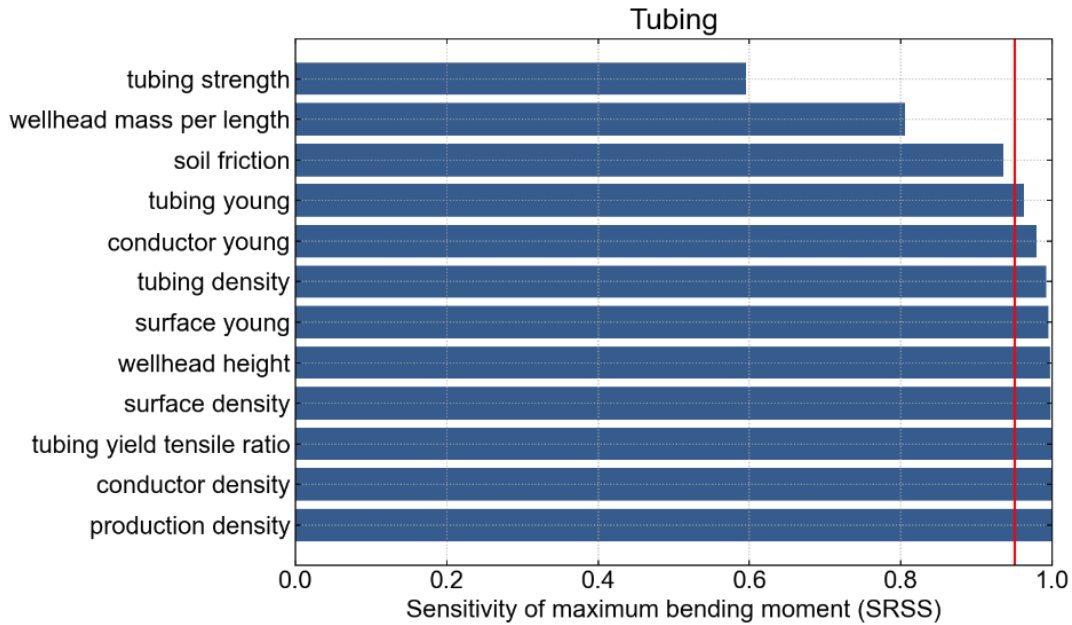


Figure 80: Sensitivity Analysis Result for Tubing (RSN77_SFERN_PUL)



Equations for Damage models

The maximum moment is calculated using Equations (C.31) and (C.32). Then using this maximum moment, the probability of shaking induced failure is calculated using Equation (3.7). The wells were again split up by well mode (explained in Section 3.3.1) and then by individual components (conductor casing, surface casing, production casing, and tubing)

First and Second Well Modes (all components)

For the first and second well modes, regardless of components, the following equation should be used in conjunction with Table 27 to Table 30 for each individual component.

$$\ln(M) = b_0 + b_1 h + b_2 h^2 + b_3 \phi + b_4 \phi^2 + b_5 m + b_6 m^2 + b_7 \ln(PGA) + b_8 \ln(PGA)^2 \quad (C.31)$$

Fourth Well Mode (all components)

For the fourth well mode, regardless of components, the following equation should be used in conjunction with Table 27 to Table 30 for each individual component.

$$\ln(M) = b_0 + b_1 h + b_2 h^2 + b_3 m + b_4 m^2 + b_5 \ln(PGA) + b_6 \ln(PGA)^2 \quad (C.32)$$

Where:

- M is the maximum moment (N-m);
- h is the height of the wellhead (m);

ϕ is the friction angle of the geomaterial (degree);

m is the mass per unit length of the height of the wellhead (kg/m);

$b_0, b_1, b_2, b_3, b_4, b_5, b_6, b_7, b_8$ are model coefficients given in Table 27 to Table 30, organized by the well components;

Table 27: Model Coefficients for Conductor Casings

	Mode 1		Mode 2		Mode 4	
	Coefficient	Coefficient Uncertainty	Coefficient	Coefficient Uncertainty	Coefficient	Coefficient Uncertainty
b_0	10.76168	0.123135	15.3602	1.367373	10.54768	0.105617
b_1	0.658693	0.073107	1.08049	0.069844	1.065653	0.07028
b_2	-0.06627	0.011974	-0.13668	0.011415	-0.13916	0.011495
b_3	0.001758	0.001685	-0.26282	0.076469	0.00056	6.94E-06
b_4	--	--	0.003674	0.001062	--	--
b_5	0.001374	4.25E-05	0.000551	6.87E-06	0.6067	0.003744
b_6	-3.74E-07	1.95E-08	--	--	-0.0272	0.001977
b_7	0.632604	0.003829	0.611787	0.003702	--	--
b_8	-0.01962	0.002022	-0.02584	0.001955	--	--
σ	0.335143	--	0.32396	--	0.32769	--

Table 28: Model Coefficients for Surface Casings

	Mode 1		Mode 2		Mode 4	
	Coefficient	Coefficient Uncertainty	Coefficient	Coefficient Uncertainty	Coefficient	Coefficient Uncertainty
b_0	9.527197	0.125012	8.480328	0.127201	9.083362	0.122692
b_1	0.665764	0.084604	1.119292	0.084643	0.891963	0.083034
b_2	-0.06382	0.013857	-0.13831	0.013844	-0.1059	0.0136
b_3	--	--	--	--	0.001398	4.83E-05
b_4	--	--	--	--	-3.73E-07	2.22E-08
b_5	0.001427	4.92E-05	0.000609	8.35E-06	0.688092	0.00435
b_6	-3.83E-07	2.26E-08	--	--	0.004312	0.002297
b_7	0.696716	0.004432	0.722274	0.004509	--	--
b_8	0.008166	0.00234	0.015596	0.002381	--	--
σ	0.387866	--	0.394659	--	0.380669	--

Table 29: Model Coefficients for Production Casings

	Mode 1		Mode 2		Mode 4	
	Coefficient	Coefficient Uncertainty	Coefficient	Coefficient Uncertainty	Coefficient	Coefficient Uncertainty
b_0	8.026537	0.132695	6.964498	0.136025	7.027724	0.142338
b_1	0.6834	0.089804	1.147249	0.090514	1.208894	0.094716
b_2	-0.06441	0.014709	-0.14094	0.014805	-0.15594	0.015492
b_3	--	--	--	--	0.000661	9.35E-06
b_4	--	--	--	--	--	--
b_5	0.001476	5.22E-05	0.00064	8.93E-06	0.80852	0.005046
b_6	-3.91E-07	2.40E-08	--	--	0.04631	0.002664
b_7	0.753006	0.004704	0.778036	0.004822	--	--
b_8	0.027775	0.002484	0.035062	0.002546	--	--
σ	0.411703	--	0.422035	--	0.441624	--

Table 30: Model Coefficients for Tubings

	Mode 1		Mode 2		Mode 4	
	Coefficient	Coefficient Uncertainty	Coefficient	Coefficient Uncertainty	Coefficient	Coefficient Uncertainty
b_0	10.75489	0.089303	10.4355	0.080335	9.398604	0.074102
b_1	-0.65819	0.060437	-0.51933	0.054368	-0.24406	0.05015
b_2	0.106031	0.009899	0.081967	0.008905	0.051431	0.008214
b_3	--	--	--	--	0.000556	2.92E-05
b_4	--	--	--	--	-1.61E-07	1.34E-08
b_5	0.000653	3.51E-05	0.000583	3.16E-05	0.13984	0.002627
b_6	-1.96E-07	1.61E-08	-1.74E-07	1.45E-08	-0.1193	0.001387
b_7	0.263827	0.003166	0.195672	0.002848	--	--
b_8	-0.13642	0.001672	-0.13808	0.001504	--	--
σ	0.277073	--	0.277073	--	0.229911	--

APPENDIX D:

Damage Models of Above Ground Infrastructure

Ground Shaking Damage Models for Above Ground Infrastructure

Damage models are available for two types of above ground components: (1) wellheads and (2) pressure vessels. Performance of wellheads is conditioned on joint rotation and strain, whereas performance of pressure vessels is conditioned on moment ratios, both of which are conditioned on the peak ground acceleration (PGA). Details to the models are provided in the subsection sections.

Ground Shaking Damage Models for Wellheads

The damage models for wellheads are divided into two stages: (1) the first stage involves calculating the influence of PGA on the longitudinal strain at the joints, and (2) the second stage involves calculating the influence of the joint rotation on the longitudinal strain. The models for rotation as a function of PGA are first given, followed by the models from rotation to longitudinal strain.

Seismic Intensity (PGA) to Joint Rotations on Wellheads

Subsystem P2-E (elbows)

For the P2 configuration with elbows, the rotation can be calculated using Equation (D.33), with the coefficients outlined in Table 31. This configuration and dimensions are shown in Figure 81.

$$\ln(Rot) = b_0 + b_1 \ln(H_t) + b_2 \ln(L_2) + b_3 \ln(L_6) + b_4 \ln(PGA) + b_5 \ln(H_t)^2 + b_6 \ln(L_2)^2 + b_7 \ln(L_6)^2 + b_8 \ln(PGA)^2 \quad (D.33)$$

Where,

Rot is the median rotation (degree);

H_t is the entire height of the well tree (ft);

L_2 is the length of pipe segment 2 (ft);

L_6 is the length of pipe segment 6 (ft);

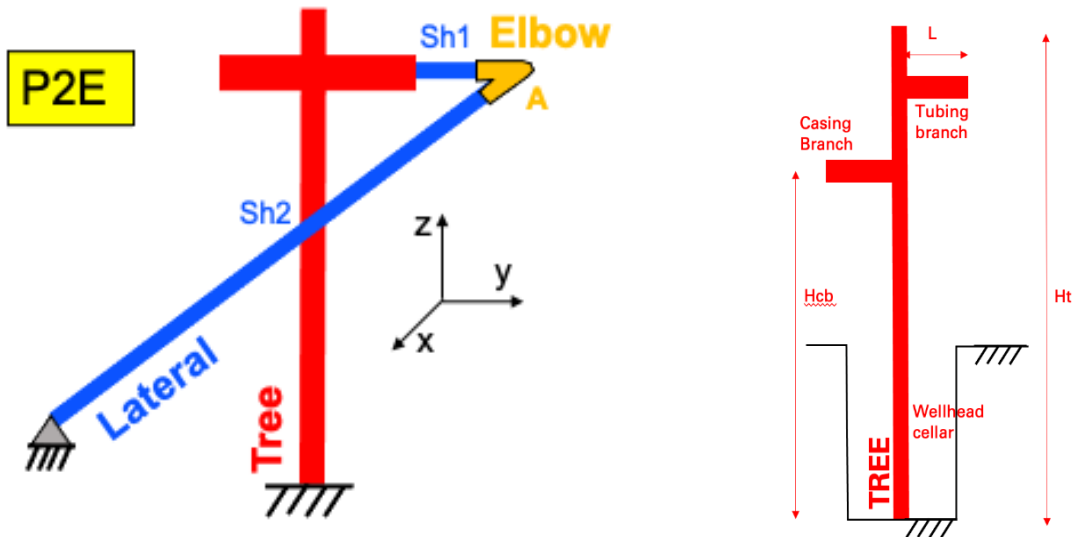
PGA is the peak ground acceleration of the ground motion (g); and

b_0 to b_8 are regression coefficients given by Table 31.

Table 31: Coefficients for subsystem P2-E (elbows)

Direction	X-Direction		Y-Direction	
Joint	A		A	
Component	4E-90 (elbows)		4E-90 (elbows)	
Orientation	Close (-)	Open (+)	Close (-)	Open (+)
b_0	-4.492392	-4.595058	-4.449407	-4.561067
b_1	-3.551781	-3.412715	-1.027858	-0.925346
b_2	-0.468746	-0.477662	0.7419337	0.7506968
b_3	-0.056979	-0.077827	-4.04115	-4.002458
b_4	1.0163933	1.0204682	1.0210042	1.0196173
b_5	1.5459539	1.5071445	0.5579471	0.5373218
b_6	0.121702	0.1226335	-0.400375	-0.401999
b_7	-0.10712	-0.10177	1.3897573	1.3701711
b_8	0.0066523	0.0125435	0.0197555	0.016749

Figure 81: Schematic of subsystem P2-E (elbow) with well tree dimensions



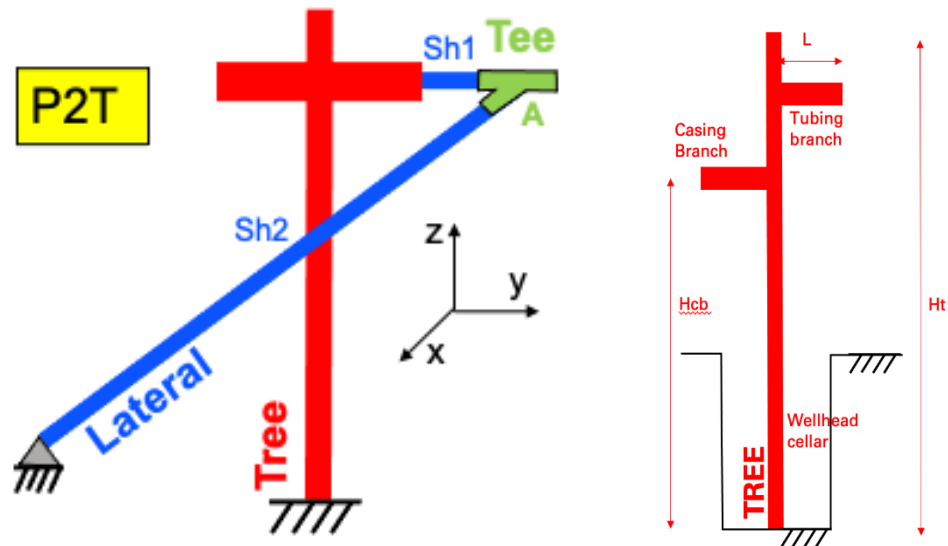
Subsystem P2-T (tee-joints)

The P2 tee-joints model follows Equation (D.33), with the coefficients outlined in Table 32. The variables needed are depicted in Figure 82.

Table 32: Coefficients for subsystem P2-T (tee-joints)

Direction	X-Direction		Y-Direction	
Joint	A		A	
Component	4T-IP (in-plane tee)		4T-IP (in-plane tee)	
Orientation	Close (-)	Open (+)	Close (-)	Open (+)
b_0	-4.177576	-4.518731	-4.462963	-4.558921
b_1	-3.821444	-3.36422	-0.963695	-0.8824
b_2	-0.561183	-0.579427	0.7376861	0.7598913
b_3	-0.064491	-0.082421	-4.126469	-3.975664
b_4	1.017156	1.0131557	1.0306181	1.0152461
b_5	1.6261647	1.4949155	0.5475509	0.5250301
b_6	0.150721	0.1566652	-0.397127	-0.404852
b_7	-0.102599	-0.098604	1.4222763	1.3611456
b_8	0.0111488	0.0109415	0.0235704	0.0154418

Figure 82: Schematic of subsystem P2-T (tee-joints) with well tree dimensions



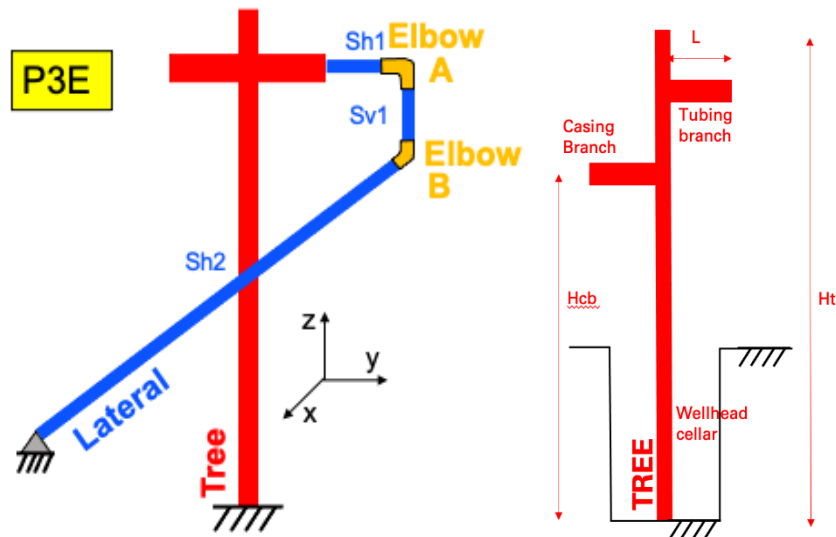
Subsystem P3-E (elbows)

The P3 elbows model follows Equation (D.33), with the coefficients outlined in Table 33. The variables needed are depicted in Figure 83.

Table 33: Coefficients for subsystem P3-E (elbows)

Direction	X-Direction		Y-Direction	
Joint	B		A	
Component	4E-90 (elbows)		4E-90 (elbows)	
Orientation	Close (-)	Open (+)	Close (-)	Open (+)
b_0	-14.61194	-14.71895	-11.9348	-11.78664
b_1	4.51517	4.7016769	2.622367	2.6286328
b_2	-0.420656	-0.42377	0.151097	0.1982484
b_3	1.009601	1.022949	0.31644	0.3240902
b_4	1.018331	1.0221844	1.052507	1.034169
b_5	-0.512237	-0.570144	0.022493	0.0030352
b_6	0.401096	0.3969054	-0.05415	-0.08186
b_7	-0.205076	-0.213641	0.214337	0.2012005
b_8	0.007106	0.0115539	0.041434	0.0252604

Figure 83: Schematic of subsystem P3-E (elbow) with well tree dimensions



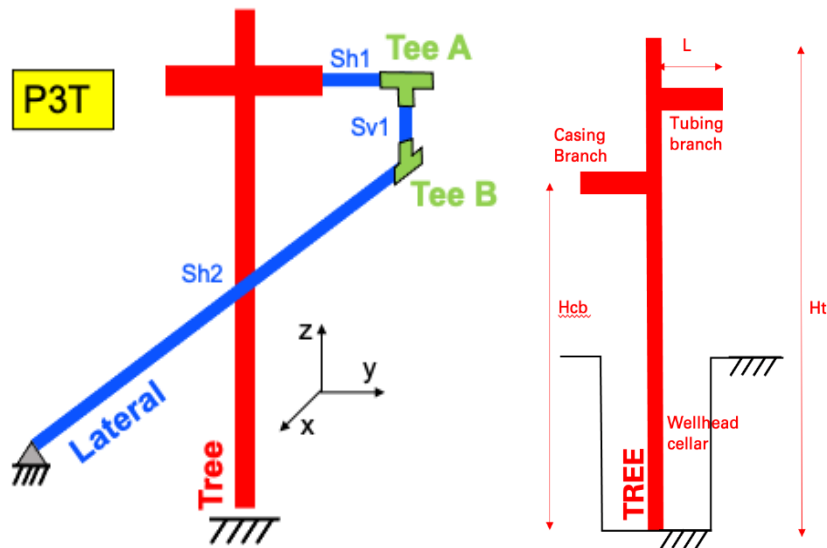
Subsystem P3-T (tee-joints)

The P3 tee-joints model follows Equation (D.33), with the coefficients outlined in Table 34. The variables needed are depicted in Figure 84.

Table 34: Coefficients for subsystem P3-T (tee-joints)

Direction	X-Direction			Y-Direction	
Joint	A	B		A	
Component	4T-OP (out-of-plane tee)	4T-IP (in-plane tee)		4T-IP (in-plane tee)	
Orientation	Both	Close (-)	Open (+)	Close (-)	Open (+)
b_0	-12.41726	-14.51882	-14.56424	-12.3567	-11.41485
b_1	3.5396056	4.416212	4.6306891	2.911206	2.4161603
b_2	-1.004937	-0.415758	-0.384809	0.167165	0.1855476
b_3	0.0617563	0.998542	1.0291383	0.352701	0.3304397
b_4	1.0198677	1.025087	1.0187997	1.079375	1.0189061
b_5	-0.518125	-0.484312	-0.561522	-0.023617	0.0421813
b_6	0.7775454	0.410226	0.383851	-0.060284	-0.07951
b_7	-0.000747	-0.197498	-0.216541	0.217201	0.1933541
b_8	0.0087592	0.011298	0.0096327	0.050151	0.0183808

Figure 84: Schematic of subsystem P3-T (tee-joints) with well tree dimensions



Subsystem P4-E (elbows)

For the P4 configuration with elbows, the rotation can be calculated using Equation (D.34), with the coefficients outlined in Table 35. This configuration and dimensions are shown in Figure 85.

$$\ln(Rot) = b_0 + b_1 \ln(H_t) + b_2 \ln(L_6) + b_3 \ln(W_v) + b_4 \ln(PGA) + b_5 \ln(H_t)^2 + b_6 \ln(L_6)^2 + b_7 \ln(W_v)^2 + b_8 \ln(PGA)^2 \quad (D.34)$$

Where,

Rot is the median rotation (degree);

H_t is the entire height of the well tree (ft);

L_6 is the length of pipe segment 6 (ft) for subsystem type 4;

W_v is the valve weight (lbf);

PGA is the peak ground acceleration of the ground motion (g); and

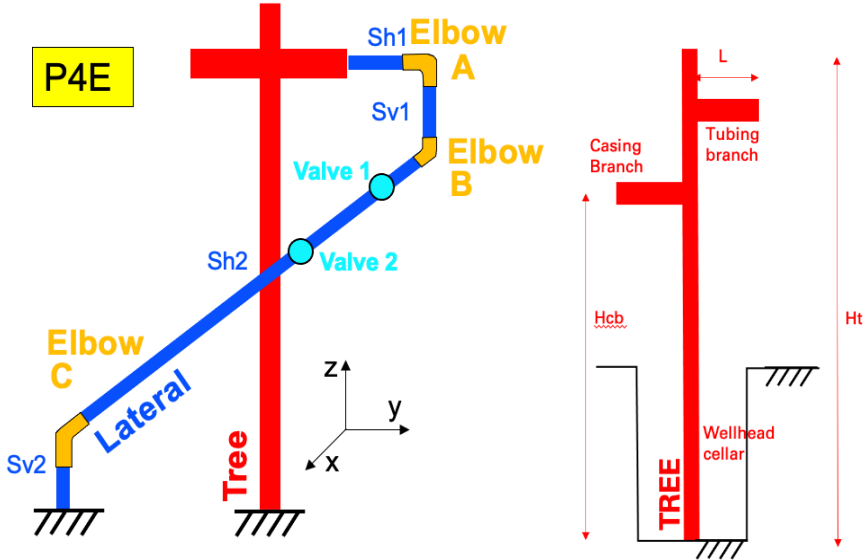
b_0 to b_8 are regression coefficients given by Table 35.

Table 35: Coefficients for subsystem P4-E (elbows)

Direction	Y-Direction	
Joint	A	
Component	4E-90 (elbow)	
Orientation	Close (-)	Open (+)
b_0	-11.44195	-11.77564
b_1	4.611668	4.654279
b_2	1.755868	1.9257181
b_3	1.125698	0.8767135
b_4	1.065353	0.9975371
b_5	-0.664844	-0.688403
b_6	-0.200098	-0.239633
b_7	0.103925	0.0295991
b_8	0.042193	0.0168513

Rotations for other combinations of direction, joint, and orientation were evaluated (e.g., x-direction, joint B, close); only the governing cases are presented in this table.

Figure 85: Schematic of subsystem P4-E (elbows) with well tree dimensions



Subsystem P4-T (tee-joints)

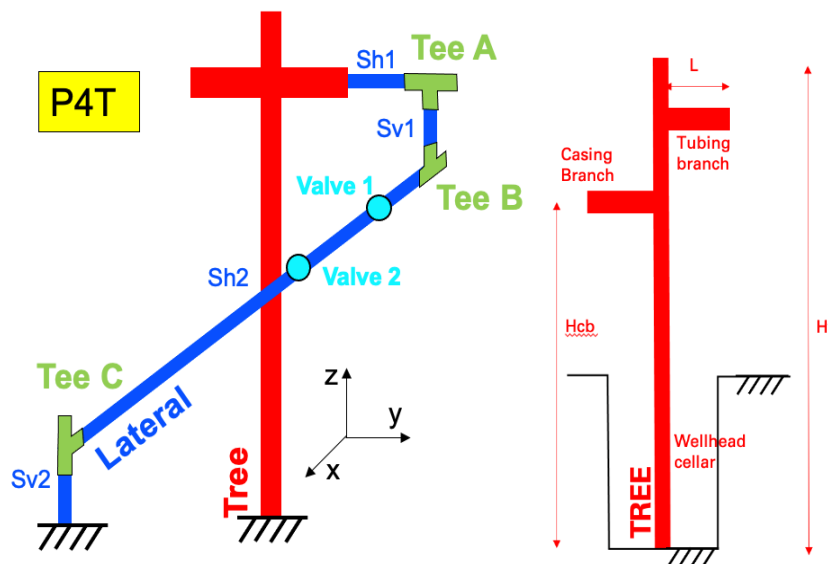
The P4 tee-joints model follows Equation (D.34), with the coefficients outlined in Table 36. The variables needed are depicted in Figure 86.

Table 36: Coefficients for subsystem P4-T (tee-joints)

Direction	Y-Direction		
Joint	A		C
Component	4T-IP (in-plane tee)		4T-OP (out-of-plane tee)
Orientation	Close (-)	Open (+)	Both
b_0	-12.18058	-11.65122	-7.222566
b_1	5.499801	4.6981409	0.176772
b_2	1.672947	1.8763506	1.9895425
b_3	1.356172	0.890829	0.4757355
b_4	1.171378	1.0068938	1.0779995
b_5	-0.827624	-0.695686	0.1533041
b_6	-0.17294	-0.236414	-0.149774
b_7	0.15359	0.029141	-0.142017
b_8	0.072764	0.0336236	0.0419737

Rotations for other combinations of direction, joint, and orientation were evaluated (e.g., x-direction, joint B, close); only the governing cases are presented in this table.

Figure 86: Schematic of subsystem P4-T (tee-joints) with well tree dimensions



Joint Rotations on Wellheads to Longitudinal Strains at Joint

The model to calculate the longitudinal strain as a function of joint rotation is given below. The model uses a weighted approach to capture the operating conditions where the operating pressure is “low” (termed “no pressure”) and where the operating pressure is “high”. More details to the terminology can be found in Pantoli et al. (2022).

$$\ln(\varepsilon) = w_{no\ pressure} \ln(\varepsilon)_{no\ pressure} + w_{high\ pressure} \ln(\varepsilon)_{high\ pressure} \quad (D.35)$$

Where:

$\ln(\varepsilon)$ is the weighted mean of the longitudinal strain (in fractions);

$$\ln(\varepsilon)_{no\ pressure} = b_{0,no\ pressure} + b_{1,no\ pressure} * \ln(Rot)$$

$$\ln(\varepsilon)_{high\ pressure} = b_{0,high\ pressure} + b_{1,high\ pressure} * \ln(Rot)$$

Rot is the rotation computed using Equations (D.33) and (D.34) (in degrees);

b_0, b_1 are the model coefficients for the respective pressure cases given in Table 37;

$w_{no\ pressure}, w_{high\ pressure}$ are weights associated with the “no pressure” and “high pressure” operating conditions.

Table 37: Coefficients for strain models

	b_0	b_1
4T-IP - No Pressure - Negative Rotation (Close)	-4.698614	0.9171584
4T-IP - No Pressure - Positive Rotation (Open)	-4.846407	1.6389036
4T-IP - High Pressure - Negative Rotation (Close)	-4.901993	1.6269746
4T-IP - High Pressure - Positive Rotation (Open)	-4.196789	1.8360272
4T-OP - No Pressure – Rotation (Both)	-5.672304	1.1390712
4T-OP - High Pressure – Rotation (Both)	-4.780363	1.1869063
4E90 - No Pressure - Negative Rotation (Close)	-5.650503	1.5118598
4E90 - No Pressure - Positive Rotation (Open)	-5.538686	1.0648018
4E90 - High Pressure - Negative Rotation (Close)	-5.675531	1.456687
4E90 - High Pressure - Positive Rotation (Open)	-5.293366	1.2205598

Ground Shaking Damage Models for Pressure Vessels

The damage model for pressure vessels is given by Equation (D.36). There are two conditions for pressure vessels, with and without stretch length, which describes base fixity condition. More details can be found in Pantoli et al. (2022).

$$\ln(M_r) = b_0 + b_1 \ln(PGA) + b_2 \ln(H_v) + b_3 \ln(D) + b_4 \ln(t_v) + b_5 \ln(D_a) + b_6 \ln(PGA)^2 + b_7 \ln(H_v)^2 + b_8 \ln(D)^2 + b_9 \ln(t_v)^2 + b_{10} \ln(D_a)^2 \quad (D.36)$$

Where:

M_r is the moment ratio (i.e., demand over capacity);

PGA is the peak ground acceleration (g);

H_v is the vessel height (ft);

D_v is the diameter of the vessel (ft) computed by $D_v = \frac{H_v}{H_v/D_v}$;

H_v/D_v is the height-to-diameter ratio for pressure vessels;

t_v is the thickness of the skirt of the vessel (in) computed by $\ln(t_v) = -7.95 + 0.934 * \ln(p) + 0.968 * \ln(D_v)$;

p is the pressure vessel design pressure (psi);

D_a is the diameter of the anchor (in);

b_0 to b_{10} are the model coefficients for the respective pressure cases given in Table 38.

Table 38: Coefficients for the moment ratio model with and without stretch length

	No Stretch Length	With Stretch Length
b_0	-13.43384	-17.70944
b_1	1.037	0.557
b_2	5.741	9.207
b_3	-1.16954	-1.296184
b_4	1.232	0.904
b_5	-1.512576	-1.189906
b_6	0.017	-0.084697
b_7	-0.383869	-1.04548
b_8	-0.094814	0.098
b_9	0.096	-0.031504
b_{10}	-0.278842	-0.254759